



Republic of Iraq
Ministry of Higher Education
& Scientific Research
University of Diyala
College of Science
Department of Physics



**Preparation of Nano barium ferrite and measurement
of its electrical properties at (x-band) region using
waveguide**

A Thesis

*Submitted to The Council of the College of Sciences, University of Diyala in
Partial Fulfillment of the Requirements for the Degree of Master of science in
Physics*

By

HUSSEIN SULAIMAN MAHMOOD

B.Sc. in Physics 2007

Supervised by

Asst. Prof. Dr. Tahseen H. Mubarak

2016 AD

Dr. Saib Thiab Alwan

1438AH

بِسْمِ اللَّهِ الرَّحْمَنِ الرَّحِيمِ

لَقَدْ أَرْسَلْنَا رُسُلَنَا بِالْبَيِّنَاتِ وَأَنْزَلْنَا مَعَهُمُ الْكِتَابَ
وَالْمِيزَانَ لِيَقُومَ النَّاسُ بِالْقِسْطِ وَأَنْزَلْنَا الْحَدِيدَ فِيهِ
بَأْسٌ شَدِيدٌ وَمَنْفَعٌ لِلنَّاسِ وَلِيَعْلَمَ اللَّهُ مَنْ يَنْصُرُهُ وَرُسُلَهُ
بِالْغَيْبِ إِنَّ اللَّهَ قَوِيٌّ عَزِيزٌ ﴿٢٥﴾

CERTIFICATION

We certify that this thesis was prepared under our supervision at the University of Diyala /College of Science / Department of Physics as a partial requirement for the Degree of Master of science in Physics.

Signature:

Name: Dr.Tahseen H.Mubarak

Title: Asst. Prof.

Date:

Signature:

Name: Dr. Saib Thiab Alwan

Title: Lecturer

Date:

Head of the Physics Department

In view of the available recommendation, I forward this thesis for debate by the examining committee.

Signature:

Name: Dr. Ziad T. Khudair (Ph.D)

Title:

Date: / /

A close-up photograph of several dark red roses in full bloom, with green stems and leaves visible. The background is a soft, out-of-focus light color.

In the name of Allah, the Beneficent, the Merciful

All praise is due to Allah, the Lord of the Worlds

DEDICATION

**I DEDICATE THIS THESIS
To the souls of the Iraqi Martyrs
and
My parents**

Hussein.S.M

Acknowledgments

First of all, thanks to his Almighty Allah, whose Grace enabled me to continue this work and overcome all difficulties.

I would like to express my sincere gratitude to my supervisors *Assist Prof. Dr. Tahseen Hussein Mubarak, and Dr. Saib Thiab Alwan,* Who have granted me the opportunity to do this research. I am indebted to them for their suggestions and valuable remarks.

Special thanks are extended to the **Dean of the College of Science** and all the **staff of the Department of Physics** for their assistance. I am also grateful to **the physics Department at the College of Education Ibn al-Haytham** for their kind help during the laboratory work and x-ray tests also special thanks for **the applied physics department in the University of Technology** for their kind help during the laboratory work and I would like to express my appreciation to **Dr. Atheer Ibrahim Abd Ali Al- Khfagy and the lecturer Duraid fawzi Mahdi** . I would like to extend my thanks and gratitude to **Dr.Lubab Ali Salman** for his outstanding efforts and instructions on the device (VNA) in the **Electronic and Communications Engineering Department /Al-Nahrain University**. I am grateful for my colleagues.

Abstract

M-type barium hexaferrite ($\text{BaFe}_{12}\text{O}_{19}$) have been synthesized by using sol-gel auto combustion technic to prepare homogeneous and ultrafine ferrites with narrow size distribution at a relatively low calcination temperature. Nitrate salts, citric acid and ammonia were used in order to ferrite nanopowders at temperature 100°C ,illustrated from XRD patterns the perfect ratio to get M-type hexagonal phase when the molar ratio of ferric nitrate to barium nitrate equal (12/1), the obtained ferrite nanopowders calcined at different temperatures ; 700°C , 800°C , 900°C , 1000°C , 1100°C and 1200°C for three hours.

XRD tests showed the presence of intermediate phase (BaFe_2O_4) and the existence of ($\gamma\text{-Fe}_2\text{O}_3$) with formation barium hexaferrite ($\text{BaFe}_{12}\text{O}_{19}$) at 700°C and the intermediate phases vanishes when the temperatures increased to 800°C , then appropriate specimens for studying electrical properties and microwave characteristics.

The SEM micrographs of Barium hexaferrite samples showed the average grain size estimated about 0.5, 0.6, 0.8,1 and $1.3\mu\text{m}$ at 800°C , 900°C , 1000°C , 1100°C and 1200°C respectively, so the increasing of the calcination temperature leads to grow the grain size.

The electrical testing of the barium hexaferrite samples was done by LCR-meter at room temperature in the range of 50Hz to 1MHz, observed that all the samples have higher dielectric constant at lower frequency decreases sharply up to (25175 Hz) and then decrease gradually with increasing frequency.

This behavior is typical for ferrites and a similar behavior was observed by other researchers, above (25175 Hz) notice a changing in the behavior of dielectric constant.

Microwave absorbing characteristics of the barium hexaferrite samples have been carried out at x-Band the frequency range (8- 12.5) GHz, Nicholson-Ross-Weir (NRW) method used to calculate both of the electrical permittivity and magnetic permeability from the s-parameters, observed an increasing the value of the attenuation of the samples that has been sintering at (900°C, 1000°C, 1100°C and 1200°C) by increasing the sintering temperature except for the samples that had been sintered at 800°C it behaves differently from other samples.

Also, composite material was synthesized consisting of; epoxy-resin as the matrix and reinforcement material (BaTiO_3 or/and $\text{BaFe}_{12}\text{O}_{19}$) by doping 1g of the powder per 10 g epoxy-resin, the maximum reflection loss, -36.83dB observed for the samples $\mathbf{A}_{1:3}$ (ferrite: barium titanate \rightarrow 1:3).

Contents

Subject	Page
Chapter One: Introduction & Applications	
1.1- Introduction	1
1.2- Literature Review	4
1.3- Aim of Study	8
Chapter Two: Theoretical Background	
2.1- Microwaves	11
2.2- Vector Network Analyzer	12
2.3- Scattering parameter	12
2.4- Transmission/Reflection Methods	13
2.4.1- Nicolson-Ross-Wier (NRW) Model	14
2.5- Maxwell's Equations	16
2.6- Electromagnetic Waves Propagation	18
2.7- Propagation in free space	18
2.8- Propagation through a homogenous medium	19
2.9- The electric and magnetic loss	21
2.10- Absorbent Material $\mu = \epsilon$	23
2.11- Absorption Mechanisms	24
2.11.1- Electric field loss	25
2.11.2- Magnetic field loss	27
2.12 -Origin of Magnetism	31
2.13- Types of Magnetic Materials	32
2.13.1- Diamagnetism	34
2.13.2- Paramagnetism	35

2.13.3- Ferromagnetism	37
2.13.4 -Antiferromagnetism	38
2.13.5- Ferrimagnetism	39
2.14 -Types of Ferrites with Respect to Their Magnetic Properties	40
2.14.1- Soft Ferrites	40
2.14.2- Hard Ferrites	40
2.15 -Structure of BaFe ₁₂ O ₁₉	42
2.16- Origin of Magnetization in BaFe ₁₂ O ₁₉	43
2.17- Epoxy resins	44
2.18- Method of preparation ferrites	44
2.18.1- Ceramic method	45
2.18.2- Sol-gel method	46
2.19 -Structural Properties	46
2.19.1 -Debye-Scherrer-Method	47
2.19.2 -Spacing of Lattice Planes	48
2.20 -Densities of ferrites	48
2.21- Diameter of grains	49
2.22 -Composites	50
2.23 - Dielectric Materials	50
2.24 - Ferroelectricity	52
Chapter Three: Experimental Part	
3.1- Introduction	55
3.2 - Selection of raw materials for preparing barium hexaferrite	55
3.3.1- Calculating Molecular weight of materials	56
3.3.2 - Method of preparation of barium ferrite	56
3.3.3 - Preparation of samples (m-type barium hexaferrite)	59

3.4- Preparation of barium titanate (BaTiO ₃) using the Conventional Ceramic Method	60
3.5 - Preparation of Composite material	62
3.6 – Instruments	63
3.6.1 - Network analyzers	63
3.6.2 - Nicholson-Ross-Weir (NRW)	66
3.6.3 - X-ray Diffraction Tests	68
3.6.4 - Measuring the density	69
3.6.5 - Scanning electron microscope (SEM) Test	69
3.6.6 - LCR –meter	71
Chapter Four: Results and Discussion	
4.1 – Introduction	74
4.2 - X-Ray Diffraction Results	74
4.3- Scanning Electron Microscopy result	83
4.4- Density measurement result	78
4.5- Electrical properties for the barium hexaferrite	88
4.5.1- Dielectric constant	88
4.5.2- A.C –Conductivity	91
4.6- Microwave characterization	93
4.6.1- Absorbing Properties	93
4.6.2- Relative Complex permittivity and permeability	97
4.7- microwaves absorbing composites	102
4.8- X-Ray Diffraction Result for (BaTiO ₃)	103
4.9- Microwave characters for the composites	104
4.9.1- Absorbing Properties	104
4.9.2- Relative Complex Permittivity and Permeability	109

Chapter Five: Conclusions & Future Recommendations	
5.1- Conclusions	118
5.2- Future recommendations	119
Appendix	122
References	133

List of Tables

No.	Title	Page
(2-1)	IEEE microwaves frequencies bands.	11
(2-2)	Chemical composition and crystallographic building for hexaferrites.	41
(2-3)	The number of ions per unit formula, coordination and spin direction for the Fe ³⁺ cationsublattices of M-type BaM.	43
(3-1)	The chemical materials and their properties.	55
(3-2)	Molar ratios and weight compounds used for the preparation of barium ferrite.	56
(3-3)	Describes sintering process for the samples.	59
(3-4)	The raw materials which used to prepare (BaTiO ₃) in Conventional ceramic method.	61
(3-5)	Preparation stages of BaTiO ₃ .	61
(3-6)	Show Epoxy- Resin with ratio of (barium hexaferrite/ barium titanate).	62
(4-1)	Shows the phase composition of the obtained powders after auto-combustion and after calcining at different temperatures and different molar proportion.	81
(4-2)	Calculation lattice parameters for XRD patterns of the powders calcined at different temperatures.	82
(4-3)	The measured proportions of elements, employing SEM/EDX analysis.	87
(4-4)	The porosity of barium hexaferrite samples sintered at different temperature.	88

(4-5)	Clarify values of complex permittivity and permeability, characteristic impedance, loss tangent for resonance peaks.	101
(4-6 a)	Clarify values of complex permittivity and permeability, characteristic impedance, loss tangent for resonance peaks, sample ($A_{0:0}$).	114
(4-6 b)	Clarify values of complex permittivity and permeability, characteristic impedance, loss tangent for resonance peaks, samples $A_{4:0}$ & $A_{3:1}$.	114
(4-6 c)	Clarify values of complex permittivity and permeability, characteristic impedance, loss tangent for resonance peaks, $A_{2:2}$, $A_{1:3}$ & $A_{0:4}$.	115

List of Figures

No.	Title	Page
(1.1)	Fields of application of hexagonal ferrites.	4
(2.1)	two-port network with “ <i>a</i> ” s and “ <i>b</i> ” s defined	12
(2.2)	Dipole alignment with an electric field	26
(2.3)	Debye relaxation spectra	27
(2.4)	Hysteresis loop	28
(2.5)	Precessional motion of magnetization	30
(2.6)	Schematic illustration of the frequency behavior of ferrites	30
(2.7)	Periodic table showing different types of magnetic materials	33
(2.8)	Diamagnetic material	35
(2.9)	Paramagnetic material	36
(2.10)	Ferromagnetism	38
(2.11)	Antiferromagnetism	39
(2.12)	Ferrimagnetism	40
(2.13)	Crystal Structure of Barium Hexaferrite	42
(2.14)	The four basic operations in ferrite preparation diagram	45
(2.15)	barium titanate (BaTiO_3) unit cell	53
(3.1)	Auto-combustion Flow diagram for preparing Nano powders barium ferrite.	58
(3.2)	Shows samples that have been prepared for the purpose of: a- For the LCR-meter tests b- For VNA tests	60
(3.3)	Prepared composite material for study microwave characteristic tests.	63
(3.4)	vector network analyzer device	64
(3.5)	(a)-sample inserted into a segment of waveguide (b)- Coaxial probe of (VNA) connected to the ends of waveguide.	65
(3.6)	The process for the NRW method.	67
(3.7)	Schematic of the basic components of the SEM	70
(3.8)	LCR meter used in electrical measurement	71
(4.1)	XRD patterns after auto-combustion on hot plate in 100°C and before calcination precursor.	75
(4.2)	XRD patterns of the powders calcined at 700°C .	76

(4.3)	XRD patterns of the powders calcined at different temperatures.	77
(4.4)	XRD patterns of the powders calcined at 1200°C.	78
(4.5)	XRD patterns of the powders calcined at 1200°C with molar ratio to Fe/Ba (12:3).	79
(4.6)	XRD patterns of the powders calcined at 1200°C with molar ratio to Fe/Ba (12:6).	80
(4.7)	SEM micrographs of M-type Barium hexaferrite sintered at 800°C for 3h .	84
(4.8 a)	SEM micrographs of M-type Barium hexaferrite sintered at 900°C for 3h .	84
(4.8 b)	SEM micrographs of M-type Barium hexaferrite sintered at 1000°C for 3h .	85
(4.8 c)	SEM micrographs of M-type Barium hexaferrite sintered at 1100°C for 3h .	85
(4.9)	SEM micrographs of M-type Barium hexaferrite sintered at 1200°C for 3h .	86
(4.10 a)	variation of real part of dielectric constant (ϵ') with frequency (Hz) for the Barium Hexaferrite samples sintered at (800°C, 900°C, 1000°C, 1100°C and 1200°C).	89
(4.10 b)	variation of imaginary part of dielectric constant (ϵ'') with frequency (Hz) for the Barium Hexaferrite samples sintered at (800°C, 900°C, 1000°C, 1100°C and 1200°C).	90
(4.11)	variation of A.C conductivity with frequency for barium hexaferrite	92
(4.12a)	Measured reflection loss for barium hexaferrite sintered at different temperatures (800°C, 900°C and 1000°C). frequency (Hz)	94
(4.12b)	Measured reflection loss for barium hexaferrite sintered at different temperatures (1100°C and 1200°C).	95
(4.13)	Showed absorbance curve versus (x-band) microwave frequencies for barium hexaferrite sintering at different temperature.	96

(4.14a)	Real part of permittivity for hexagonal barium ferrite within frequency range (8-12.5GHz).	98
(4.14b)	Imaginary part of permittivity for hexagonal barium ferrite within frequency range (8-12.5GHz).	99
(4.15a)	Showed real part of permeability of hexagonal barium ferrite at x-band microwave frequencies.	100
(4.15b)	Showed imaginary part of permeability of hexagonal barium ferrite at x-band microwave frequencies.	100
(4.16)	XRD patterns for the barium titanate powder	104
(4.17a)	showed the reflection loss values as a function of frequency for samples $A_{0:0}$, $A_{4:0}$ and $A_{3:1}$	105
(4.17b)	showed the reflection loss values as a function of frequency for samples $A_{2:2}$, $A_{1:3}$ and $A_{0:4}$	106
(4.18)	Showed absorbance curve versus microwave frequencies(x-band) for composite templates.	108
(4.19)	Showed real and imaginary part of permittivity for composite samples $A_{0:0}$, $A_{4:0}$, $A_{3:1}$, $A_{2:2}$, $A_{1:3}$ and $A_{0:4}$	111
(4.20)	Showed real and imaginary part of the permeability spectra of composite samples $A_{4:0}$, $A_{3:1}$, $A_{2:2}$ and $A_{1:3}$.	112

List of Symbols

Symbol	Definition	Unit
F	Frequency	Hz
$S_{11}, S_{21}, S_{12}, S_{22}$	Scattering parameter; S_{11} (related to the radiation emission from port 1 and collect in port 1) and S_{21} (scattering parameter related to the radiation emission from port 1 and collect in port 2) etc...	----
Γ_j	Reflection coefficient	----
T_j	Transmission coefficient	----
μ_r	Relative Permeability	----
μ_r'	Real Part of Relative Permeability	----
μ_r''	Imaginary Part of Relative Permeability	----
ϵ_r	Relative Permittivity or Dielectric Constant	----
ϵ_r'	Real Part of Relative Permittivity	----
ϵ_r''	Imaginary Part of Relative Permittivity	----
λ_c	Cutoff wavelength	cm
λ_0	free space wavelength	cm
E	Electric field intensities	volt/m
H	Magnetic field intensities	Ampere/m
D	Electric flux densities	coulomb/m ²
B	magnetic flux densities	Weber/m ² or Tesla
\vec{J}	electric current density(charge flux)	Ampere/m ²
ρ	volume charge density	Coulomb/m ³
ϵ_0	8.854×10^{-12}	Farad/m
μ_0	$4\pi \times 10^{-7}$	Henry/m
σ	Conductivity	($\Omega \cdot \text{cm}$) ⁻¹
Z_0	Intrinsic Impedance of Free-Space	377 Ω
Z	Intrinsic Impedance of the Material	Ω
Z_r	Relative Impedance	----
v	velocity of propagate in homogeneous isolated	m/sec
γ	propagation constant	----
α	attenuation constant	<u>Nepers</u> /meter
β	Phase Constant	Radian/m
t	time	S
ω	Angular frequency ($2 \pi f$)	rad.s ⁻¹
δ_m	Magnetic Loss Angle	Degree or Rad
δ_ϵ	Electric loss Angle	Degree or Rad

τ	relaxation time	S
f_c	Relaxation Frequency	Hz
M	Magnetization	A/m
H_c	Coercive Force	Oe
δ	skin depth	cm
F_L	Lorentz force	N
q	charge	Colomb
m	Mass	g
x	displacement	cm
β	damping coefficient	----
M_s	saturation magnetization	emu/g
f_L	Larmor angular frequency	Hz
γ	gyroscopic ratio	rad.T ⁻¹ S ⁻¹
χ	magnetic susceptibility	----
C	Curie constant	----
T	absolute temperature	°K
T_c	Curie temperature	°C
λ	Wavelength	Å
θ	Diffraction angle	degree
D	grain size	μm
d	Interplaner Distance	Å
(hkl)	Miller indices	----
d_B	Bulk density	g/cm ³
R.L	reflection loss	dB

List of Abbreviations

Symbol	Definition
UHF	Ultra high frequency region ranges between 300 MHz and 3 GHz
NFMR	Natural ferrimagnetic resonance
FMR	ferrimagnetic resonance
EHF-therapy	30 to 300 GHz, therapy and IR radiation in combined treatment of children suffering from atopic dermatitis].
EMI	Electromagnetic immunity
EMC	Electromagnetic compatibility
SI	Signal integrity
RAM	Radar Absorbing Materials
PMMA	Poly (methyl methacrylate)
VNA	Vector Network Analyzer
MW	Microwaves region (1-100) cm
RF	Radio frequency
IR	Infrared region
IEEE	Institute of Electrical and Electronics Engineers
NRW	Nicolson-Ross-Wier
XRD	X-ray diffraction
ICDD	International Centre for Diffraction Data
ASTM	American Standard for Testing Materials
SEM	Scanning electron microscope
JCPDS	Joint Committee on Powder Diffraction Standards
FWHM	Full Width at Half Maximum
EDX	Energy Dispersive X-ray Analysis
FESEM	Field-emission Scanning Electron Microscope
MWCNTs	multi-walled carbon nanotubes
DBSA	Dodecylbenzene sulphonic acid
NZF	Nickel –zinc ferrite

Chapter One

Introduction

and

Previous Studies

1.1-Introduction

The history of magnetism is contemporary with the history of science, the magnet's ability to attract ferrous objects by remote control, acting at a distance, has captivated countless curious spirits over two millenia (not least the young Albert Einstein), to demonstrate a force field that can be manipulated at will, you need only two chunks of permanent magnet or one piece of permanent magnet and a piece of temporary magnet such as iron, weakly permanent magnets are quite plentiful in nature in the form of lodestones – rocks rich in magnetite, the iron oxide Fe_3O_4 – which were magnetized by huge electric currents in lightning strikes. Priests and people in Sumer, ancient Greece, China and pre-Colomban America were familiar with the natural magic of these magnets [1].

Ferrites is a type of ceramic compound consists of basically from iron oxide (Fe_2O_3) combined chemically with one or more additional metallic elements, ferrimagnetic materials are dark brown or gray in color and very hard and brittle in mechanical properties. They are prepared by heat-treating the various transition metal oxides or alkaline earth oxides with the ferric oxides [2].

The magnetic properties revealed by the ferrites known as ferrimagnetism, in fact which is different from ferromagnetism that is revealed by metallic materials. In 1952, a different kind of ferrites possess permanent magnetic characteristics was detected. These were known as hard ferrites with formula $\text{M}(\text{Fe}_{12}\text{O}_{19})$ where M is commonly (Sr, Ba, Pb or Ca), which has complex hexagonal structure with a unique c axis, which is the easy axis of magnetization in the basic structure.

Hexagonal ferrites are referred to as hard as the direction of magnetization cannot be changed easily to another axis. Workers at a Philips laboratory in Eindhoven in the Netherlands made the evolution of hexagonal ferrites possible.

Initially, these materials were studied for their use as permanent magnets or as magnetic soft cores at frequencies well into (UHF) Ultra high frequency region. Later on it was realized that due to their large “built in” biasing field, these materials have good prospects for application at microwave frequencies [3-6].

Since the beginning of this century Electrical engineering exert significant steps, developments in the electromagnetic and telecommunication fields have encouraged the advancement of the desired high- frequency dielectric and magnetic materials. At the same time innovative technology was encouraged to acquire additional information of the ionic structure of these ferrites, therefore made it possible to give an explanation for the semiconducting properties, and magnetic behavior.

After 1950 a new systems of magnetic oxides were detecting and evolved such as the barium hexaferrite $\text{BaFe}_{12}\text{O}_{19}$ the ferroxplana materials and the garnets. Moreover, enormous expansions in electronics happened, the exploitation of such certain characteristics of magnetic oxides as their gyromagnetic effects and their ability to store information [7].

Ferrites are also utilized as microwave absorbers, by interaction loss of the incident waves and dissipate microwave energy into thermal energy. These materials have an imaginary part of the permittivity and

Permeability that can vary with composition of material and frequency [8]. M type Hexaferrite has been reported for employment in microwave devices at *mm* wave frequencies [9].

Polivanov et al, 1960, and it was concluded that the absorbed energy at the natural ferrimagnetic resonance (NFMR), without any bias magnetic field, is significantly higher than the resistance or pure dielectric polarization loss. Thus the NFMR differs from the FMR only by the significantly lower magnetic field needed for the resonance operation of microwave (mm-wave) devices.

This theory lays the basis for many engineering applications, including the Hexaferrite radio absorbing materials with electrical conductivity close to zero; omnidirectionally matched with free space, protecting coatings; and devices for spectral analysis and frequency-selective measurements of microwave and mm-wave power. Also, as soon as a new class of ferrite materials, magneto –uniaxial hexagonal ferrites with high internal fields of crystallographic anisotropy, were synthesized, it has become possible to develop gyromagnetic resonance devices operating without external bias magnetization, or with low bias magnetization needed for ferrite saturation and tuning of the resonance frequency.

A utilization of hexagonal ferrites is established and remains very perspective for solving many problems related to microwave engineering, radar engineering, electromagnetic compatibility (EMC), electromagnetic immunity (EMI), and signal integrity (SI). Hexaferrites can be used for detections and suppression of unwanted radiation and coupling paths; for frequency-selective measurements of signal

Parameters; and for running proper non-reciprocal separation in channels of generation, transmission, and reception over the selected frequency bands within the wide range up to a few hundred GHz, Numerous applications illustrated in the Figure (1.1) [10].

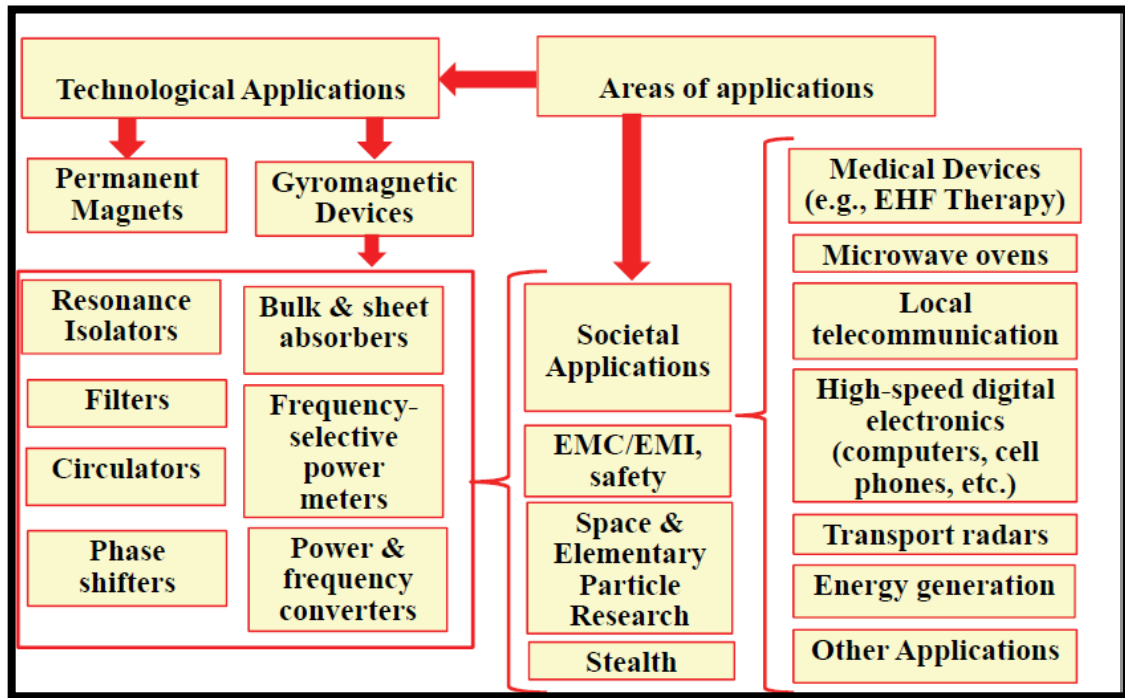


Figure (1.1): fields of application of hexagonal ferrites.

1.2 Literature Review

In 1994 J.Y.Shin et al, Y-type hexagonal ferrite- rubber composites were synthesized. By employment a network analyzer within the frequency range 200MHz -14GHz were measured complex permittivity and permeability of $Ni_{2-x}Zn_xY$ ferrite. Two types of resonance the domain wall and the spin rotational resonance, were observed .with a ferrite particle with a diameter of about 1 μm , only spin rotational resonance was observed [11].

In 2003 C. Dimri et al, M-type barium hexaferrite were prepared by the citrate sol-gel method, was observed possibility of controlling the

Particle size by varying the pH of the solution. Microwave characteristics measurements implemented by the Vector Network Analyzer using the cavity perturbation method [12].

In 2005 A. Ghasemi et al, M-type with chemical composition $\text{BaFe}_{12-x}(\text{Mn}_{0.5}\text{Cu}_{0.5}\text{Ti})_{x/2}\text{O}_{19}$ (x varying from 0 to 3 in steps of 1) were prepared by the classical ceramic method, microwave absorbing composite were formed after mixing the powder of ferrites with polyvinyl chloride plasticizer [13].

In 2006 S.M. Abbas et al, prepared M-type hexaferrite composition $\text{BaCo}_{0.9}\text{Fe}_{0.05}\text{Si}_{0.95}\text{Fe}_{10.1}\text{O}_{19}$ using conventional ceramic method. In the substituted hexaferrite composition $\text{BaCo}_x\text{Fe}^{+2}_y\text{Si}_{x+y}\text{Fe}^{+3}_{12-2x-2y}\text{O}_{19}$ ($x = 0.9$ and $y = 0.05$), Fe^{+3} ions are doped to replace into Fe^{+2} ions by the increase Si^{+4} (0.05) ion substitution. The dielectric losses is expected been reinforced due to electron hopping between Fe^{+3} and Fe^{+2} ions [14].

In 2007 Mu.Guohong, et al, M-type nanorods were prepared using a sol-gel technique, when added PMMA into the precursor solution phase shaped nanorods with diameters approximately 60nm and lengths nearly 300nm which are estimated from FESEM images, and without adding PMMA Generated granular shape. The microwave characteristics of barium hexaferrite for the two forms were measured using VNA within the frequency range 5–15GHz, observed the reflection loss for the rod- shaped are superior that possess granular [15].

In 2008 L. C .Jefferson et al, Z-type barium hexaferrite with chemical compositions of $\text{Ba}_3\text{Co}_2\text{Fe}_{24}\text{O}_{41}$ prepared using citric presider technique. Nanocomposites (80:20% weights) of Z-type barium hexaferrite with polychloroprene (CR) were synthesis for the microwave characteristics

Measurements by combining and molding the composite. Microwave absorbing characteristics achieved by the Transmission/Reflection method within the microwave frequencies (2.6-16GHz) [16].

In 2009 W.Lixi , et al, W-type barium hexaferrite substituted with Sm^{+3} in the chemical composition $\text{Ba}_{1-x}\text{Sm}_x\text{Co}_2\text{FeO}_{27}$ ($x=0.0, 0.05, 0.1, 0.15, 0.2$) were prepared by the conventional ceramic method. The microwave characteristics of the specimens have been measured within the microwaves frequencies S, C, X and Ku-band. With increasing Sm^{3+} ions doping It was observed that real and imaginary parts of permittivity increased slightly, and the peaks of ϵ'' tend to a lower frequency [17].

In 2010 R.S. Meena et al, Polycrystalline specimens of U-type barium hexaferrite series: $(\text{Ba}_{1-3x}\text{La}_{2x})_4\text{Co}_2\text{Fe}_{36}\text{O}_{60}$ with $0.10 \leq x \leq 0.20$ where the value of x in each blend equal (0.05), and the conventional solid state reaction method were used to prepared the component. Fractional replacements of Ba^{2+} ions with La^{3+} ions increases the electron hopping and decrease the magnetic behavior in the specimens within the X-band frequencies; be a result wide ranges microwave absorption in all specimens [18].

In 2010 G.Ali et al, (MWCNTs) nanocomposites have been prepared in two steps; in the first step, substitute Mn-Co-Ti in BaM to get chemical composition $\text{BaFe}_9\text{Mn}_{0.75}\text{Co}_{0.75}\text{Ti}_{1.5}\text{O}_{19}$ nanoparticles by using sol-gel technique. In the second step, an aquatic medium was utilized to dissipate carbon nanotubes and afterward blend MWCNTs with ferrite nanoparticles by hetero- coagulation. Nanocomposites which combined of MWCNTs/doped barium ferrite (BaM) exhibited good microwave absorption compared to that of pure MWCNTs and barium hexaferrite

Nanoparticles [19].

In 2011 C.Sun et al, chemical structure $\text{BaCe}_{0.05}\text{Fe}_{11.95}\text{O}_{19}$ it was prepared using the citrate sol–gel technique, and formed by Ce^{+3} substituted in M-type barium hexaferrite. The specimens were synthesized by mixing ferrite powder with paraffin wax at a ratio of 70% mass (ferrite). VNA was utilized to measure the (μ_r, ϵ_r) , microwave absorption properties were measured by the transmission/reflection coaxial line method within the frequency range 8–13 GHz [20].

In 2011 Prof. K. D Chapal, Radar absorbing materials(RAMs) were prepared from polymerize Aniline in the presence of dodecylbenzene sulphonic acid (DBSA) as a functionalized protonic acid in water medium to form DBSA-doped polyaniline (PANI). $\text{Ni}_{0.5}\text{Zn}_{0.5}\text{Fe}_2\text{O}_4$ (NZF) nanoparticles were synthesized by co-precipitation method along with Barium Titanate (BaTiO_3) particles to form $\text{BaTiO}_3\text{-Ni}_{0.5}\text{Zn}_{0.5}\text{Fe}_2\text{O}_4$ nanoparticles [21].

In 2013 K.Abhishek,et al, Single phase M-type barium hexaferrite powder with different particle size were prepared using sol-gel auto-combustion technique, the particle size was grown by increasing the period of annealing time, the product powders were mixed with epoxy –resin, thus obtained were cast into a rectangular pellet to match the waveguide dimensions with thickness 2.2mm [22].

In 2014 A.Hamed ,et al, w-type hexaferrites ($\text{Ba}(\text{Co}_x\text{Zn}_{1+x})_2\text{Fe}_{16}\text{O}_{27}$) with the combinations of $X= 0, 0.75, 0.5, 0.25$, were prepared using sol-gel auto-combustion technique. Study attempts to investigate the influence of temperature on synthesis and magnetic characteristic of w-type hexaferrites barium Nano composites with radar wave absorbing properties[23].

In 2014, S. Vinayasree et al, resilient single layer electromagnetic wave absorbers synthesis by merging suitable amounts of carbon black (CB) in a Nitrile butadiene rubber matrix along with an optimized amount of barium Hexaferrite (BaF) for Microwave applications in S, C, and X-bands. Complex permittivity and permeability were measured using the cavity perturbation method in the frequency range of 2–12 GHz. properties, bandwidth of absorption, thickness, and absorptivity [24].

In 2015 J.Silvia et al, hard-soft nanocomposites were prepared by using sol-gel auto-composition procedure, the hard-soft ferrites formed by two steps at first Nd-Co fractional substituted within strontium hexaferrite with chemical structure $\text{Sr}_{0.5}\text{Co}_{0.5}\text{Nd}_{0.5}\text{Fe}_{10.5}\text{O}_{19}$, and second NiFe_2O_4 Nickel ferrite nanoparticles were prepared, the hard-soft $\text{Sr}_{0.5}\text{Co}_{0.5}\text{Nd}_{0.5}\text{Fe}_{10.5}\text{O}_{19}/\text{NiFe}_2\text{O}_4$ with various weight proportions were mixed with epoxy resin in order to obtain mixtures sample/resin of about 45 wt% [25].

1.3 Aim of Study

- 1- M-type barium hexagonal ferrite Prepared at different temperatures and reveals the temperature at which consists of hexagonal phase, and studying the effect of increasing the concentration of barium oxide to form hexagonal phase.
- 2- Barium hexagonal ferrite treatment at different temperatures and investigated the effect of sintering temperature on the particle size, porosity, grain size, Electrical properties and microwave characteristics.
- 3- Prepare composite materials consisting of Barium titanate and barium hexaferrite powders dispersed in epoxy-resin as a template and investigate its microwave characteristics at x-band zone.

4- Programming and employment (NRW) method for Complex permittivity and permeability calculations.

Chapter two

Theoretical

Background

2.1 Microwaves

Microwaves are a form of electromagnetic radiation with frequencies bandwidth between radio frequency RF and infrared region IR, and wavelength ranging from 1cm to 100cm, the nature of the spectrum of microwave frequencies is a rotational spectrum. Microwaves are transverse electromagnetic waves in which the disturbance is a time-variation of the electric and magnetic fields \mathbf{E} and \mathbf{B} at a point. They are generated by accelerating (often-oscillating) electrical charges, or by magnetic dipole. The microwaves frequency contain of many regions which are divided by two methods; Institute of Electrical and Electronics Engineers (IEEE) method; and the other method is US military [26,27]; every region has its own specific applications, as monitoring, detecting, and censoring for the far or the short range. The most important are X-band and Ku-band because of it is widely applications in radar systems; table (2-1) listed the IEEE microwave frequency bands.

Table (2-1) IEEE microwaves frequencies bands [26].

Designation	Frequency range (GHz)
VHF	0.030-0.300
UHF	0.300-1.00
L-band	1.00-2.00
S-band	2.00-4.00
C-band	4.00-8.00
X-band	8.00-12.50
Ku-band	12.50-18.0
K-band	18.0-26.50
Ka-band	26.50-40.00
Millimetre	> 40.00

2.2 Vector Network Analyzer

The vector network analyzer VNA is the most important instrument in microwave measurements today. Its primary function is the measurement of S -parameters; this instrument has evolved into the workhorse of any microwave laboratory, and is today moving into measurement of nonlinear properties of components, and the frequency of operation today entering the THz region [28].

2.3 Scattering parameter

The responses of a network to external circuits can also be described by the input and output microwave waves, as shown in Figure (2.1) the input waves at port 1 and port 2 are denoted as a_1 and a_2 respectively, and the output waves from port 1 and port 2 are denoted as b_1 and b_2 respectively. These parameters (a_1 , a_2 , b_1 , and b_2) may be voltage or current, and in most cases, we do not distinguish whether they are voltage or current. The relationships between the input wave [a] and output wave [b] are often described by scattering parameters [S] [29]:

$$[b] = [S] [a] \quad \dots\dots\dots (2-1)$$

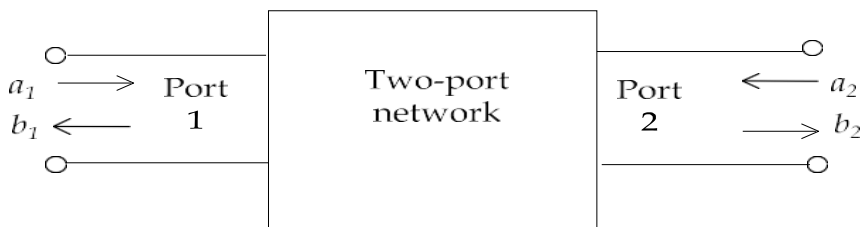


Figure (2.1) a two-port network with “ a ” s and “ b ” s defined

Where $[a] = [a_1, a_2]^T$, $[b] = [b_1, b_2]^T$, and the scattering matrix $[S]$ is in the form of $[S] = \begin{bmatrix} s_{11} & s_{12} \\ s_{21} & s_{22} \end{bmatrix}$ (2-2) For

a scattering parameter S_{ij} , if $a_i = 0$ ($i \neq j$), from Eq. (2-1), we have

$$S_{jj} = \frac{b_j}{a_j} \quad (j = 1, 2) \quad \dots\dots\dots (2-3)$$

$$S_{ij} = \frac{b_i}{a_j} \quad (i \neq j ; i = 1, 2; j = 1, 2) \quad \dots\dots\dots (2-4)$$

Equation (2-3) shows that when port j is connected to a source and the other port is connected to a matching load, the reflection coefficient at port j is equal to S_{jj} :

$$\Gamma_j = S_{jj} = \frac{b_j}{a_j} \quad \dots\dots\dots (2-5)$$

Equation (2-4) shows that when port j is connected to a source, and port i is connected to a matching load, the transmission coefficient from port j to port i is equal to S_{ij} :

$$T_j = S_{ij} = \frac{b_i}{a_j} \quad \dots\dots\dots (2-6)$$

2.4 Transmission/Reflection Methods

In this method, the specimen is placed in a portion of transmission line, and the permeability and permittivity of the specimen are derived from the transmission and reflection of the specimen, after analyzing the working principle and calculation algorithms, we discuss four types of transmission/reflection methods, including coaxial airline method, waveguide method,

Hollow metallic, free-space method and surface-wave method. We can get the electromagnetic properties of the specimen. In a transmission/reflection method, all the four scattering parameters can be measured, so we have more data at our disposal than in reflection measurements. For a transmission/reflection measurement, the relevant scattering equations contain variables including the complex permittivity and permeability of the specimen, the positions of the two reference planes, and the sample length. These relevant scattering equations are generally over determined and therefore can be solved in various ways [29].

2.4.1 Nicolson-Ross-Wier (NRW) Model

The NRW method is a common technique for calculating material's electromagnetic properties from the s-parameters [30, 31]. It requires at least two measured parameters (S_{11} and S_{21}) and works well for lossy materials and short samples. The method is derived from the following two equations for S_{11} and S_{21}

$$S_{11} = \frac{(1-T^2)\Gamma}{1-\Gamma^2 T^2}$$

$$S_{21} = \frac{(1-\Gamma^2)T}{1-\Gamma^2 T^2} \dots\dots\dots (2-7)$$

Where Γ is a reflection coefficient

$$\Gamma = \frac{\sqrt{\frac{\mu_r}{\epsilon_r}} - 1}{\sqrt{\frac{\mu_r}{\epsilon_r}} + 1} \dots\dots\dots (2-8)$$

and T is a transmission coefficient

$$T = \exp \left[-i \frac{w}{c} \sqrt{\mu_r \epsilon_r} d \right] \dots\dots\dots (2-8)$$

Here $w = 2\pi f$ (angular frequency), c (speed of light), and d (thickness of the sample). Therefore, we can find both of the coefficients from the s-parameters

$$V_1 = S_{21} + S_{11}$$

$$V_2 = S_{21} - S_{11} \dots\dots\dots (2-9)$$

$$\text{And if } X = \frac{1 - V_1 V_2}{V_1 - V_2} \dots\dots\dots (2-10)$$

The optimum thickness for the sample is $\frac{\lambda_g}{4}$, where

$$\frac{1}{\lambda_g} = \frac{1}{\sqrt{\frac{\epsilon_r \mu_r}{\lambda_0^2} - \frac{1}{\lambda_c^2}}} \dots\dots\dots (2-11)$$

λ_c - cut off frequency ($\lambda_c = \infty$ for coaxial transmission line) and λ_0 - frequency in GHz

$$\text{Then } \Gamma = x \pm \sqrt{x^2 - 1} \dots\dots\dots (2-12)$$

$$\Gamma = \frac{V_1 - \Gamma}{1 - V_1 \Gamma} \dots\dots\dots (2-13)$$

The appropriate sign should be chosen in (2-12) so that $|\Gamma| \leq 1$.

Now, from (2-8) we define

$$\frac{\mu_r}{\epsilon_r} = \left(\frac{1 + \Gamma}{1 - \Gamma} \right)^2 = C_1 \dots\dots\dots (2-14)$$

And from (2-8) we define

$$\mu_r \epsilon_r = - \left[\frac{c}{wd} \ln \left(\frac{1}{\Gamma} \right) \right]^2 = C_2 \dots\dots\dots (2-15)$$

$$\text{Then } \mu_r = \sqrt{C_1 C_2} \dots\dots\dots (2-16)$$

$$\epsilon_r = \sqrt{\frac{C_2}{C_1}} \dots\dots\dots (2-17)$$

2.5 Maxwell's Equations

Maxwell's equations describe all (classical) electromagnetic phenomena:

$$\vec{\nabla} \times \vec{E} = -\frac{\partial \vec{B}}{\partial t} \dots\dots\dots (2-18)$$

$$\vec{\nabla} \times \vec{H} = \frac{\partial \vec{D}}{\partial t} + \vec{J} \dots\dots\dots (2-19)$$

$$\vec{\nabla} \cdot \vec{D} = \rho \dots\dots\dots (2-20)$$

$$\vec{\nabla} \cdot \vec{B} = 0 \dots\dots\dots (2-21)$$

The first is Faraday's law of induction; the second is Ampere's law as amended by Maxwell to include the displacement current $\partial D/\partial t$, the third and fourth are Gauss' laws for the electric and magnetic fields. The displacement current term $\partial D/\partial t$ in Ampere's law is essential in predicting the existence of propagating electromagnetic waves.

The quantities E and H are the electric and magnetic field intensities and are measured in units of [volt/m] and [Ampere/m], respectively. The quantities D and B are the electric and magnetic flux densities and are in units of [coulomb/m²] and [Weber/m²], or [Tesla]. D is also called the electric displacement, and B, the magnetic induction. The quantities ρ and J are the volume charge density and electric current density (charge flux) of any external charges (that is, not including any induced polarization charges and currents.) They are measured in units of [coulomb/m³] and [Ampere/m²][32].

The electric and magnetic flux densities D , B are related to the field intensities E , H via the so-called constitutive relations, whose precise form depends on the material in which the fields exist. In vacuum, they take their simplest form [33]:

$$\vec{D} = \epsilon_0 \vec{E} \dots\dots\dots (2-22)$$

$$\vec{B} = \mu_0 \vec{H} \dots\dots\dots (2-23)$$

$$\vec{J} = 0 \dots\dots\dots (2-24)$$

Where ϵ_0 and μ_0 are the permittivity and permeability of vacuum, with numerical values: [34,35]

$$\epsilon_0 = 8.854 \times 10^{-12} \text{ Farad/m}$$

$$\mu_0 = 4\pi \times 10^{-7} \text{ Henry/m}$$

And for the medium

$$\vec{D} = \epsilon \vec{E} \dots\dots\dots (2-25)$$

$$\vec{B} = \mu \vec{H} \dots\dots\dots (2-26)$$

$$\vec{J} = \sigma \vec{E} \dots\dots\dots (2-27)$$

Where ϵ permittivity, μ permeability and σ conductivity of medium where [36,37]:

$$\epsilon = \epsilon_0 \epsilon_r \dots\dots\dots (2-28)$$

$$\mu = \mu_0 \mu_r \dots\dots\dots (2-29)$$

This is mean

$$\epsilon_r = \frac{\epsilon}{\epsilon_0} \dots\dots\dots (2-30)$$

$$\mu_r = \frac{\mu}{\mu_0} \dots\dots\dots (2-31)$$

where ϵ_r is called Relative Electric Permittivity or called Dielectric Constant and μ_r called Relative Magnetic permeability which is function of

Temperature and frequency [38,39] the complex form of ϵ_r and μ_r may be written as: [40,41]

$$\epsilon_r^* = \epsilon' - j\epsilon'' \dots\dots\dots (2-32)$$

$$\mu_r^* = \mu' - j\mu'' \dots\dots\dots (2-33)$$

Where: ϵ_r^* complex value of relative permittivity, μ_r^* complex value of relative permeability. ϵ' , ϵ'' it is the real and imaginary part of permittivity, μ' and μ'' it is the real and imaginary part of permeability.

2.6 Electromagnetic Waves Propagation

Electromagnetic Waves Propagate in Different Media like free space, homogenous medium and Inhomogeneous medium and this Propagate depend on many parameters like permittivity, permeability and electrical conductivity and the value of these parameters depends on frequency of electromagnetic waves [33].

2.7 Propagation in free space

In free space $J = 0$, $\rho = 0$ therefore Maxwell's equations become [33]:

$$\vec{\nabla} \times \vec{E} = -\frac{\partial \vec{B}}{\partial t} \dots\dots\dots (2-34)$$

$$\vec{\nabla} \times \vec{H} = \frac{\partial \vec{D}}{\partial t} \dots\dots\dots (2-35)$$

$$\vec{\nabla} \cdot \vec{D} = 0 \dots\dots\dots (2-36)$$

$$\vec{\nabla} \cdot \vec{B} = 0 \dots\dots\dots (2-37)$$

From above equation and from equations (2-22, 2-24) we can get:

$$\nabla^2 E = \epsilon_0 \mu_0 \frac{\partial^2 \vec{E}}{\partial t^2} \dots\dots\dots (2-38)$$

$$\nabla^2 H = \epsilon_0 \mu_0 \frac{\partial^2 \vec{H}}{\partial t^2} \dots\dots\dots (2-39)$$

and the Impedance for the free space is

$$Z_0 = \sqrt{\frac{\mu_0}{\epsilon_0}} = 377 \Omega \dots\dots\dots (2-40)$$

2.8 Propagation through a homogenous medium

The equations of electromagnetic Waves for nonconductive homogenous medium, when the conductivity equal to zero is as follow [33]:

$$\nabla^2 E = \mu \epsilon \frac{\partial^2 \vec{E}}{\partial t^2} \dots\dots\dots (2-41)$$

$$\nabla^2 H = \mu \epsilon \frac{\partial^2 \vec{H}}{\partial t^2} \dots\dots\dots (2-42)$$

and the Impedance of medium is [42]:

$$Z = \sqrt{\frac{\mu}{\epsilon}} \dots\dots\dots (2-43)$$

And the velocity of propagate in homogeneous isolated with lossless is:

$$v = \frac{1}{\sqrt{\mu \epsilon}} \dots\dots\dots (2-44)$$

For the conductive medium equations (2-41) and (2-42) becomes [33]:

$$\nabla^2 E = \mu \epsilon \frac{\partial^2 \vec{E}}{\partial t^2} + \mu \sigma \frac{\partial \vec{E}}{\partial t} \dots\dots\dots (2-45)$$

$$\nabla^2 H = \mu \epsilon \frac{\partial^2 \vec{H}}{\partial t^2} + \mu \sigma \frac{\partial \vec{H}}{\partial t} \dots\dots\dots (2-46)$$

Maxwell's Equations (2-18) to (2-21) can be written in the phase form as

$$\vec{\nabla} \times \vec{H} = j\omega\vec{D} + \vec{J} \quad \dots\dots\dots (2-47)$$

$$\vec{\nabla} \times \vec{E} = -j\omega\vec{B} \quad \dots\dots\dots (2-48)$$

$$\vec{\nabla} \cdot \vec{D} = \rho \quad \dots\dots\dots (2-49)$$

$$\vec{\nabla} \cdot \vec{B} = 0 \quad \dots\dots\dots (2-50)$$

Also the equations (2-45) and (2-46) may be written in the phase form as shown [33]

$$\nabla^2 E = -\omega^2\mu\epsilon \vec{E} + j\omega\sigma\mu \vec{E} = \gamma^2\vec{E} \quad \dots\dots\dots (2-51)$$

$$\nabla^2 H = -\omega^2\mu\epsilon \vec{H} + j\omega\sigma\mu \vec{H} = \gamma^2\vec{H} \quad \dots\dots\dots (2-52)$$

Where γ is wave propagation constant in the conductive medium and from equation (2-52) we get [33]:

$$\gamma = \sqrt{-\omega^2\mu\epsilon + j\omega\sigma\mu} \quad \dots\dots\dots (2-53)$$

And the complex form of propagation constant is

$$\gamma = \alpha + j\beta \quad \dots\dots\dots (2-54)$$

Where α is attenuation constant and β is phase constant and from equations (2-53) and (2-54) we get [33]:

$$\alpha = \text{Real}\{\sqrt{-\omega^2\mu\epsilon + j\omega\sigma\mu}\} \quad \dots\dots\dots (2-55)$$

$$\beta = \text{Imag}\{\sqrt{-\omega^2\mu\epsilon + j\omega\sigma\mu}\} \quad \dots\dots\dots (2-56)$$

2.9 The electric and magnetic loss

From the Maxwell Equation (2-19) and the equations from (2-25) to (2-27) we get [33]:

$$\vec{\nabla} \times \vec{H} = \frac{\partial(\epsilon\vec{E})}{\partial t} + \sigma \vec{E} \quad \dots\dots\dots (2-57)$$

This equation in phase form written as

$$\vec{\nabla} \times \vec{H} = j\omega\epsilon\vec{E} + \sigma \vec{E} \quad \dots\dots\dots (2-58)$$

From above equation we get

$$\vec{\nabla} \times \vec{H} = j\omega(\epsilon - j \frac{\sigma}{\omega})\vec{E} \quad \dots\dots\dots (2-59)$$

Where

$$\epsilon^* = \epsilon - j \frac{\sigma}{\omega} \quad \dots\dots\dots (2-60)$$

Where ϵ^* called Complex Dielectric Constant and the equation (2-60) may be rewrite able as:

$$\epsilon^* = \epsilon_0(\epsilon' - j\epsilon'') \quad \dots\dots\dots (2-61)$$

The imaginary part ϵ'' represents the value of the loss factor

$$\epsilon'' = \frac{\sigma}{\epsilon_0\omega} \quad \dots\dots\dots (2-62)$$

Equation (2-61) can be written as:

$$\epsilon^* = \epsilon_0\epsilon_r \quad \dots\dots\dots (2-63)$$

This mean

$$\epsilon_r = \frac{\epsilon^*}{\epsilon_0}$$

$$\epsilon_r = \epsilon' - j\epsilon'' \dots\dots\dots (2-64)$$

Where

$$\epsilon' = \text{Re}\left(\frac{\epsilon^*}{\epsilon_0}\right) \quad \text{It is the real part for Dielectric constant}$$

$$\epsilon'' = -\text{Im}\left(\frac{\epsilon^*}{\epsilon_0}\right) \quad \text{It is the imaginary part for Dielectric constant}$$

And the equation (2-60) can be written as [33]:

$$\epsilon_r = \epsilon'(1 - j\tan\delta_\epsilon) \dots\dots\dots (2-65)$$

Where

$$\tan\delta_\epsilon = \frac{\epsilon''}{\epsilon'} \dots\dots\dots (2-66)$$

Where δ_ϵ is called dielectric loss angle and $\tan\delta_\epsilon$ is called dielectric loss tangent and the same method us to write the complex permeability [43] as:

$$\mu^* = \mu_0 \mu_r \dots\dots\dots (2-67)$$

$$\mu^* = \mu_0 (\mu' - j\mu'') \dots\dots\dots (2-68)$$

Where

$$\mu_r = \mu' - j\mu'' \dots\dots\dots (2-69)$$

$$\mu_r = \mu'(1 - j\frac{\mu''}{\mu'}) \dots\dots\dots (2-70)$$

$$\mu_r = \mu'(1 - j\tan\delta_m) \dots\dots\dots (2-71)$$

Where

μ^* Complex permeability

μ' Real part of complex permeability

μ'' Imaginary part of complex permeability

δ_m Magnetic loss angle

$\tan\delta_m$ Magnetic loss tangent

2.10 Absorbent Material $\mu = \epsilon$

Harmonization occurs between free space and absorbent material when the reflection coefficient of the Electromagnetic radiation falling on material equal to one this means that all the radiation penetrates absorbent material and this requires to be the Impedance of free space equal to the Impedance of absorbent material. In other words [33,44 ,45]:

$$Z = Z_0 \dots\dots\dots (2-72)$$

And this leads to

$$\sqrt{\frac{\mu_r}{\epsilon_r}} = 1 \dots\dots\dots (2-73)$$

And from this equation we get

$$\mu_r = \epsilon_r \dots\dots\dots (2-74)$$

And such an equation that verify this condition called absorbent material $\mu = \epsilon$ and for the material, which is general type the loss is composed of two types dielectric loss and magnetic loss and the Impedance as follows [33] :

$$Z = \sqrt{\frac{\mu_0 \mu' (1 - j \tan \delta_m)}{\epsilon_0 \epsilon' (1 - j \tan \delta_\epsilon)}} = 1 \quad \dots\dots\dots (2-75)$$

2.11 Absorption Mechanisms

Radar absorbing materials absorb energy from the electromagnetic fields passing through them. Similar to a resistor that consumes energy of an electric current, RAM dissipates the absorbed EM energy into heat. Since EM wave has an electric and magnetic component, it is common to separate dielectric and magnetic absorption mechanisms. Using Gauss's and Ampere's laws formulated in (2-18) to (2-21) we can derive the energy stored in the electric and magnetic fields of an absorbed EM wave. The energy densities inside the absorber are

$$U_e = \frac{1}{2} \epsilon_A \epsilon_0 |E|^2 \quad \dots\dots\dots (2-76)$$

$$U_m = \frac{1}{2 \mu_A \mu_0} |B|^2 \quad \dots\dots\dots (2-77)$$

It follows that relative permittivity ϵ_A and permeability μ_A define RAM's electromagnetic loss. Both numbers are complex and depend on the frequency of an electromagnetic wave

$$\epsilon_A(f) = \epsilon'_A + i\epsilon''_A \quad \dots\dots\dots (2-78)$$

$$\mu_A(f) = \mu'_A + i\mu''_A \quad \dots\dots\dots (2-79)$$

Where the real part is a measure of how much energy from an external electric/- magnetic field is stored in a material; the imaginary part called the loss factor and is a measure of how dissipative or lossy a material is to an external electric/magnetic field. Because the absorber's conductivity σ is often the major loss mechanism, it is convenient to express this effect in terms of ϵ''_A

$$\varepsilon''_A = \frac{\sigma}{\omega \varepsilon_0} \dots\dots\dots (2-80)$$

Where $\omega = 2\pi f$ is the radian frequency.

We can rewrite (2-78) and (2-79) in polar notation

$$\varepsilon_A(f) = |\varepsilon_A| e^{i\delta_e} \dots\dots\dots (2-81)$$

$$\mu_A(f) = |\mu_A| e^{i\delta_m} \dots\dots\dots (2-82)$$

Where δ_e and δ_m are the electric and magnetic loss tangents given by

$$\tan \delta_e = \frac{\varepsilon''_A}{\varepsilon'_A} \dots\dots\dots (2-83)$$

$$\tan \delta_m = \frac{\mu''_A}{\mu'_A} \dots\dots\dots (2-84)$$

We can interpret loss tangent as a ratio of energy lost per cycle to energy stored per cycle.

2.11.1 Electric field loss

Absorption of electric field in matter is due to the number of dielectric mechanisms or polarization effects that contribute to the overall permittivity ε_A . In a microwave region, the loss is caused primarily by the dielectric relaxation effects associated with permanent and induced molecular dipoles. The electrical field E creates a torque T on the electric dipole, and the dipole rotates to align with the electric field, thus creating orientation polarization (Fig.2.2). At low frequencies electric field changes slowly and the dipole has enough time to align, but at microwave frequencies dipole's alignment starts to lag due to the viscosity of the material.

The friction accompanying the alignment of the dipole leads to energy dissipation in a form of heat. Water is an example of a substance that exhibits strong orientation polarization (H_2O is a polar molecule, meaning it has a permanent dipole moment) and that is why food heats in a microwave oven.

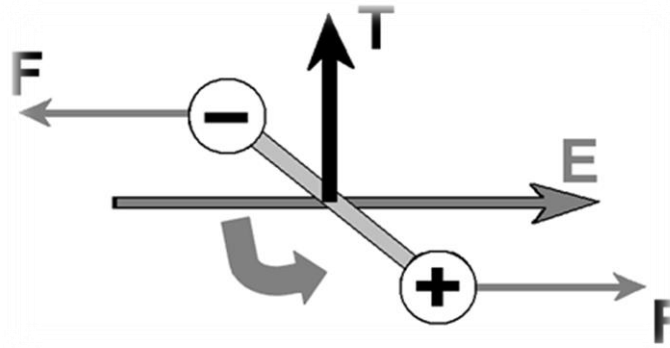


Figure (2.2): Dipole alignment with an electric field.

In terms of permittivity, the rotation of dipoles leads to a variation in both ϵ'_A and ϵ''_A at the relaxation frequency f_c , which is related to the time τ (called "relaxation time") required for an aligned dipole in an electric field to return to $1/e$ of its random equilibrium value

$$\tau = \frac{1}{2\pi f_c} \dots\dots\dots (2-85)$$

At frequencies below f_c when dipoles can keep up with the a pace of field variations, the loss ϵ''_A is directly proportional to the frequency. As the frequency increases ϵ''_A continues to increase, but the storage of electric energy ϵ'_A begins to drop due to the lack of alignment between the dipole and an electric field. At frequencies above f_c the field is oscillating too fast to affect polarization, so both parts of a complex permittivity decrease. The described dependency of permittivity as function of frequency for ideal dipoles is known as Debye relaxation model (Fig.2.3) one other type of polarization we need to

Consider in our study of microwave absorption in nanostructures is interfacial or space charge polarization. When an absorber is made of more than one material (heterogeneous system), the free charge carriers cannot fully migrate through the material in the presence of an electric field. The carriers can be trapped within the absorber's interfaces and cause the accumulation of charges, which distorts the electric field and increases the overall material's capacitance, thereby increasing ϵ'_A [46].

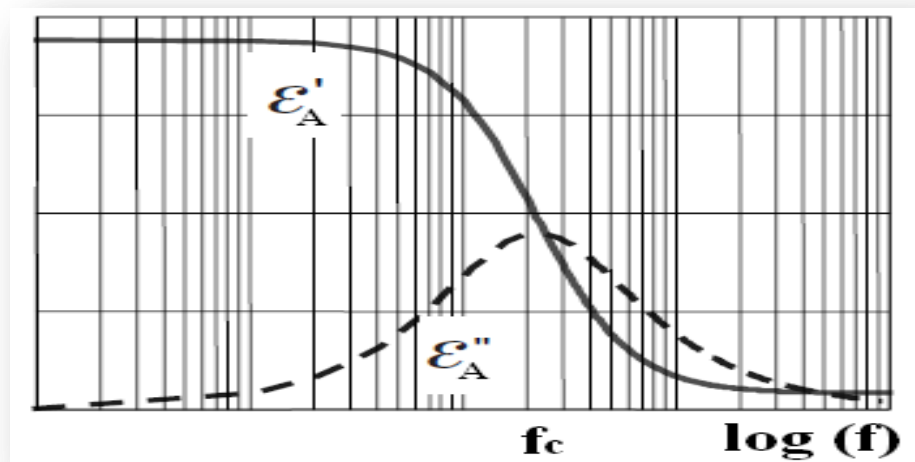


Figure (2.3): Debye relaxation spectra [47].

2.11.2 Magnetic field loss

Ferrites are iron oxide based compounds commonly employed as magnetic absorbers in RAM design. Similar to the absorption of an electric field, different magnetic loss mechanisms dominate at different frequencies. At lower frequencies of magnetic field energy is dissipated as heat caused by the magnetic dipoles re-alignment [48].

This phenomenon known as hysteresis reflects the non-linear relationship between the applied magnetic field intensity H and the magnetization of

The material M. The two important parameters of this loss mechanism are saturation magnetization (maximum possible magnetization of the material) and coercivity (field required to reduce magnetization to zero) Fig (2.4).

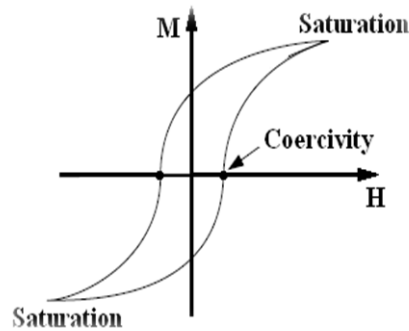


Figure (2.4): Hysteresis loop.

As we have seen in (2-80) and (2-83) material's conductivity increase with the electric loss. It also plays an important role in a magnetic loss due to the eddy currents. For eddy currents to occur material has to have a large conductivity and thickness larger than the skin depth δ , which is defined as the depth of penetration of the magnetic field at which its value decreases by $1/e$ of its surface value ($\delta = \sqrt{\frac{2}{\sigma\omega\mu}}$). From the Maxwell's Equation in (2-18),(2-19),(2-20),(2-21) it follows that the alternating magnetic field generates an electric field that drives the charge carriers via the Lorentz force ($F_L = qE$). The resulting eddy current dissipates energy in a form of heat. However, as any other alternating current, it also re-emits an EM wave that can be easily detected - this makes metals highly reflective.

In a microwave region the residual losses due to resonance effects often dominate [49]. The resonance phenomenon has two distinct loss mechanisms: magnetic domain wall resonance and ferromagnetic resonance.

A magnetic domain is a region within a material that has magnetic moments of atoms aligned in one direction that creates a uniform magnetization within a domain. When an external magnetic field is applied the domain's wall is slightly displaced and the lattice strain creates the restoring force. Since the wall has inertia the movement is accompanied by energy dissipation and an equation of motion can be written for a sinusoidal applied field [48]

$$m\ddot{x} + \beta\dot{x} + kx = 2M_s B(t) \dots\dots\dots(2-86)$$

where x is the displacement normal to the wall, m is inertia, β is a damping coefficient, k is a stiffness coefficient, M_s is a saturation magnetization, and $B(t)$ is an alternating magnetic field. Equation (2-86) describes a damped harmonic oscillation and, if damping is small, a resonance effect will occur at

$$\text{a frequency } \omega = \sqrt{\frac{k}{m}}.$$

In ferromagnetic and ferrimagnetic materials, the spin of an electron combined with its electric charge results in a magnetic dipole moment and creates a magnetic field that contributes to the overall material's magnetization. Since the magnetic moment is associated with an angular momentum, in a static magnetic field the electron experiences a torque and processes around the field direction with the Larmor angular frequency

$$f_L = \frac{\gamma \mu_0}{2\pi} H = 35.2 \times 10^6 \text{ H (GHz)} \dots\dots\dots(2-87)$$

Where γ is the gyroscopic ratio ($\gamma = \frac{g \mu_B}{h} = 1.76 \times 10^{11} \text{ T}^{-1} \text{S}^{-1}$), H is the magnetic field (A/m) [48]. If a microwave field of resonance frequency f_L is applied perpendicular to the direction of the static field H ,

Then the torque will cause the angle of precession to increase, so the energy of the microwave field will be absorbed. When a microwave field is removed the precessional energy will be dissipated, and the magnetization vector gradually spirals towards the direction of the static field (Fig.2.5).



Figure (2.5): Precessional motion of magnetization: (a) precession maintained by an applied microwave field $H \text{ GHz}$; (b) M_s spiraling into line with H as the precessional energy is dissipated [48].

In summary, it is important to note that as we have seen magnetic loss mechanisms are intrinsically narrow band. Furthermore, the losses are greater at the lower frequencies, and at the higher frequencies the electric properties of a material account for the electromagnetic absorption. Since relative permittivity and permeability account for the loss mechanisms, we can graphically illustrate their approximate behavior in a microwave region (Fig.2.6).

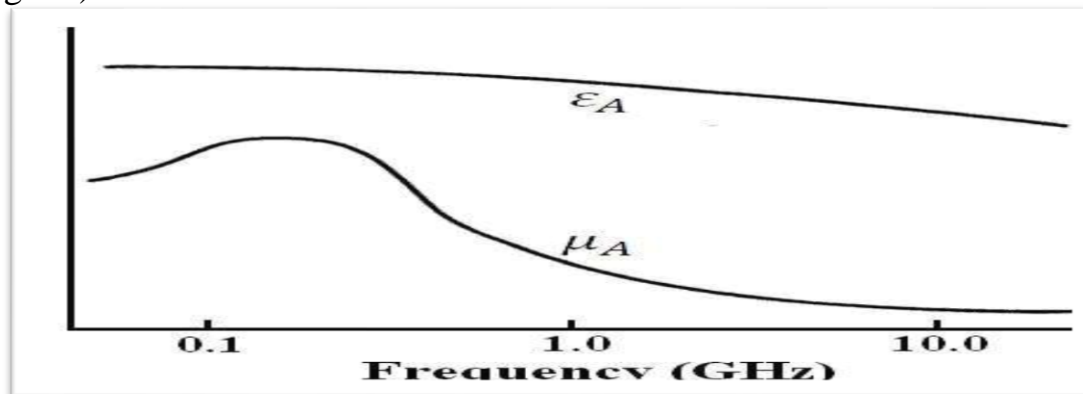


Figure (2.6): Schematic illustration of the frequency behavior of ferrites [50].

2.12 Origin of Magnetism

A magnetic field is a force field similar to gravitational and electrical fields that is surrounding a source of potential; there is a contoured sphere of influence or field. The origin of the magnetic potential is known as magnetic dipoles. Magnetism basically results from two electronic motions accompanying with the atom; the orbital motion of the electron and the spin motion of the electron. For macroscopic purposes these small currents due to these motions can be consider as magnetic dipoles, as a rule they cancel each other out due to the random orientation of the atoms. But when a magnetic field is applied, a net alignment of these magnetic dipoles implement and the medium becomes magnetically polarized [51-52].

The intensity of magnetic field which magnetizes the material is measured by magnetic field (H), B is termed as the magnetic induction or magnetic flux density inside the magnetized material. The magnetic moment per unit volume of the magnetized material is measured by magnetization M , The magnetization M is the sum of the magnetic moments m_j per unit volume.

$$M = \sum_{\text{volume}} m_j \dots\dots\dots (2-88)$$

The magnetic characteristic of magnetic materials is described not only by the magnitude and sign of M , but also the way in which M varies with H . The ratio of these two quantities is called magnetic susceptibility.

$$\chi = \frac{M}{H} \dots\dots\dots (2-89)$$

The magnetization M of a material is expressed by the relation:

$$B = \mu_0 (H + M) = \mu_r \mu_0 H = \mu H \dots\dots\dots (2-90)$$

Where $\mu_o = 4\pi \times 10^{-7} \text{ Hm}^{-1}$ is the permeability of free space and B and H are measured in Tesla (T) and Am^{-1} respectively. μ_r is termed as the relative permeability of the material, subsequently from the relations (2-89) and (2-90), it can be shown that:

$$\mu = \mu_o(1 + \chi) \dots\dots\dots (2-91)$$

The value of χ and μ_r characterizes the magnetic properties of a material.

2.13 Types of Magnetic Materials

When a material is placed within a magnetic field, the magnetic forces of the material's electrons will be affected. This effect is known as Faraday's Law of Magnetic Induction. However, materials can react quite differently to the presence of an external magnetic field.

This reaction depends on a number of factors, such as the atomic and molecular structure of the material, and the net magnetic field associated with the atoms.

The magnetic moments associated with atoms are the electron orbital motion, the change in orbital motion caused by an external magnetic field, and the spin motion of the electron. Some materials acquire a magnetization parallel to B (Paramagnets) and some opposite to B (Diamagnets) [53].

In most atoms, electrons occur in pairs. Electrons in a pair spin in opposite directions. When electrons are paired together, their opposite spins cause their magnetic fields to cancel each other.

Therefore, no net magnetic field exists. Alternately, materials with some unpaired electrons will have a net magnetic field and will react more to an external field.

Most materials can be classified as diamagnetic, paramagnetic or ferromagnetic, Figure (2.7) showing different kinds of magnetic materials.

Magnetic materials can also be classified in terms of their magnetic properties and uses.

If a material is easily magnetized and demagnetized then, it is referred to as a soft magnetic material, whereas if it is difficult to demagnetize, then it is referred to as hard (permanent) magnetic material.

Materials in between hard and soft are almost exclusively used as recording media and have no other general term to describe them. Other classifications for types of magnetic materials are subset of soft or hard materials.

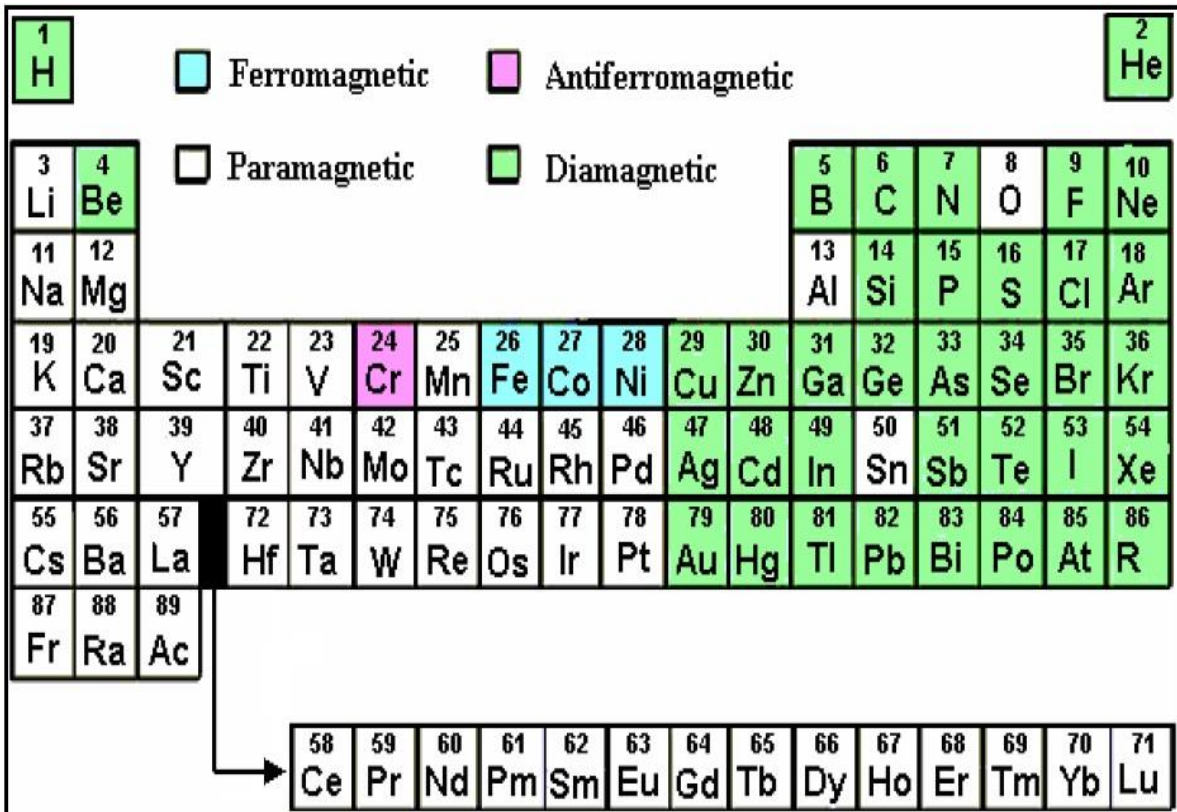


Figure (2.7): Periodic table showing different kinds of magnetic materials [53].

2.13.1 Diamagnetism

Diamagnetic substances consist of atoms or molecules with no net angular momentum. When an external magnetic field is applied, there creates a circulating atomic current that produces a very small bulk magnetization opposing the applied field [54].

Diamagnetism is exhibited by all common materials but so feeble that it is covered if material also exhibits paramagnetism or ferromagnetism [55].

When a material is placed in a magnetic field, electrons in the atomic orbitals tend to oppose the external magnetic field by moving the induced magnetic moment in a direction opposite to the external magnetic field. Due to this fact, the material is very weakly repelled in the magnetic field.

This is known as diamagnetism. The induced dipole moments disappear when the external field is removed. The diamagnetic effect in a material can be observed only if the paramagnetic effect or the ferromagnetic effect does not hide the weak diamagnetic effect. Diamagnetism can be understood through Figures (2.8) (a) and (b). In the absence of the external magnetic field, the atoms have zero magnetic moment as shown in Fig. (2.8a).

But when an external magnetic field H_0 is applied in the direction as shown in Figure (2.8) (b), the atoms acquire an induced magnetic moment in the direction opposite to that of the field.

Diamagnetic materials have very small negative susceptibility. Due to this fact, a diamagnetic material is weakly repelled in the magnetic field. When the field is removed, its magnetization becomes zero. Examples of some diamagnetic materials are gold, silver, mercury, copper and zinc [56].

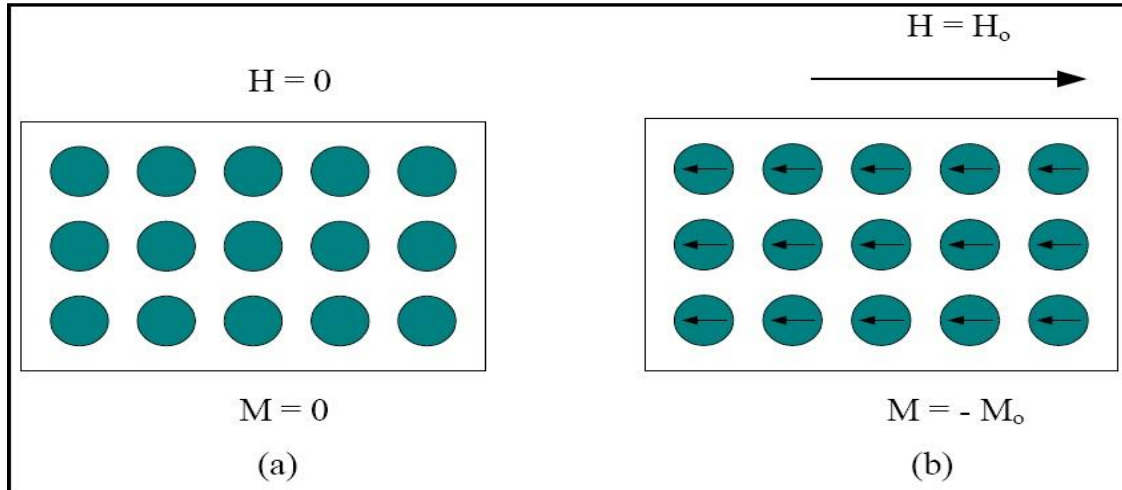


Figure (2.8): (a) Diamagnetic material: The atoms do not possess magnetic moment. When $H=0$: so $M=0$. (b) When a magnetic field H_0 is applied, the atoms acquire induced magnetic moment in a direction opposite to the applied field that results a negative susceptibility [53].

2.13.2 Paramagnetism

In certain materials, each atom or molecule possess permanent magnetic moment individually due to its orbital and spin magnetic moment. In the absence of an external magnetic field, the individual atomic magnetic moments are randomly oriented.

The net magnetic moment and the magnetization of the material becomes zero. But when an external magnetic Field is applied, the individual atomic magnetic moments tend to align themselves in the direction of externally applied magnetic field and results into a nonzero weak magnetization as shown in Figure (2.9) (a) and (b). Such materials are paramagnetic materials and phenomenon is called paramagnetism [56].

Paramagnetism occurs in materials with permanent magnetic dipole moment, such as atomic or molecular with an odd number of electrons, atoms or ions in unfilled orbitals.

Paramagnetism is found in atoms, molecules & lattice defects possessing an odd number of electrons as the total spin of the system can't be zero.

Metals, free atoms & ions with partly filled inner shell, transition elements and few compounds with an even number of electrons including oxygen also show paramagnetism [57].

Paramagnetic materials are attracted when subjected to an applied magnetic field. Paramagnetic materials also exhibit diamagnetism, but the latter effect is typically very small.

These materials show weak magnetism in the presence of an external magnetic field but when the field is removed, thermal motion will quickly disrupt the magnetic alignment. These materials have very weak and positive magnetic susceptibility to an external magnetic field.

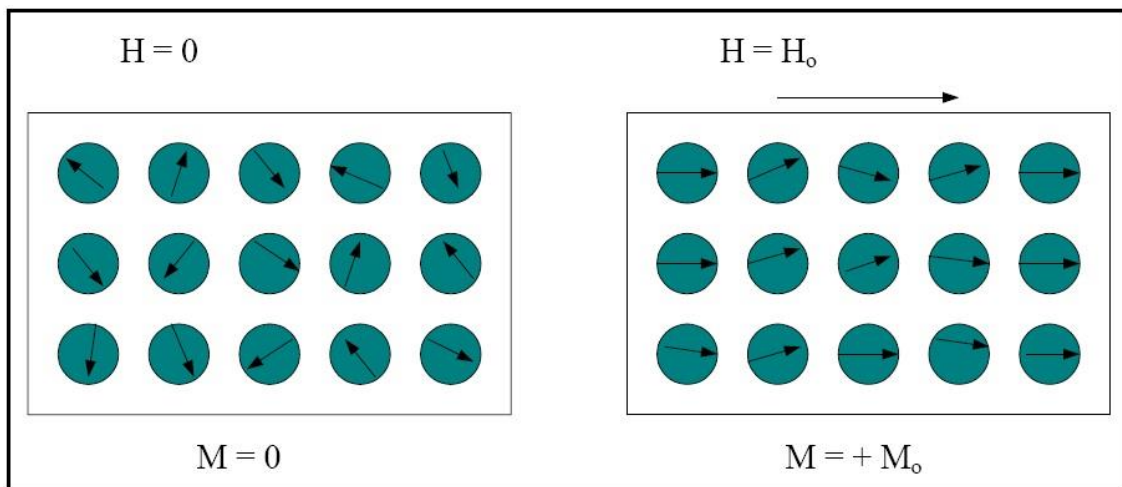


Figure (2.9): (a) Paramagnetic material: Each atom possesses a permanent magnetic moment. When $H=0$, all magnetic moments are randomly oriented: so $M=0$. (b) When a magnetic field H_0 is applied, the atomic magnetic moments tend to orient themselves in the direction of the field. That results a net magnetization $M=M_0$ and positive susceptibility the [53].

The alignment of magnetic moments is disturbed by the thermal agitation with the rise in temperature and greater fields are required to attain the same magnetization. As a result paramagnetic susceptibility decreases with the rise in temperature. The paramagnetic susceptibility is inversely proportional to the temperature. It can be described by the relation

$$\chi = \frac{C}{T} \dots\dots\dots (2.92)$$

This is called the Curie Law of paramagnetism. Here χ is the paramagnetic susceptibility, T is the absolute temperature and C is called the Curie constant. Examples of paramagnetic elements are aluminum, calcium, magnesium and sodium [56].

2.13.3 Ferromagnetism

Ferromagnetism is a phenomenon of spontaneous magnetization. It has the alignment of an appreciable fraction of molecular magnetic moments in some favorable direction in the crystal. Ferromagnetism appears only below a certain temperature, known as Curie temperature. Above Curie temperature, the moments are randomly oriented resulting the zero net magnetization [58]. Ferromagnetism is only possible when atoms are arranged in a lattice and the atomic magnetic moment can interact to align parallel to each other (Fig. 2.10). A ferromagnetic material has spontaneous magnetization due to the alignment of its atomic magnetic moments even in the absence of external magnetic field [56]. Examples of ferromagnetic materials are transition metals Fe, Co and Ni, but other elements and alloys involving transition or rare-earth elements are also ferromagnetic due to their unfilled 3d and 4f shells. These materials have a large and positive magnetic susceptibility to an external magnetic field. They exhibit a strong attraction to magnetic fields and are able to retain their magnetic properties after the external field is removed.

When ferromagnetic materials are heated, then due to thermal agitation of atoms the degree of alignment of the atomic magnetic moment decreases, eventually the thermal agitation becomes so great that the material becomes paramagnetic. The temperature of this transition is the Curie temperature, T_c (Fe: $T_c = 770$ °C, Co: $T_c = 1131$ °C and Ni: $T_c = 358$ °C). Above T_c the magnetic susceptibility varies according to the Curie-Weiss law [56].

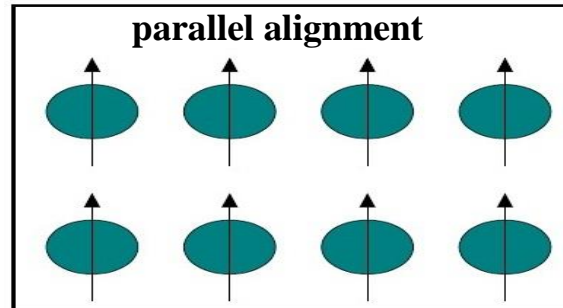


Figure (2.10): Ferromagnetism [53].

2.13.4 Antiferromagnetism

Antiferromagnetic materials are those in which the dipoles have equal moments, but adjacent dipoles point in opposite directions [58]. There are also materials with more than two sub lattices with triangular, canted or spiral spin arrangements. Due to these facts, antiferromagnetic materials have small non-zero magnetic moment [59]. They have a weak positive magnetic susceptibility of the order of paramagnetic material at all temperatures, but their susceptibilities change in a peculiar manner with temperature.

The theory of antiferromagnetism was developed chiefly by Néel in 1932. Chromium is the only element exhibiting antiferromagnetism at room temperature [58]. Antiferromagnetic materials are very similar to ferromagnetic materials but the exchange interaction between neighboring atoms leads to the anti-parallel alignment of the atomic magnetic moments (Fig. 2.11). Therefore the magnetic field cancels out and the material appears to behave in the same way as the paramagnetic material.

The antiparallel arrangement of magnetic dipoles in antiferromagnetic materials is the reason for small magnetic susceptibility of antiferromagnetic materials. Like ferromagnetic materials, these materials become paramagnetic above transition temperature, known as the Néel temperature, T_N (Cr: $T_N = 37$ °C).

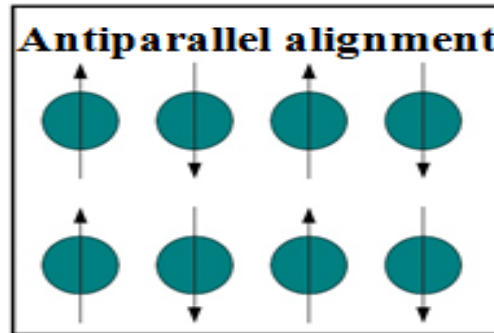


Figure (2.11): Antiferromagnetism [53]

2.13.5 Ferrimagnetism

Ferrimagnetic materials have spin structure of both spin-up and spin-down components but have a net non-zero magnetic moment in one of these directions [60]. The magnetic moments of the atoms on different adjacent sub lattices are opposite to each other as in antiferromagnetism; however, in ferrimagnetic materials the opposing moments are unequal (Fig. 2.12). This magnetic moment may also be due to more than two sub lattices and triangular or spiral arrangements of sub lattices [61].

Ferrimagnetism is only observed in compounds, which have more complex crystal structures than pure elements. These materials, like ferromagnetic materials, have a spontaneous magnetization below a critical temperature called the Curie temperature (T_c). The magnitude of magnetic susceptibility for ferromagnetic and ferrimagnetic materials is similar, however the alignment of magnetic dipole moments is drastically different.

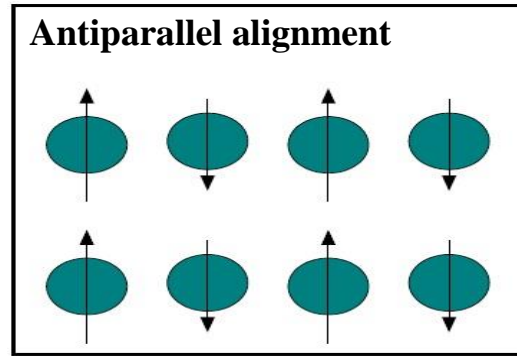


Figure (2.12): Ferrimagnetism [53].

2.14 Types of Ferrites depending on their magnetic properties

There are two types of ferrites:

1. Soft ferrites.
2. Hard ferrites.

2.14.1 Soft Ferrites

Easily magnetized or demagnetized is characteristic for soft Ferrites. This infers that soft magnetic materials possess low coercive field and high magnetization that is desired in various applications.

The hysteresis loop for a soft ferrite must be small; so the energy losses are very low for examples, Ni, Co and Fe, manganese etc. They are used in microwave devices, inductors, transformer cores, and recording heads.

Soft ferrites possess certain features over other electromagnetic materials inclusive high electrical resistivity and low eddy current losses over a broad range of frequencies. They have high permeability and are stable over a wide temperature range. These advantages make soft ferrites substantial over all other magnetic materials [56].

2.14.2 Hard Ferrites

Difficulty in magnetize or demagnetize is characteristic for hard Ferrites. They are utilized as permanent magnets. The hysteresis loop it is a broad and

The coercivity it is so high in the hard ferrite. Examples are rare earth metal alloys, alnico etc. The evolution of permanent magnets started in 1950s with the progression of hard ferrites. The magnets can also be utilized to enough demagnetizing fields and enabling be used for requirements such as permanent magnet motors. The hexagonal ferrite is found in both $\text{BaFe}_{12}\text{O}_{19}$ and $\text{SrFe}_{12}\text{O}_{19}$, but Strontium ferrites have better magnetic properties [56].

Hard ferrites have a hexagonal structure and can be classified as M-, W-, Y-, Z-, X-, U-type ferrites; Table (2-2) shows the types of ferrites and their particular chemical formulae:

Table (2-2): chemical composition and crystallographic building for hexaferrites

-Type	Chemical formula	No. of molecules per unit cell	Crystallographic building per unit cell
M	$\text{BaFe}_{12}\text{O}_{19}$	2	RSR^*S^*
W	$\text{BaMe}_2\text{Fe}_{16}\text{O}_{27}$	2	$\text{RSSR}^*\text{S}^*\text{S}^*$
Y	$\text{Ba}_2\text{Me}_2\text{Fe}_{12}\text{O}_{22}$	3	3(ST)
Z	$\text{Ba}_3\text{Me}_2\text{Fe}_{24}\text{O}_{41}$	2	$\text{RSTSR}^*\text{S}^*\text{T}^*\text{S}^*$
X	$\text{Ba}_2\text{Me}_2\text{Fe}_{28}\text{O}_{46}$	3	3($\text{RSR}^*\text{S}^*\text{S}^*$)
U	$\text{Ba}_4\text{Me}_2\text{Fe}_{36}\text{O}_{60}$	1	$\text{RSR}^*\text{S}^*\text{T}^*\text{S}^*$

Table 2-2 also lists the crystallographic building for each type of hexaferrites. R ($\text{BaFe}_6\text{O}_{11}$), S (Fe_6O_8 or $\text{Me}_2\text{Fe}_4\text{O}_8$) and T ($\text{Ba}_2\text{Fe}_8\text{O}_{14}$) are the building

Blocks of the crystal. R*, S* and T* indicate the blocks obtained by rotating R, S and T through 180° around the vertical axis, respectively [62].

2.15 Structure of $\text{BaFe}_{12}\text{O}_{19}$

The oxygen atoms are closed packed with the A and Fe ions in the interstitial sites. There are ten layers of oxygen atoms along the c axis and the iron atoms are positioned at five crystallographically different sites.

The S (Fe_6O_8) and S* blocks are spinels with 2 oxygen layers and six Fe^{3+} ions. Four of these Fe^{3+} ions are in the octahedral sites with their spins aligned parallel to each other. The remaining two Fe^{3+} ions are in tetrahedral sites and have their spins antiparallel to those that are at the octahedral sites.

As for the hexagonal R ($\text{AFe}_6\text{O}_{11}$) and R* blocks, they consist of three oxygen layers with one of the oxygen anions replaced with an A ion (A= Ba-Sr-Pb). Each R block contains six Fe^{3+} ions, of which five are in octahedral sites, three having spin up and two having spin down [63].

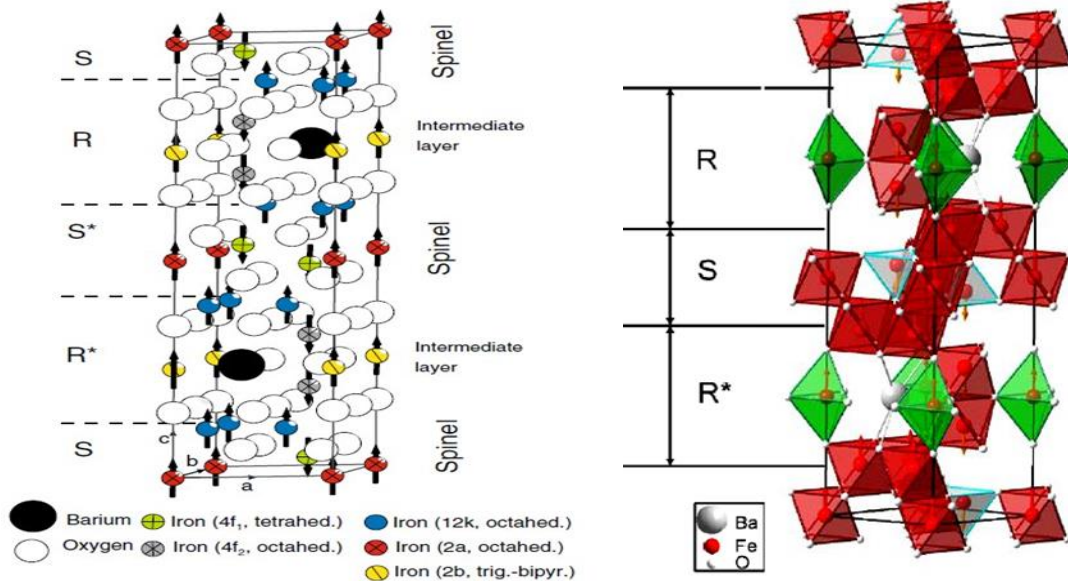


Figure (2.13): Crystal Structure of Barium Hexaferrite ($2\text{BaFe}_{12}\text{O}_{19}$) showing a unit cell and position of ionic sites in the four spinel blocks (SRS*R*) and relative orientation of magnetic moments of Fe^{3+} ions.

2.16 Origin of magnetization in BaFe₁₂O₁₉

In the construction, each Fe³⁺ ion participate 5μB to the magnetic moment at absolute zero, the net magnetization at zero temperature can be computed knowing that (8) Fe³⁺ ions are in the spin up state, and (4) are in spin down state resulting in (4) net spin up Fe³⁺ ions.

Consequently, the total magnetization per molecular unit is (1- 2+ 7- 2) * 5μB= 20μB (One Barium ion for every molecular unit) [63].

Table (2-3) Number of ions per unit formula, coordination and spin direction for the Fe³⁺ cationsublattices of M-type BaM [63]

Lattice sites per unit	Coordination	Number of Fe ³⁺ ions	Block	Spin direction
12k	Octahedral	6	R-S	Up↑
2b	Trigonal–bipyramidal	1	R	Up↑
4f2	Octahedral	2	R	Down↓
4f1	Tetrahedral	2	S	Down↓
2a	Octahedral	1	S	Up↑

2.17 Epoxy resins

Epoxy resins are high-performance thermosetting resins, which display a unique combination of properties. Epoxy resins have been commercially available for almost a half-century. Epoxy resins are arguably one of the most versatile polymers with uses across an enormously wide variety of industries. The outstanding physical properties exhibited by epoxy resins include

- Low cure shrinkage
- No volatiles given off during cure
- Compatibility with a great number of materials
- Strength and durability
- Adhesion
- Corrosion and chemical resistance
- Electrical insulation

The prevailing reason for the broad acceptance of epoxy resins in these important and diverse markets is their capacity to provide a good balance of handling characteristics and ultimate physical properties. They adhere well to a very large variety of substrates, and they generate tough, environmentally resistant films or matrices [64].

2.18 Methods of preparation ferrites

Almost present techniques of solid state chemistry can be utilized to prepared ferrites, leading to various morphologies (particle size, polycrystalline and properties). Several methods have been evolved to prepare ferrites with accurate microstructures; many treatment methods have been mannered as shown in figure (2.14), but are generally branched into two groups:

1- Solid state reaction technique, i.e., conventional ceramic method, includes grinding of ingredients then heating at higher temperatures range. 2- Non-conventional procedure includes formation the powder by wet method among these manners is: organic precursors, Co precipitation, freeze dry, co-spray roasting, sol- gel synthesis, and activated sintering.

The following shows certain methods of preparation ferrites [65]:

2.18.1 Ceramic method

Ceramic method includes the equivalent processes as the classical techniques for production of conventional ceramics. Raw materials are generally iron oxide ($\alpha\text{-Fe}_2\text{O}_3$) and the carbonate or the oxide of the other cations in the required ferrite. A common characteristic of the new manner for powder preparation, many new techniques have been evolved to encroachment the restriction of the ceramic method as shown in figure (2.14) [66].

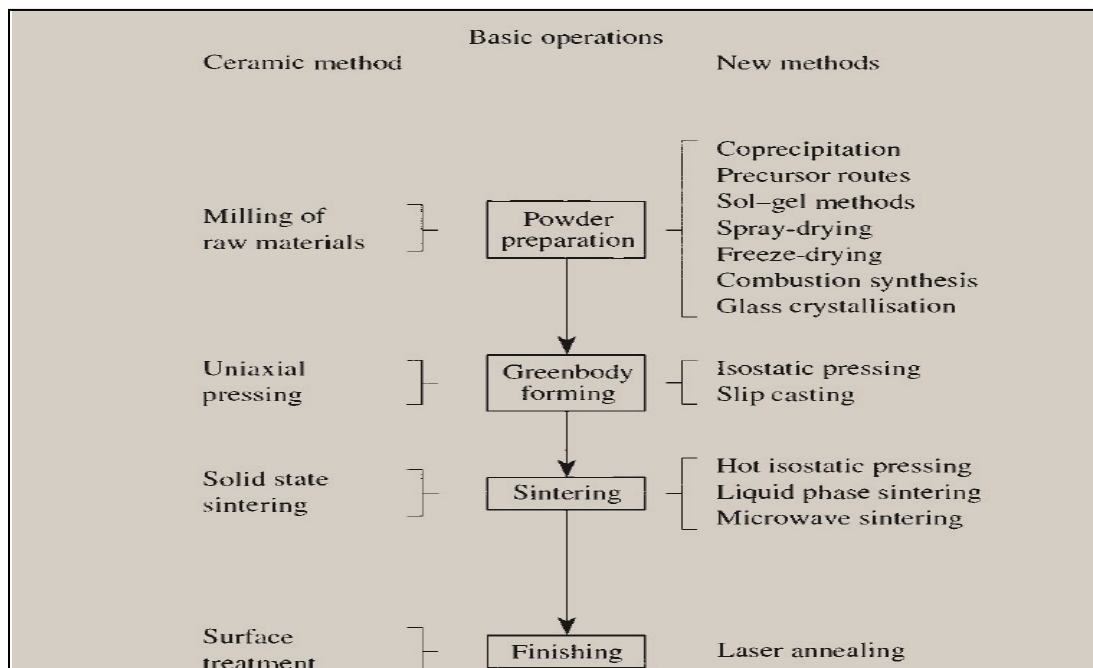


Figure (2.14): The four basic operations in ferrite preparation diagram. Some components of the ceramic method are on the left; on the right, some of the new methods are indicated [66]

2.18.2 Sol-gel method

In this technique, the 'sol' progressively changes to the formation of a gel-like dual phase system including both phase liquid and solid whose morphologies arrangement from incoherent particles to uninterrupted particles. In the status of the colloid, the concentration of particles may low that an important amount of fluid may need to be evaporated so it seems like a gel [67].

To evaporate the remaining liquid phase applies a drying process. The amount at which the dissolvent can be segregate is eventually specified by the distribution of porosity in the gel. Micro-structure of the final synthesis will obviously be virtually influenced by changes imposed onto the structural form through this phase of transformation. After this, a thermal processing or combustion is requisite for further polycondensation. When we do the sintering processes, we observed improve mechanical properties, densification and grain growth, structural stability [68]. The sol-gel method requires low-temperature comparatively so it is economic technique and allows for the accurate control of the product's chemical structure. Sol-gel resulting materials have various utilizations in optics, energy, electronics, space etc... [69].

2.19 Structural Properties

Longstanding XRD used to define the atomic scale structure of materials. The technique is depends on the idea that the wavelength of X-rays is equivalent in size to the spaces between atoms levels. Thus, when a bulk material that shows periodic atomic order, long-range, such as a crystal, is irradiated with X-rays, it acts as an extended, almost perfect grating and produces a diffraction pattern showing numerous sharp spots, called

Bragg diffraction peaks. By measuring and analyzing the positions and intensities of Bragg peaks, it is possible to determine the spatial characteristics of the grating, i.e. to determine the three-dimensional (3D) atomic arrangement in bulk crystals. This is the principle of what is known as "crystal structure" [70].

2.19.1 Debye-Scherrer-Method

The Debye-Scherrer technique utilizes a crystalline powder and it is irradiated with X-rays. The deflected ray is detected via a Geiger-Muller-Tube. The powder patterns consist of small single-crystals, known as crystallites. According to Bragg's equation; (2.93) a set of parallel lattice planes so-called Miller indices (hkl) in a crystallite results in constructive interference from diffracted X-ray beams [71].

$$n \lambda = 2 d \sin \theta \quad \dots\dots\dots (2.93)$$

Where λ - wavelength of x-ray, d -inter planer distance, θ -diffraction angle, $n = 1, 2, 3 \dots$

The grain size can be calculated using the Scherrer's formula (2.94) [72].

$$D = 0.9 \lambda / \beta \cos \theta \quad \dots\dots\dots (2.94) \text{ .Where;}$$

- D it is the regular size of the ordered (crystalline) domains, which probably

Smaller or equivalent to the grain size

- λ it is X-ray wavelength;

- β it is the line broadening at the middle of the maximum intensity (FWHM)

- θ it is the Bragg angle.

2.19.2 Spacing of Lattice Planes

The vertical stretch separating every lattice plane in a bunch is symbolized by the letter d , d wideness and the relationship to the private lattice plane is d_{hkl} (i.e., d_{001} , d_{101} , d_{103}) with the Miller index for the private plane summarized in the subscript, this is the common symbol utilized in X-ray diffraction and crystallography. The magnitude of d spacing with regard to hexagonal systems are shown in the equation (2-95), and for monoclinic systems are shown in equation (2-96) and for cubic systems are shown in equation (2-97) [73].

$$\frac{1}{d^2} = \left[\frac{4}{3a^2} (h^2 + hk + k^2) + \frac{l^2}{c^2} \right] \dots\dots\dots (2.95)$$

The values of d spacing for monoclinic is shown in the equation:

$$\frac{1}{d^2} = \left[\frac{\frac{h^2}{a^2} + \frac{l^2}{c^2} - \frac{2hl \cos \beta}{ac}}{\sin^2 \beta} + \frac{k^2}{b^2} \right] \dots\dots\dots (2.96)$$

The value of d spacing for cubic is shown in the equation:

$$d = \frac{a}{\sqrt{a^2 + k^2 + l^2}} \dots\dots\dots (2.97)$$

2.20 Densities of ferrites

Ferrites, being ceramic formed by sintering had mechanical properties such as pottery and in particular the properties depend on the density. The pressed core before firing contain relatively porous merging on oxides and during sintering the oxides interact to configured crystallites, or grains, of the desired composition, the grains nucleate at disconnected centers and grow around the outside pending the boundaries combined with those of adjacent crystallites

, Meantime this progress of the operation the concentration of the mass increasing. Although there are a few disparities in X-ray densities because of differences in divalent ions, the greater contribution to influential density of ferrite sharing is its porosity [74]. The density of the sample can be measured by knowing the three dimensions of the sample, as shown in the equation below (2-6):

$$d_B = M \text{ (g)} / V \text{ (cm}^3\text{)} \dots\dots\dots (2.98)$$

Where, d_B density, M: mass of sample, V: volume of sample.

2.21 Diameter of grains

The Scherrer equation is used to determine the diameter of grains after smoothing and refining the sintered sample, this is done by enumeration the grains that the straight is extending across the image after enlarge, and then it divides the length of the straight on the number of grains to find the diameter of grain rate.

This test also helps to study the crystalline patterns emerging as well as the study of the form and distribution of crystals. In most employment, data are well-ordered over a chosen area of the surface of the specimen, and a 2-dimensional image it was created that shows spatial distinction in these properties. Areas varies from about 1 cm to 5 microns in width can be illustrated in a scanning mode utilization that technique.

The SEM is also qualified for fulfillment analyses of picked point locations on the specimen; this approach is principally useful in qualitatively or semi-quantitatively definition chemical compositions [75].

2.22 Composites

A composite is consists of two (or more) discrete materials, which is composed of groups, ceramics, metals, and polymers. The objective of a composite is to synthesis a complex of characteristics that is not present by any individual material, and also to combine the best properties of whole of the ingredients materials. A great number of composite categories exist that are performed by different integration of ceramics, metals, and polymers. The biggest advantage of modern composite materials is that they are light as well as strong. By choosing an appropriate combination of matrix and reinforcement material, a new material can be made that exactly meets the requirements of a particular application. Composites also provide design flexibility because many of them can be moulded into complex shapes. The downside is often the cost. Although the resulting product is more efficient, the raw materials are often expensive [76].

2.23 Dielectric Materials

When an electric field is applied to a typical dielectric material there is no long-range transport of charge as in the conductor but only a finite rearrangement of charge in the opposite direction creates a dipole moment which causing dielectric polarization. In all materials atomic polarization arises from small shifting of the electrons in an atom relative to the nucleus. The ionic polarization result from the lattice vibrations or molecular vibrations induce relative displacements of the atoms, the centers of positive and negative charges are also displaced. Dipolar materials, arises from a permanent dipole such as water, can become polarized because the applied electric field orients the molecules.

Eventually, space charge polarization results from a bounded transport of charge carriers till they are cut off at a potential barrier, perhaps phase boundary or a grain boundary. A singular ion or atom in a dielectric is not submitted directly to an electric field but to a local field in certain conditions it has a quite different value, the local field resulting from the lattice polarization is inclined to stabilize the polarization further (feedback mechanism process).

This indicates the possibility of “spontaneous polarization” i.e., dielectric material which characterized by electric polarization in the absence of an external electric field. “Ferroelectrics” constitute a significant category of spontaneously polarized materials [77].

A number of polymers and ceramics are utilized as insulators and/or in capacitors. Numerous of the ceramics, including porcelain, glass, mica, and steatite, possess dielectric constants in the range from (6 -10) moreover showed a high degree of dimensional stability and mechanical strength. Practical utilization involve electrical insulation, powerline, light receptacles and switch bases.

The Titanium dioxide (TiO_2) and titanate ceramics, like barium titanate (BaTiO_3), can be produce to have highly dielectric constants, which advance them to benefit for some capacitor utilizations. Most polymers have dielectric constant less than for ceramics, since the ceramics may show maximal dipole moments: ϵ_r magnitude for polymers usually ranging from 2 to 5. These materials are ordinarily utilized for insulation of cables ,wires, generators, motors , capacitors and so on [76].

2.24 Ferroelectricity

Class of dielectric materials known as ferroelectrics showed spontaneous polarization despite the absence of an external electric field. They are the dielectric parallel of ferromagnetic substances, which may exhibit permanent magnetic demeanor. Ferroelectric substances have permanent electric dipoles, the principle of which is obvious for barium titanate, one of the generally ferroelectrics.

The spontaneous polarization is a result of the locating of the Ba^{2+} , Ti^{4+} , and O^{2-} ions in the unit cell, as showed in Figure (2.15). The Ba^{2+} ions are situated in the corners of the unit cell, which is of tetragonal symmetry. The dipole moment creates from the relative displacements of the O^{2-} and Ti^{4+} ions from their symmetrical positions as shown in the side view of the unit cell. The O^{2-} ions are located near, but slightly below, the centers of each of the six faces, whereas the Ti^{4+} ion is displaced upward from the unit cell center.

Thus, a permanent ionic dipole moment is associated with each unit cell (Figure 2.15*b*). Nevertheless, ferroelectric demeanor is stopped when BaTiO_3 is heated higher than its ferroelectric Curie temperature (120°C), the crystal structure becomes cubic, and all ions supposedly symmetric situations in the cubic structure.

Ferroelectrics possess highly dielectric constants at low frequencies; for example, approximate value of dielectric constantate for BaTiO_3 at room temperature about 5000. Consequently, now it is possible to fabricate capacitors have much smaller size from the ferroelectric materials[76].

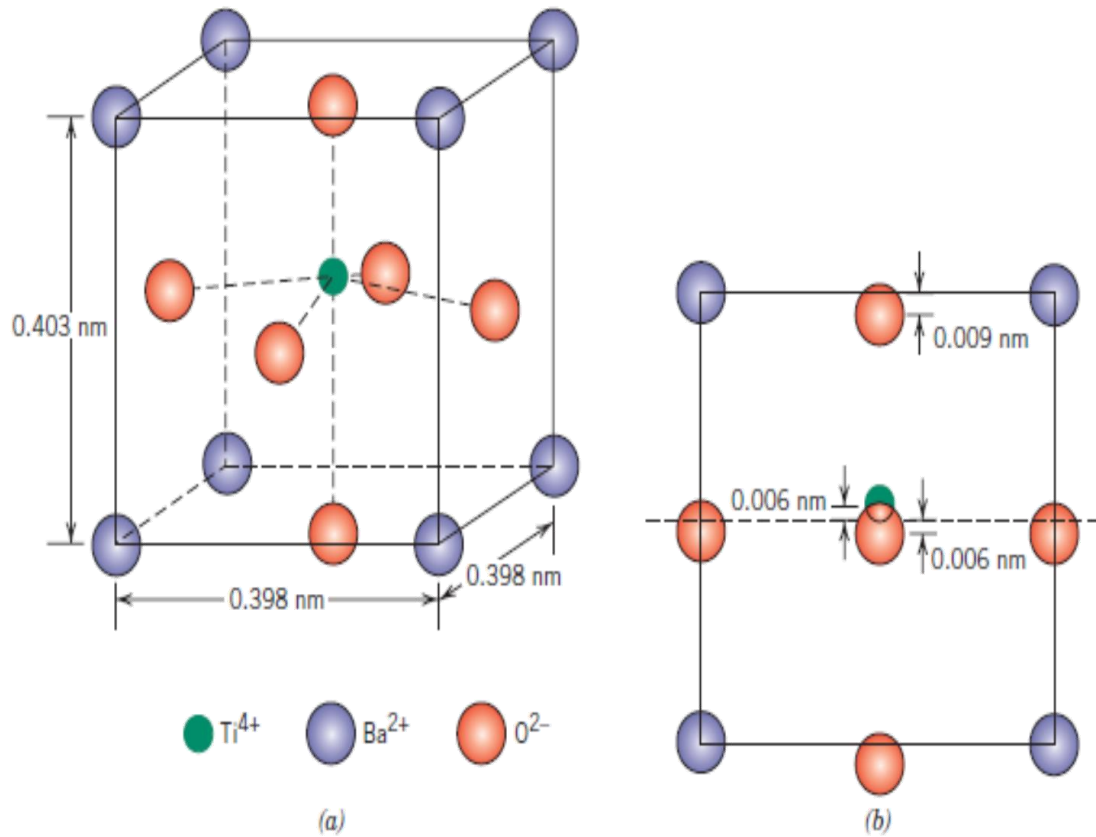


Figure (2.15) a barium titanate (BaTiO_3) unit cell (a) in an isometric projection, and (b) looking at one face, which shows the displacements of Ti^{4+} and O^{2-} ions from the center of the face [76].

Chapter Three

Experimental work

3.1 Introduction

This chapter includes practical steps for the sample preparation with general formula $\text{BaFe}_{12}\text{O}_{19}$ (barium hexaferrite) using sol - gel method, and synthesis appropriate forms for tests. Barium titanate (BaTiO_3) was prepared using a conventional ceramic method, then making composite material samples using epoxy- resin. This chapter also includes devices, which were used for testing the prepared sample.

3.2 Selection of raw materials for preparing barium hexaferrite

Table (3-1) shows the raw materials that had been used in this work to prepare the samples using the sol - gel method and its purity as shown in the labels of the cans of materials.

Table (3-1): The chemical materials and their properties

Compounds	Chemical formula	% Purity	Company
Iron (III) nitrate	$\text{Fe}(\text{NO}_3)_3 \cdot 9\text{H}_2\text{O}$	98	Qualikems
Barium nitrate	$\text{Ba}(\text{NO}_3)_2$	99	ZORKA
Ammonia solution	NH_3	30	Lobachmie
Citric Acid	$\text{C}_6\text{H}_8\text{O}_7 \cdot \text{H}_2\text{O}$	99	Lobachmie

3.3.1 Calculating Molecular weight of materials

The molecular weight of the raw materials used, was calculated from the atomic weight of the base elements as given below:

$$\text{Fe (NO}_3)_3 \cdot 9\text{H}_2\text{O} = 55.84 + 14.01 \times 3 + 15.99 \times 18 + 18 \times 1.008 = 403.834 \text{ g/mol}$$

$$\text{Ba (NO}_3)_2 = 137.3 + 14.01 \times 2 + 15.99 \times 6 = 261.26 \text{ g/mol}$$

$$\text{C}_6\text{H}_8\text{O}_7 \cdot \text{H}_2\text{O} = 6 \times 12.01 + 10 \times 1.008 + 8 \times 15.99 = 210.16 \text{ g/mol}$$

3.3.2 Method of preparation of barium ferrite

Table (3-2) below showing the molar ratios and weight compounds used for the preparation of barium ferrite:

No-	Molar ratio [Fe/Ba]	Iron (III) nitrate (Fe (NO ₃) ₃ · 9H ₂ O)	Barium nitrate (Ba(NO ₃) ₂)	Citric Acid (C ₆ H ₈ O ₇ · H ₂ O)
1	12:1	24.23 g	1.3063 g	12.6 g
2	12:3	24.23 g	3.9189 g	12.6 g
3	12:6	24.23 g	7.8378	12.6 g

1-The equation below used for calculating the samples weight of the compound composition:

$$[M] = \frac{m}{m.wt} \times \frac{1000}{v \text{ ml}} \dots\dots\dots (3-1)$$

Where [M] - Molar concentration, m- weight (g), (m .wt) - Molecular Weight, V- Volume.

2- The molar ratio of Citric Acid with iron nitrate fixed with ratio 1:1.

3-Measuring the stoichiometric amounts of Iron (III) nitrate,

Barium nitrate and citric acid were dissolved in 200ml of distilled water in a glass beaker ,to obtain aqueous solution which homogenized by continuous stirring by magnetic hot plate-stirrers , aqueous solution containing citric acid used to chelate ions Ba^{+2} and Fe^{+3} in the solution [78] .

4-Then liquid ammonia was slowly added to neutralize solution until PH=7 with continuous stirring.

5-By heating the neutralized solution at 100 °C on a hot plate with continuous stirring, the water evaporated from the solution which became gluey.

6-While continuing heating bubbles will consist in the gel which rid as gasses and steam sluggish from the solution.

7-After the gel dries completely it will turn to incoherently powder by self-combustion.

8-The Powder is calcined in air atmosphere at different temperatures: 700°C, 800°C, 900°C, 1000°C, 1100°C and 1200°C for three hours and left in the furnace to reach room temperature after turning off the furnace for each calcination process.

Figure (3.1) shows the sol-gel auto combustion synthesis flow diagram that was used for preparing Nano powders ferrite.

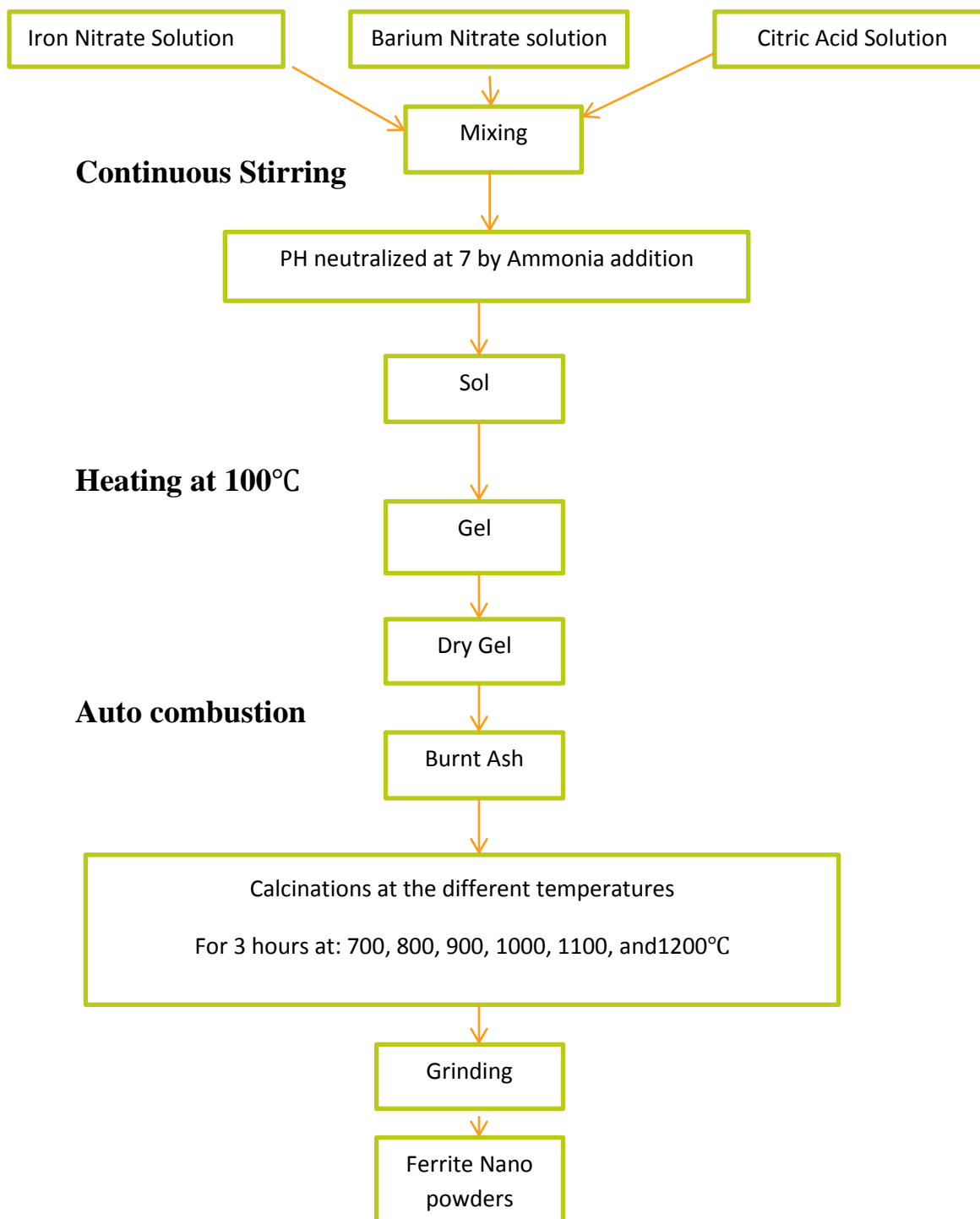


Figure (3.1): auto-combustion Flow diagram for preparing Nano powders barium ferrite.

3.3.3 Preparation of samples (m-type barium hexaferrite)

The five samples were obtained from powder of barium hexaferrite will gotten after calcination the powder at different temperatures. weighed 5 g of each sample to pressing within the cylinder mold under the pressure 4500 pounds per 1.6 inch to form the disks shape which sintered later in the higher temperature(the powder was acquired at 700°C and then sintered at 800°C for 3hours and so on for the other samples) as follows:

Table (3-3) describes the sintering process for the samples

NO-	Calcination Temperature(°C)/3h (Powder)	Sintering Temperature(°C)/3h (Disk)
1	700	800
2	800	900
3	900	1000
4	1000	1100
5	1100	1200

After sintering the samples which obtained from weighing 5g of barium ferrite it used for LCR- meter test after adjusted the thickness to 2.8 mm for all the samples as shown in the figure (3.2a). In the same procedure, weight 15g of powders giving discs with thickness ranges (8-8.4 mm), then cutting and modified to match waveguide dimensions(22.86× 10.16)mm with the thickness 8mm for all the samples and equated the thickness to 8mm which used to VNA tests as shown in the figure (3.2b).

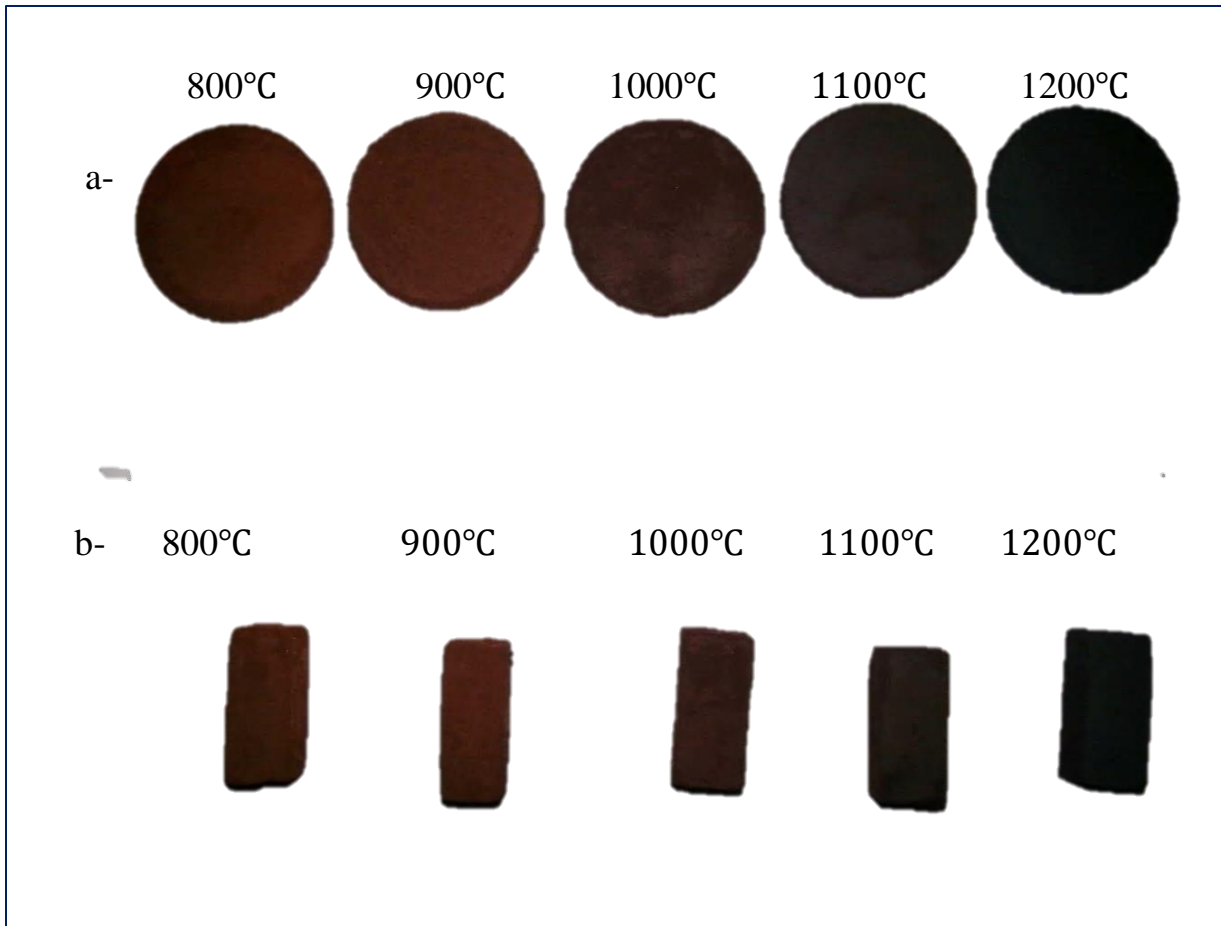


Figure (3.2) Shows samples that have been prepared for the purpose of:

a- For the LCR-meter tests

b- For VNA tests

3.4 Preparation of barium titanate (BaTiO_3) using the Conventional Ceramic Method

Barium titanate was prepared by a solid-state reaction method that involves a ball milling of BaCO_3 or BaO and TiO_2 which requires calcination of the mixture at high temperature [79-80].

Table (3-4): The raw materials which used to prepare (BaTiO₃) in Conventional ceramic method.

Compounds	Chemical formula	Molecular Weight	% Purity	Company
Barium carbonate	BaCO ₃	197.28 g/mol	99	Panreac Assay
Titanium dioxide	TiO ₂	79.85 g/mol	97	GCC

BaTiO₃ was prepared by the reaction between BaCO₃ and TiO₂ by mixing 15.96 g from TiO₂ with 39.456g from BaCO₃ (which means that the molar ratio of the two compounds 0.2:0.2) was done by milling the mixture using the conventional ceramic a mortar in three stages:

Table (3-5): preparation stages of BaTiO₃

Number of -stage	Milling time	Calcined Temperature(°C)
1-	15h	1000
2-	5h	1100
3-	5h	1200

Finally, we get barium titanate (BaTiO₃) and identified by x-ray examinations then grind to prevent conglomerates.

3.5 Preparation of Composite material

1-The main method of preparation of samples begin with the weight of the matrix (epoxy- resin) with a mix ratio (3:1) i.e. 7.5: 2.5g.

2-After mixing process of basic material epoxy and reinforcement material (BaTiO_3 or/and $\text{BaFe}_{12}\text{O}_{19}$) particles which placed in class peaker to dispersion material using ultrasonic for half an hour, reduce the viscosity of the basic material for facilitating the distribution of nanoparticles.

3-After the addition of hardener then mixed using magnetic stirrers with continuous stirring obtain viscous liquid with homogeneous particle.

4- Casting of the liquid mixture in special templates which prepared to fit the waveguide dimensions, then left to dry after 24 hours. It has been added 1g from (BaTiO_3 or/and $\text{BaFe}_{12}\text{O}_{19}$) powders for every 10g epoxy-resin (EUXIT 50) according to the table (3-6) below:

Table (3-6) Show Epoxy- Resin with ratio of (barium hexaferrite/ barium titanate)

No-specimen	Barium hexaferrite(g)	Barium titanate(g)	Epoxy-Resin(g)	Thickness(mm)	Denotation
1-	—	—	10	4.46	A_{00}
2-	1.00	—	10	4.46	$A_{4:0}$
3-	0.75	0.25	10	4.46	$A_{3:1}$
4-	0.50	0.50	10	4.46	$A_{2:2}$
5-	0.25	0.75	10	4.46	$A_{1:3}$
6-	—	1.00	10	4.46	$A_{0:4}$

Barium hexaferrite which used to prepare composite material in this experiment calcined at 1200°C for 3h. Figure (3.3) below shows the prepared composite samples for VNA tests:



Figure (3.3) prepared composite material for study microwave characteristic tests.

3.6 Instruments

A set of devices were used to testing the physical characteristics of the samples:

3.6.1 Network analyzers

A network analyzer is one of the most important tools for analyzing analog circuits. By measuring the amplitudes and phases of transmission and reflection coefficients of an analog circuit, Network analyzers are

Widely used to measure the four elements in a scattering matrix: S_{11} , S_{12} , S_{21} , and S_{22} . The vector network analyzer device is illustrated in figure (3.4) type of (E5071C - 300kHz-20 GHz) .

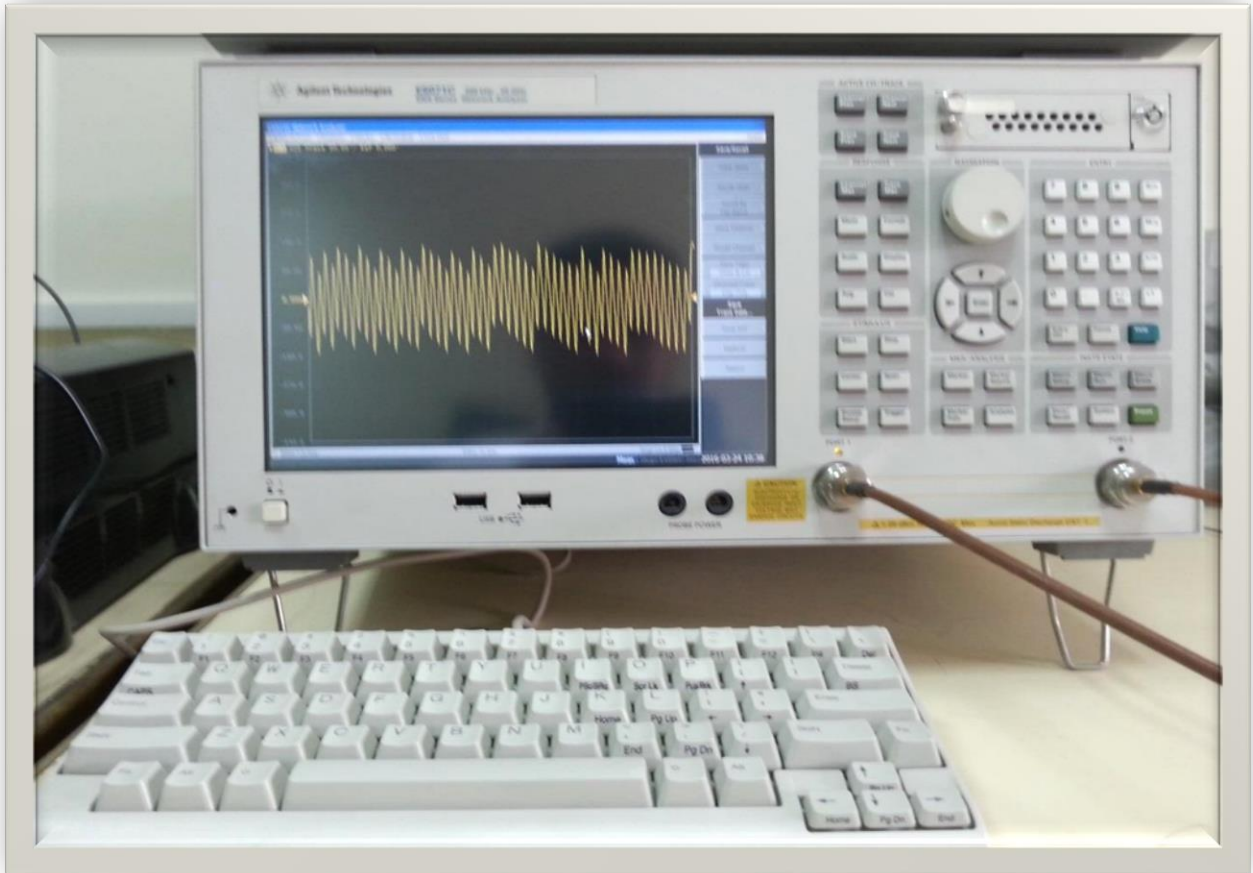
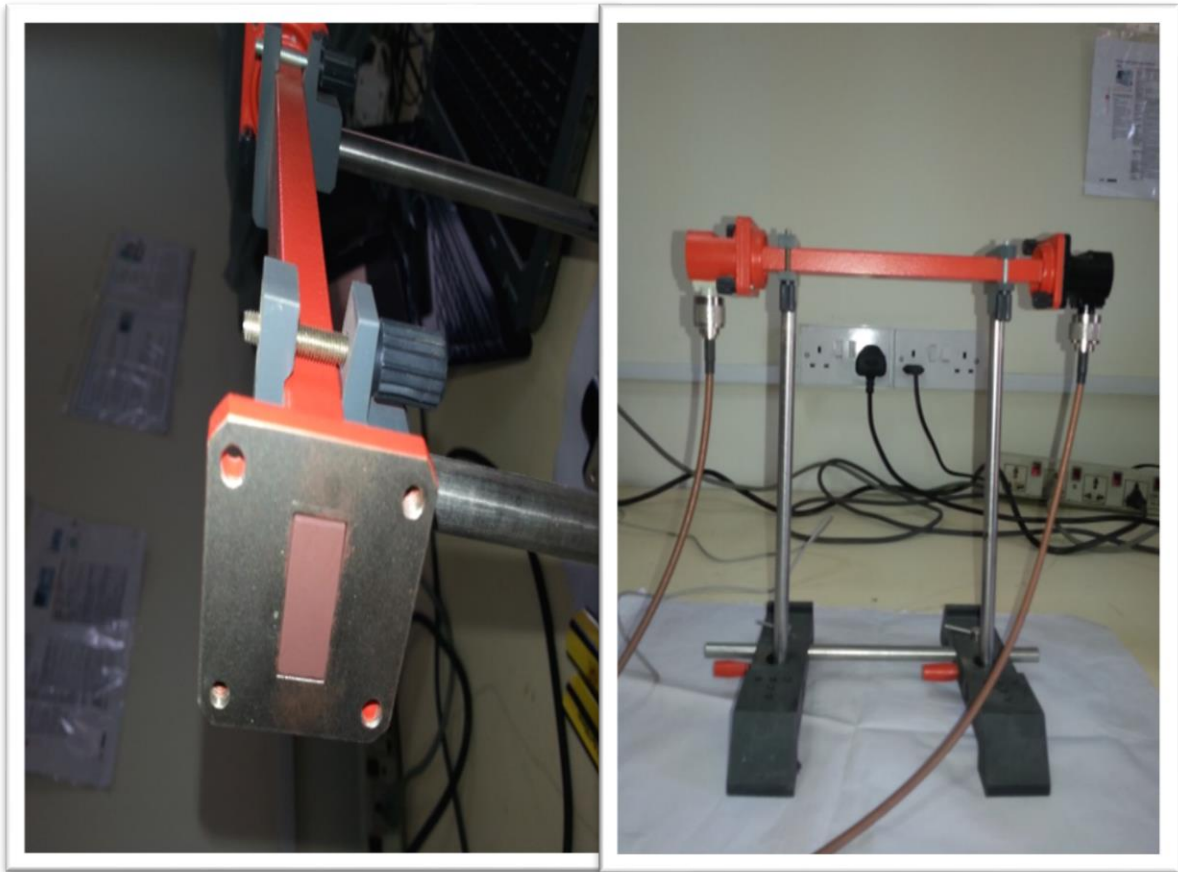


Figure (3.4) vector network analyzer device

In a transmission/reflection method, the sample under test is inserted into a segment of transmission line, such as waveguide, as shown in figure (3.5a, b). From the scattering parameters were calculated the permittivity and permeability for the sample by using explicit formulas called Nicolson–Ross–Weir (NRW) algorithm.

The samples were measured with the Vector Network Analyzer between 7.5 and 12.5 GHz. The attenuation coefficient or reflection loss in (dB) unit is calculated from the equation below [43]:

$$\text{Attenuation Coefficient} = -20 \text{ Log}|s_{11}| \dots\dots\dots (3-2)$$



(a)

(b)

Figure (3.5), (a) -sample inserted into a segment of the waveguide

(b) - Coaxial probe of (VNA) connected to the ends of the waveguide.

And the absorption of the EM waves was calculated by the following equation [81]:

$$(\text{Absorption}) = -10 \log [|S_{21}|^2 / (1 - |S_{11}|^2)]. \dots\dots\dots (3-3)$$

an absorption of 20 dB indicates that 99% of the introduced EM waves is absorbed.

3.6.2 Nicholson-Ross-Weir (NRW)

This method provides a direct calculation of both the permittivity and permeability from the s-parameters. It is the most commonly used method for performing such conversion.

Measurement of reflection coefficient and transmission coefficient requires all four (S_{11} , S_{21} , S_{12} , S_{22}) or a pair (S_{11} , S_{21}) of s parameters of the material under test to be measured. NRW method is divergent at integral multiples one-half wavelength in the sample.

This is due to the fact that at a point corresponding to the one-half wavelength the s-parameter (S_{11}) gets very small. For a small s-parameter (S_{11}) value the uncertainty in the measurement of the phase of S_{11} on the VNA is very large.

Therefore the uncertainty caused the divergence at these frequencies. These divergences can be avoided by reducing the sample length, but it is difficult to determine the appropriate sample length when its ϵ and μ are unknown.

Advantages of NRW method

- Fast, non-iterative.
- Applicable to waveguides and coaxial line.

Disadvantages of NRW method

- Divergence at frequencies corresponding to multiples of one-half wavelength.

- Short sample should be used.
- Not suitable for low loss materials.

Nicholson-Ross-Weir Conversion Process

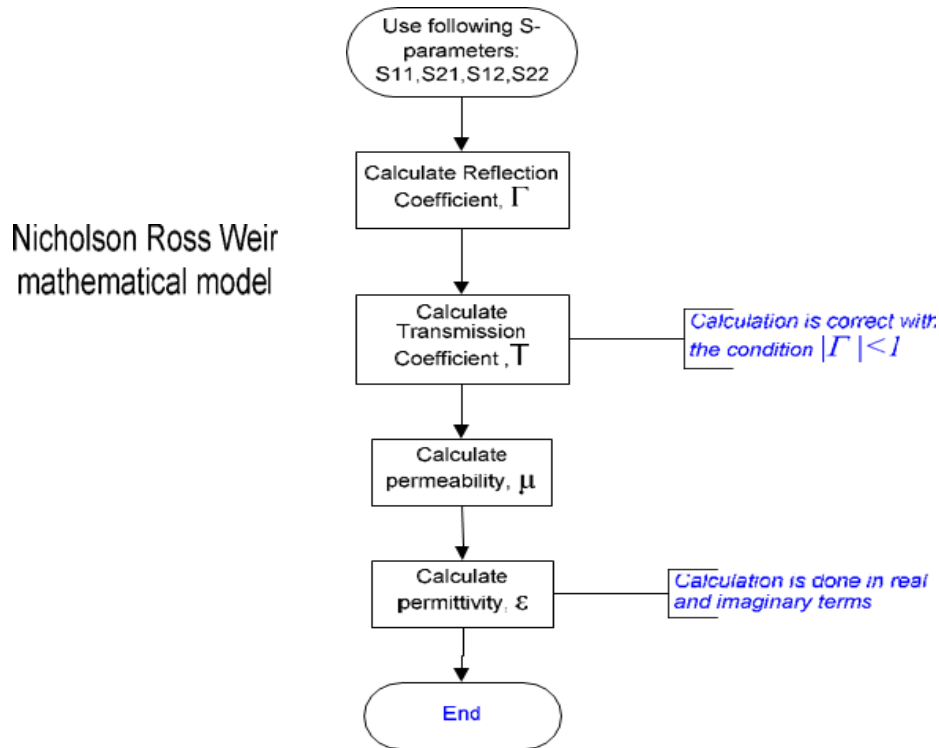


Figure (3.6) the process for the NRW method.

The procedure proposed by NRW method is deduced from the following equations [82]:

$$S_{11} = \frac{\Gamma(1-T^2)}{(1-\Gamma^2 T^2)} \quad \text{and} \quad S_{21} = \frac{T(1-\Gamma^2)}{(1-\Gamma^2 T^2)}$$

These parameters can be obtained directly from the network analyzer.

The reflection coefficient can be deduced as:

$$\Gamma = X \mp \sqrt{X^2 - 1} \dots\dots\dots (3-4)$$

Where $|\Gamma| < 1$ is required for finding the correct root and in terms of s-parameter.

$$X = \frac{S_{11}^2 - S_{21}^2 + 1}{2S_{11}} \dots\dots\dots (3-5)$$

The transmission coefficient can be written as:

$$T = \frac{S_{11} + S_{21} - \Gamma}{1 - (S_{11} + S_{21})\Gamma} \dots\dots\dots (3-6)$$

The permeability is given as:

$$\mu_r = \frac{1 + \Gamma_1}{\Lambda(1 - \Gamma) \sqrt{\frac{1}{\lambda_0^2} - \frac{1}{\lambda_c^2}}} \dots\dots\dots (3-7)$$

Where λ_0 is free space wavelength and λ_c is the cutoff wavelength and

$$\frac{1}{\Lambda^2} = \left(\frac{\epsilon_r * \mu_r}{\lambda_0^2} - \frac{1}{\lambda_c^2} \right) = - \left(\frac{1}{2\pi L} \text{Ln} \left(\frac{1}{T} \right) \right)^2 \dots\dots\dots (3-8)$$

The permittivity can be defined as

$$\epsilon_r = \frac{\lambda_0^2}{\mu_r} \left(\frac{1}{\lambda_c^2} - \left[\frac{1}{2\pi L} \text{Ln} \left(\frac{1}{T} \right) \right]^2 \right) \dots\dots\dots (3-9)$$

3.6.3 X-ray Diffraction Tests

To investigate the crystal structure of the prepared samples after sintering , phase analysis was done by x-ray diffraction (XRD) using Cu-K α radiation, and wavelength $\lambda = 1.54060 \text{ \AA}$; the range of the Braggs angles are taken ($2\theta = 20^\circ - 90^\circ$) for the samples ,with scan speed 8.0000(deg /min), the type of this device is (XRD -6000) and made in Japan by SHIMADZU.

The lattice parameter can be calculated using equation (2-95); which is standard relation to the hexagonal systems, where h , k and l are the indices of

The crystal planes, a and c are the lattice parameters, The interplaner distance (d) measured, and then comparing the resultant x-ray patters with international standerd (ICDD) International Centre for Diffraction Data which is the American Standard for Testing Materials (ASTM).

3.6.4 Measuring the density

The bulk density of the prepared samples has been measured after a process of sintering the samples have been weighted and Measuring the dimensions. The volume (V) is measured by the unit of cm^3 (volume = length * width * height) and the mass (m) is measured by the unit of a gram. The porosity can be calculated using equations below:

$$d_{bulk} = \frac{m}{V} \dots\dots\dots (3-10)$$

$$d_{theo} = \frac{2M}{N_A V} \dots\dots\dots (3-11)$$

$$V = \frac{\sqrt{3}}{2} a^2 c \dots\dots\dots (3-12)$$

$$P(\%) = \left(1 - \frac{d_{bul;}}{d_{theo.}}\right) * 100 \dots\dots\dots (3-13)$$

Where (d_{bulk}) is the Bulk density, (d_{Theo}) is the Theoretical density, (P) is the porosity, (M) is the molecular mass, (N_A) is the Avogadro's number and (a, c) is the lattice constant [83-84].

3.6.5 Scanning electron microscope (SEM) Test

The scanning electron microscope (SEM) is a type of electron microscope that is used to produce high resolution three dimensional images of a specimen surface. This technique is useful for looking at particle or grain size,

Crystal morphology, magnetic domains, porosity surface defects. The basic components of the SEM consist of the lens system, the electron gun, the electron collector, the visual and photo recording cathode ray tubes (CRTs), and the associated electronics shown in figure (3-7).

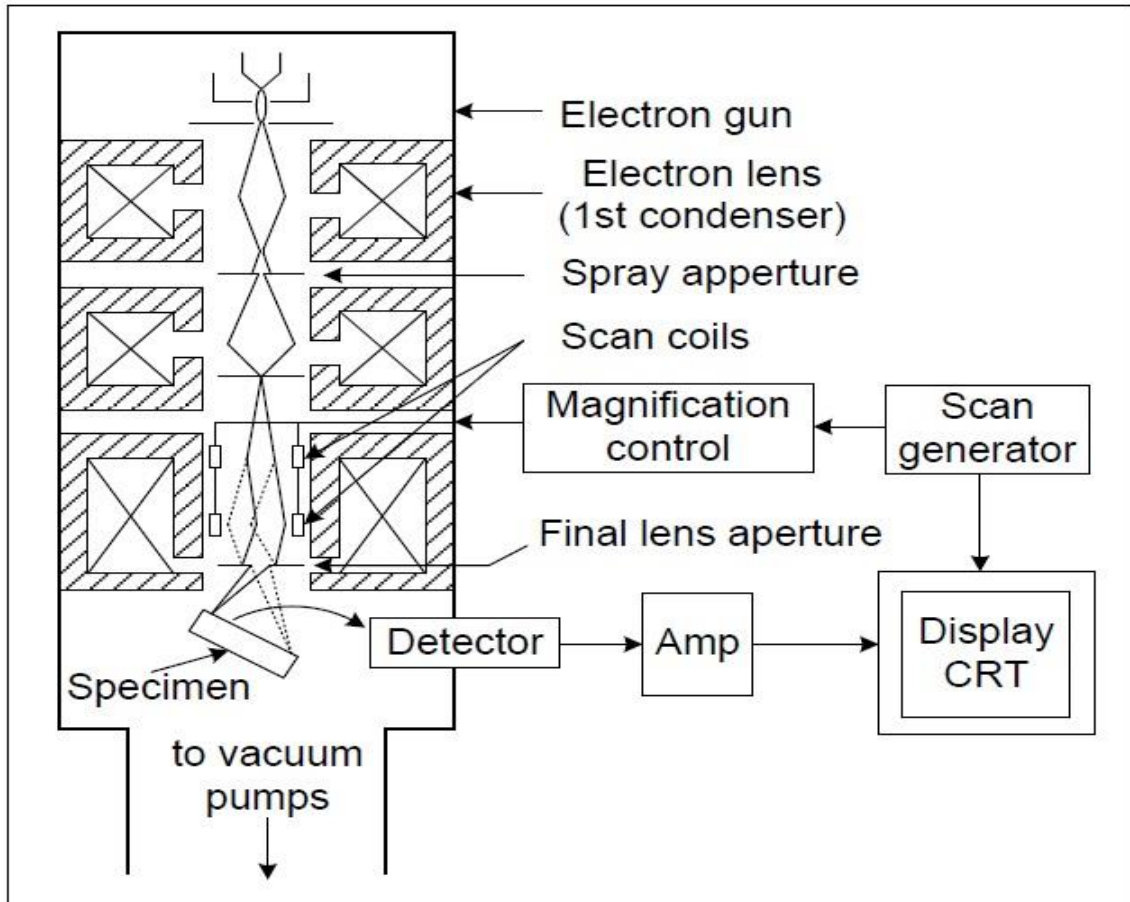


Figure (3.7): Schematic of the basic components of the SEM

In the SEM, the area to be examined or the micro volume to be analyzed is irradiated with a finely focused electron beam which may be swept in a raster across the surface of the specimen to form images or may be static to obtain an analysis at one position. The types of signals produced from the interaction of the electron beam with the sample include secondary electrons, backscattered electrons, characteristic X-rays, and other photons of various energies. These signals are obtained from specific emission volumes within

The sample and used to examine many characteristics of the sample (surface topography, crystallography, composition, etc.) [43].The microstructure of the samples was observed using a scanning electron microscope (SEM).inspect S50.FEI .Netherlands' origin.

3.6.6 LCR -meter

The dielectric constant which is measured by an LCR meter connected to a computer that the sample which puts between the poles and makes sure that the poles touch sample surface, LCR system is used for the purpose of measuring the capacity of the disc samples at different frequencies. Dielectric constant data have recorded on computer screen via mathematic formulas. The model of LCR-8105G, manufactured by GW Instek, its range of frequency is (5Hz-5MHz), as shown in the figure (3.8).



Figure (3.8) LCR meter used in electrical measurement

The capacitance of the pellets was determined from The LCR meter and then dielectric constant was calculated using the formula [85]:

$$\varepsilon' = C/C_0 \quad \dots\dots\dots (3-14)$$

C Is the capacitance of the material and C_0 is the capacitance of free space,

$$\text{And } C_0 = \varepsilon_0 A/d \quad \dots\dots\dots (3-15)$$

Where ε_0 is the permittivity of the free space and has a value of $(8.854 \times 10^{-12} \text{ F.m}^{-1})$, the equation (3-14) becomes:

$$\varepsilon' = Cd/\varepsilon_0 A \quad \dots\dots\dots (3-16)$$

Where d is the thickness of the pellet in meters, A is the cross-sectional area of the flat surface of the pellet.

And the dissipation factor (D) (loss tangent $\tan \delta$) determined from The LCR meter, loss tangent can be expressed as:

$$\tan \delta = \frac{\varepsilon''}{\varepsilon'} \quad \dots\dots\dots (3-17)$$

Where, ε' And ε'' Are real and imaginary part of a relative permittivity,

the AC conductivity was calculated from the values of dielectric constant and dielectric loss factor using the relation:

$$\sigma_{A.C} = \omega \varepsilon_0 \varepsilon'' \quad \dots\dots\dots (3-18)$$

Where σ_{AC} is the AC conductivity, ω is the angular frequency.

Chapter Four

Results

and

Discussion

4.1 Introduction

This chapter includes practical results that were obtained from the measurements and tests performed on prepared samples. The structural test which includes X-ray diffraction testing, scanning electron microscopy (SEM) and measuring the density for samples, the dielectric constant were studied at low frequency using the LCR – meter, the real part (ϵ_r') of dielectric constant it is represented electrical energy stored in the material, the imaginary part (ϵ_r'') represents the energy dissipated, and the ratio of the imaginary part to the real part represent the 'lossiness' of the material. Microwave absorbance measurements, including attenuation coefficient and absorption for all samples using the (VNA)-system, then the permittivity and permeability were calculated by explicit formulas called Nicolson–Ross–Weir (NRW) algorithm.

4.2 X-Ray Diffraction Results

sol-gel combustion process was used to synthesize homogeneous and ultrafine ferrites with narrow size distribution at a relatively low calcination temperature, to study influences of calcination temperature and molar ratio to the phase composition, morphology for obtained powders, the combustion precursor was calcined for 3h at 700°C, 800°C, 900°C, 1000°C, 1100°C and 1200°C with the fixed molar ratio citric acid /nitrates (1:1) and Fe/Ba (12:1), and for the molar ratio Fe/Ba (12:3), (12:6) were calcined at 1200°C, then comparing the resultant x-ray patterns with international standard (ICDD) International Centre for Diffraction Data which is the American Standard for Testing Materials (ASTM).

Figure (4.1) illustrates the XRD patterns obtained after combustion precursor in 100°C on hot plate, the peaks of combustion precursor matched well with

Barium Carbonate (BaCO_3) and maghemite ($\gamma\text{-Fe}_2\text{O}_3$), which suggests that, unlike other spinel ferrites.

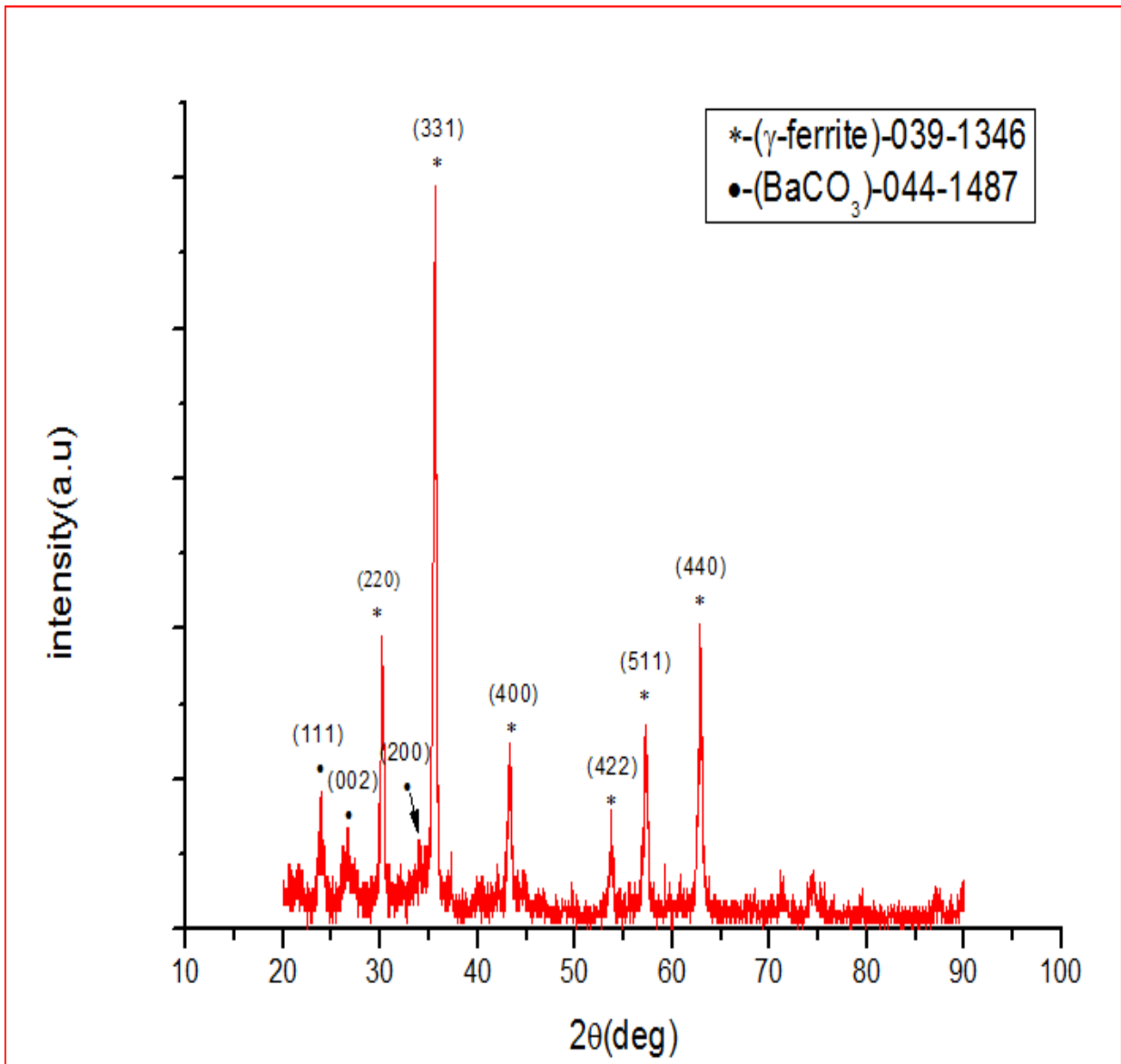


Figure (4.1) shows XRD patterns after auto-combustion on a hot plate at 100°C and before calcination precursor.

The results which acquired from XRD tests figure (4.1) inferred that difficultly of preparing the hexagonal phase directly by auto-combustion procedure. For the sample calcined at 700°C for 3h,

Figure (4.2) shows the presence of intermediate phase (BaFe_2O_4) and the existence of ($\gamma\text{-Fe}_2\text{O}_3$) with barium hexaferrite ($\text{BaFe}_{12}\text{O}_{19}$) formation.

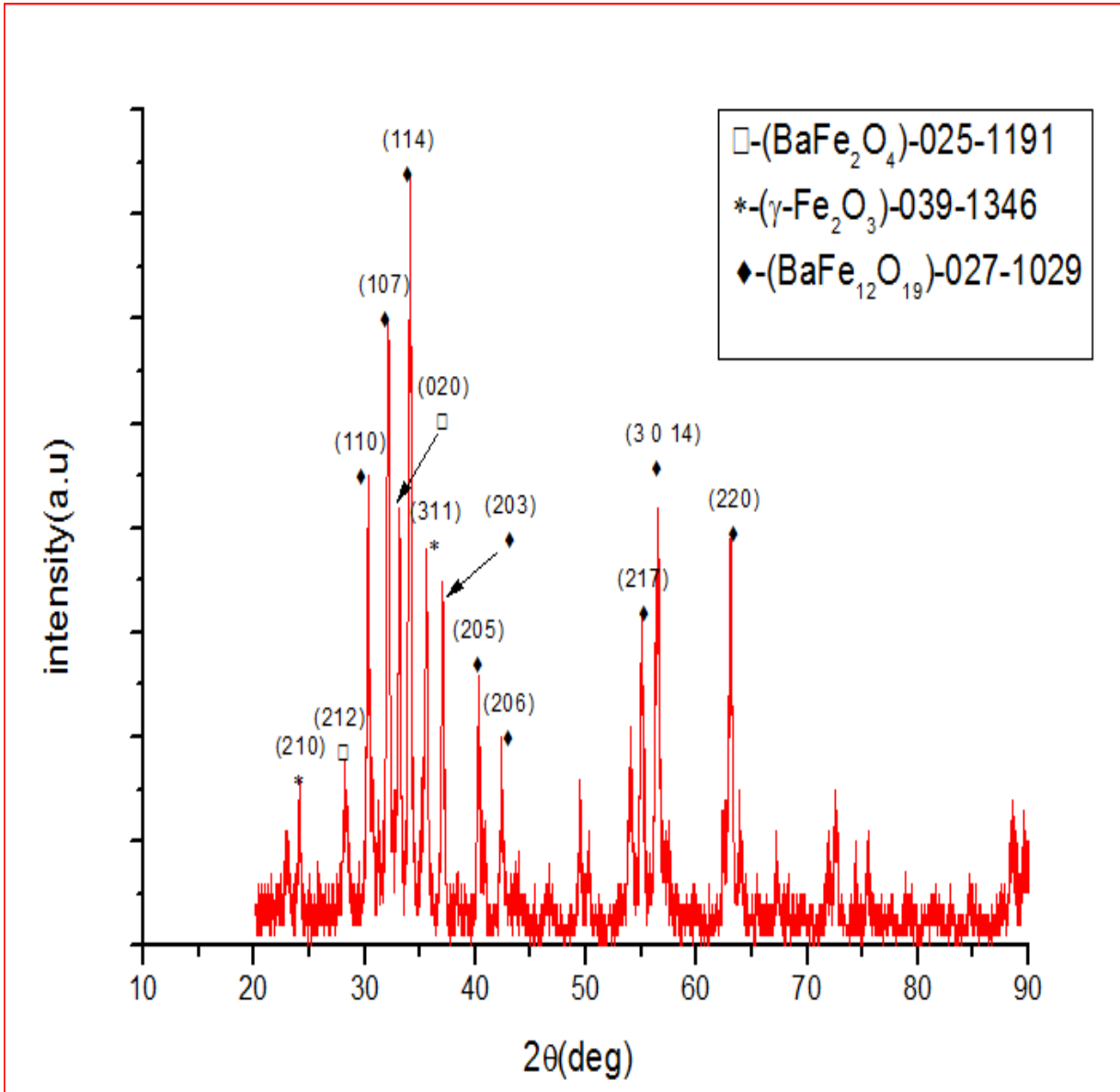


Figure (4.2) XRD patterns of the powders calcined at 700°C.

XRD also shows that single objective ($\text{BaFe}_{12}\text{O}_{19}$) hexagonal structure was detected for powders calcined at 800°C, 900°C, 1000°C and 1100°C for 3h

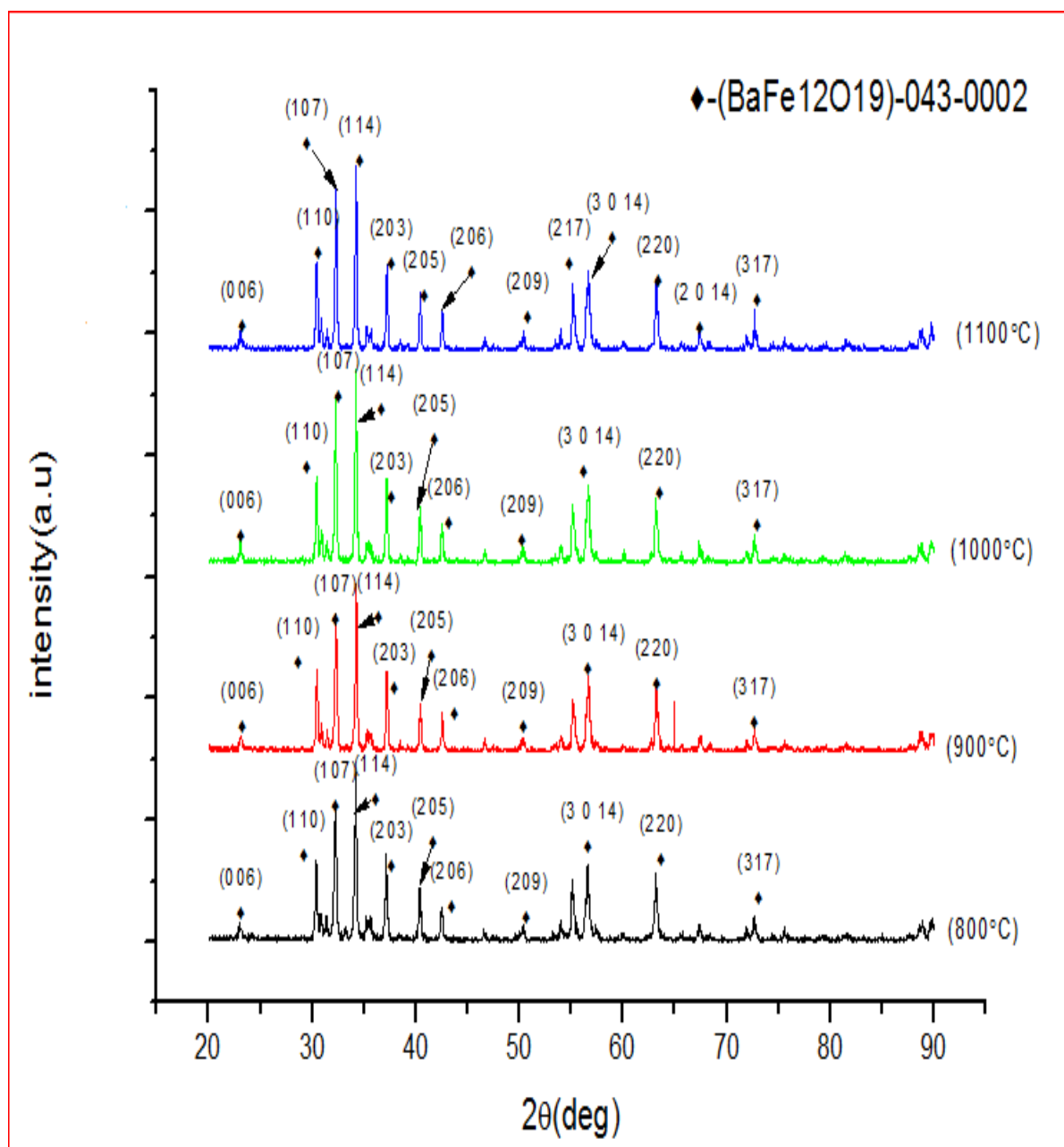


Figure (4.3) XRD patterns of the powders calcined at different temperatures.

The previous XRD pattern shows that began to transform into $\text{BaFe}_{12}\text{O}_{19}$ (hexagonal phase) when the calcination temperature at 800°C or

Greater than, it can be easily found that with increasing calcination temperature the peak width becomes narrower, indicating that the mean crystalline size of synthesized ferrites gradually increased [86].

When the calcination temperature was 1200°C two phases of the hexagonal Barium Ferrite observed, which matched fully compatible with $(\text{BaFe}_{12}\text{O}_{19})$ JCPDS 039-1433 and $(\text{Ba}_3\text{Fe}_{32}\text{O}_{51})$ JCPDS 041-0846, as evidenced in the figure (4.4):

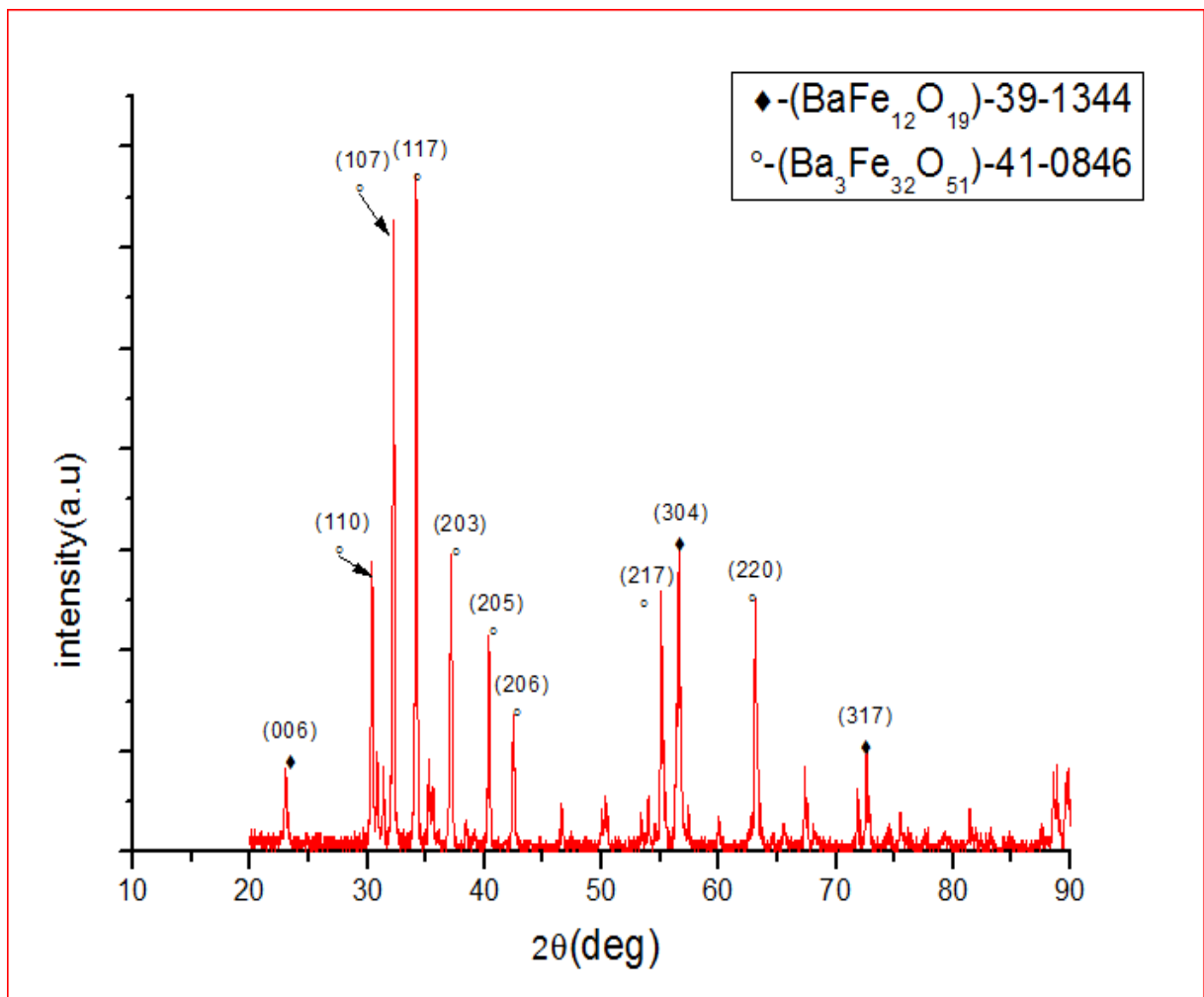


Figure (4.4) XRD patterns of the powders calcined at 1200°C.

Otherwise when a molar ratio of Fe/Ba was (12:3), a secondary phase barium mono-ferrite (BaFe_2O_4) was observed in addition to the hexagonal phase $\text{BaFe}_{12}\text{O}_{19}$ as evidenced in the figure (4.5):

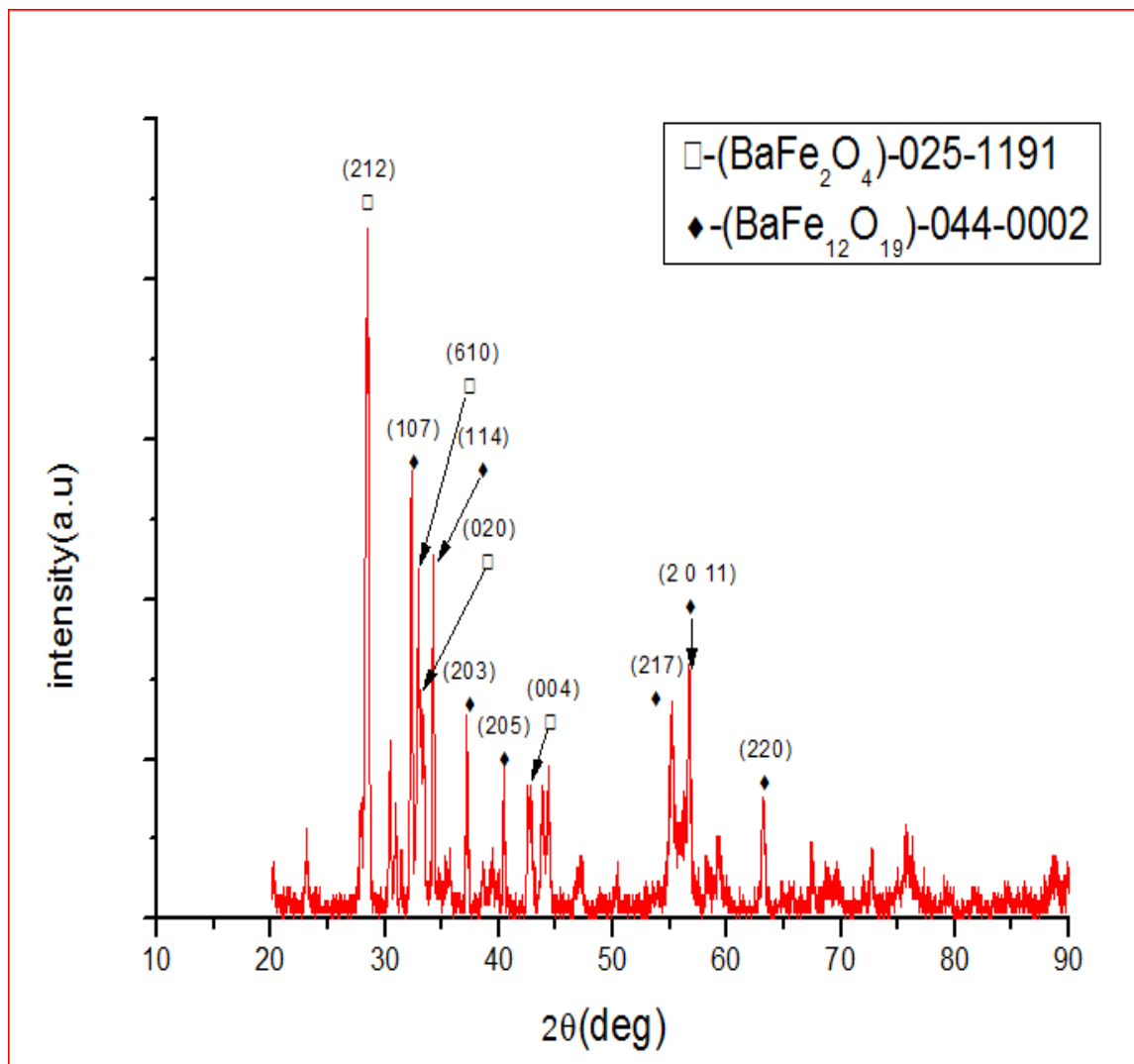


Figure (4.5) XRD patterns of the powders calcined at 1200°C for 3h with molar ratio to Fe/Ba (12:3).

By increased the molar ratio to (Fe/Ba) 12:6, Hexagonal phase disappears completely and barium mono-ferrite BaFe_2O_4 (antiferromagnetic [86]) was formed, evidenced in the figure (4.6):

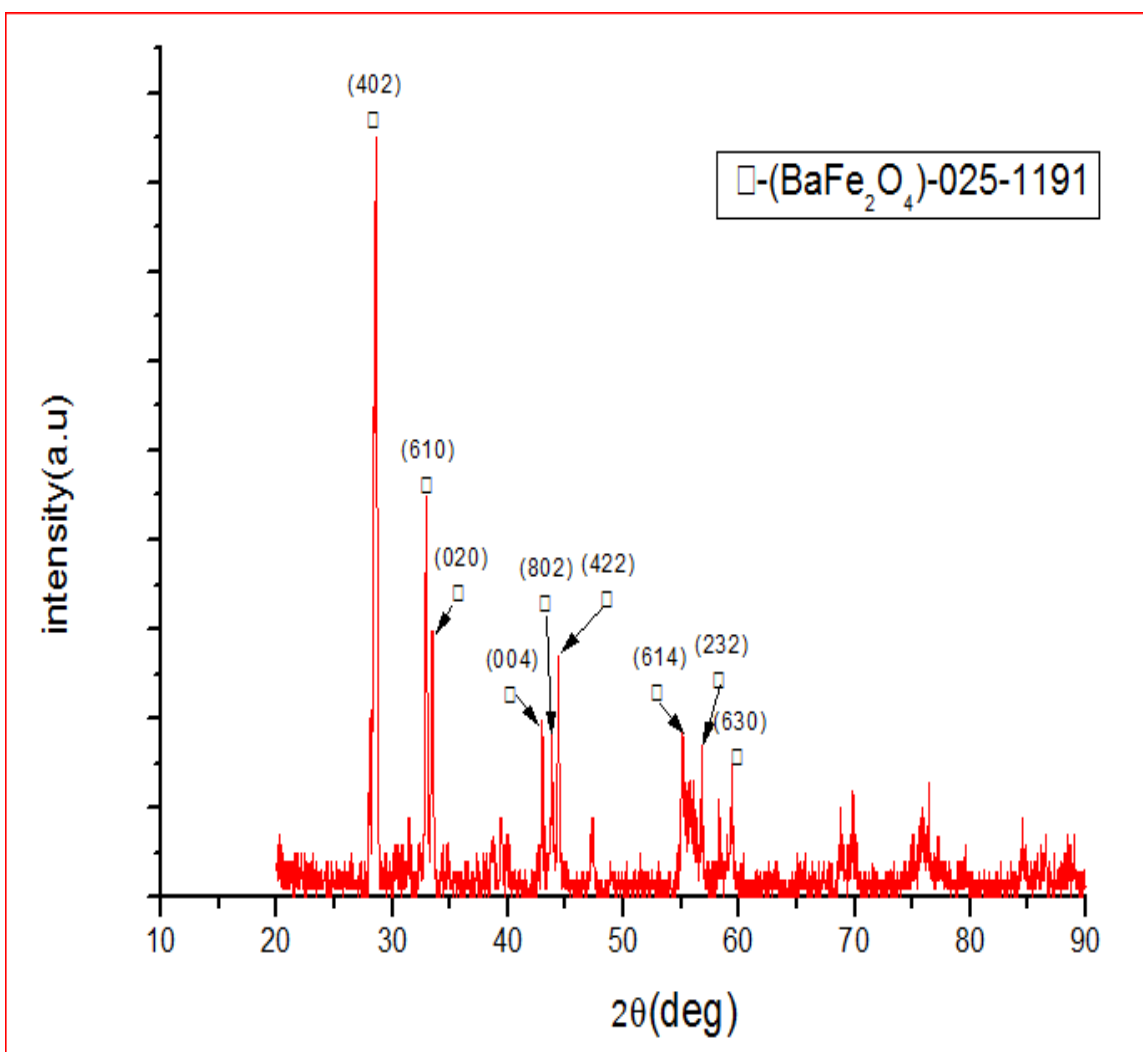


Figure (4.6) XRD patterns of the powders calcined at 1200°C with molar ratio to Fe/Ba (12:6).

The previous results summarized in the table (4-1):

The table (4-1) shows the phase composition of the obtained powders after auto-combustion, after calcined at different temperatures and different molar proportion.

Table (4-1) phase composition of the studied samples.

No-	Molar Ratio (Fe/Ba)	Phase composition						
		Auto-Combustion	700°C/3h	800°C/3h	900°C/3h	1000°C/3h	1100°C/3h	1200°C/3h
1	12:1	γ -Fe ₂ O ₃ BaCO ₃	γ -Fe ₂ O ₃ BaFe ₂ O ₄ Barium monoferrite BaFe ₁₂ O ₁₉ Barium hexaferrite	BaFe ₁₂ O ₁₉ Barium hexaferrite Ba ₃ Fe ₃₂ O ₅₁ Barium hexaferrite				
2	12:3	-	-	-	-	-	-	BaFe ₁₂ O ₁₉ hexaferrite BaFe ₂ O ₄ Barium monoferrite
3	12:6	-	-	-	-	-	-	BaFe ₂ O ₄ Barium monoferrite

Where the table (4.2) shows the crystal systems, lattice parameters and average crystalline size which resulted from XRD tests at different temperature comparisons to JCPDS- cards for compounds.

Table (4-2) lattice parameters for XRD patterns of the powders obtained from auto-composition procedure and calcined at different temperatures (700°C, 800°C, 900°C, 1000°C, 1100°C and 1200°C) comparison with (ICDD).

	Compound	ICDD calculated parameters					XRD Tests			
		JCPDS-card NO-	System	a (Å)	b (Å)	c (Å)	a (Å)	b (Å)	c (Å)	Average crystalline size (nm)
Auto-combustion	γ -Fe ₂ O ₃	039-1346	Cubic	8.35	8.35	8.35	8.36	8.36	8.36	23.81
	BaCO ₃	044-1487	Orthorhombic	5.31	8.90	6.43	5.26	8.9	6.51	
700°C	γ -Fe ₂ O ₃	039-1346	Cubic	8.35	8.35	8.35	8.31	8.31	8.31	31.85
	BaFe ₂ O ₄	025-1191	Orthorhombic	8.44	19.0	5.39	8.5	18.89	5.4	
	BaFe ₁₂ O ₁₉	027-1029	Hexagonal	5.89	5.89	23.19	5.89	5.89	23.26	
800°C	BaFe ₁₂ O ₁₉	027-1029	Hexagonal	5.89	5.89	23.19	5.87	5.87	23.17	32.99
900°C	BaFe ₁₂ O ₁₉	043-0002	Hexagonal	5.89	5.89	23.18	5.86	5.86	23.13	42.66
1000°C	BaFe ₁₂ O ₁₉	043-0002	Hexagonal	5.89	5.89	23.18	5.86	5.86	23.15	47.63
1100°C	BaFe ₁₂ O ₁₉	043-0002	Hexagonal	5.89	5.89	23.18	5.87	5.87	23.15	49.13
1200°C (Fe/Ba=12:1)	BaFe ₁₂ O ₁₉	043-0002	Hexagonal	5.89	5.89	23.18	5.88	5.88	23.3	52.68
	Ba ₃ Fe ₃₂ O ₅₁	041-0846	Hexagonal	5.89	5.89	23.19	5.87	5.87	23.16	
1200°C (Fe/Ba=12:3)	BaFe ₁₂ O ₁₉	043-0002	Hexagonal	5.89	5.89	23.18	5.88	5.88	22.91	29.2
	BaFe ₂ O ₄	025-1191	Orthorhombic	8.44	19.0	5.39	8.46	18.9	5.35	
1200°C (Fe/Ba=12:6)	BaFe ₂ O ₄	025-1191	Orthorhombic	8.44	19.0	5.39	8.41	18.6	5.35	31.16

By using equation (2-94) (Debye-Scherrer formula), the average crystalline size was calculated which showed an increasing in the crystalline size with increasing the calcination temperature, due to the diffusion of the small particles through the larger particles.

This increasing in the crystallite size mentioned by decreasing of (FWHM) of the XRD diffraction pattern. In the very small crystallites; there are not enough planes to produce complete destructive interference, so a broadened peak is observed [87].

4.3 Scanning Electron Microscopy results

The SEM micrographs of Barium hexaferrite particles for samples after formation which sintered at different temperature:

800°C, 900°C, 1000°C, 1100°C and 1200°C for 3 hours as showed in figure (3.2), had been prepared by using sol-gel (auto-composition) techniques, with molar ratio (Fe/Ba 12:1), shows the influences of temperature on the size of grains, so the increase of temperature will increases the growth rate of crystals and atomic diffusion, consequently leading to form larger grain size.

Figure (4.7) shows very fine particles of ferrite powder that began to agglomerate at 800°C, no clear crystalline microstructure can be seen in this stage, which is indicate that the sintering temperature at 800°C is not perfectly adequate to crystalline M-type structure.

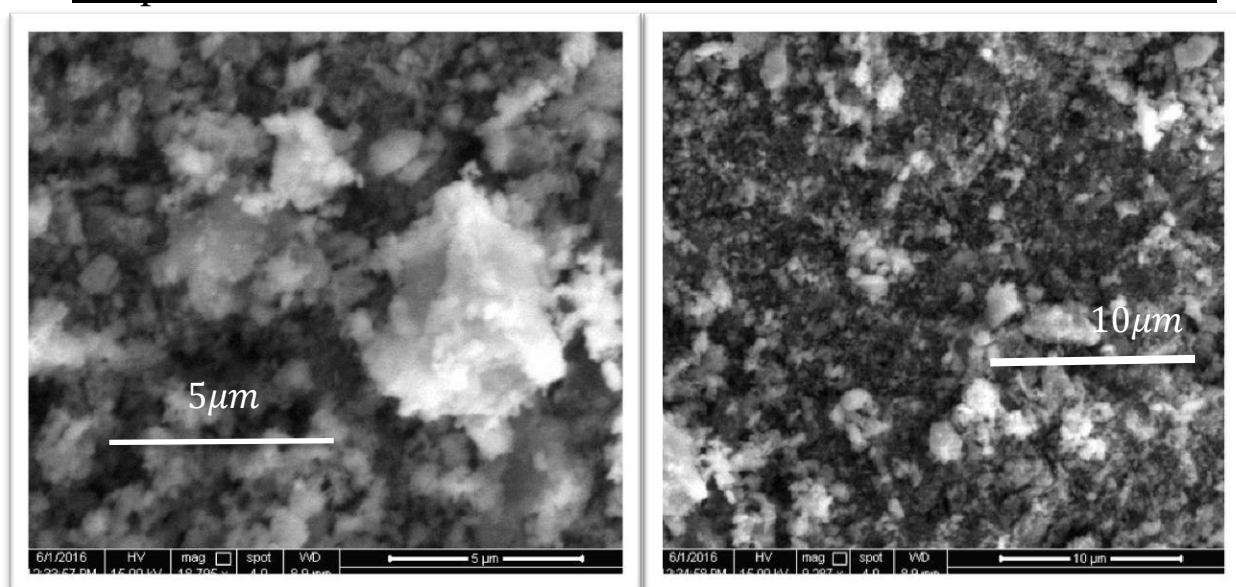


Figure (4.7) SEM micrographs of M-type Barium hexaferrite sintered at 800°C for 3h.

With an increase in sintering temperature grains have coalesced to form larger grains, the morphology which observed by studying of the selected samples produced at various sintering temperatures (**900°C, 1000°C and 1100°C**) by SEM which showed in the figure (4.8 a, b and c) :

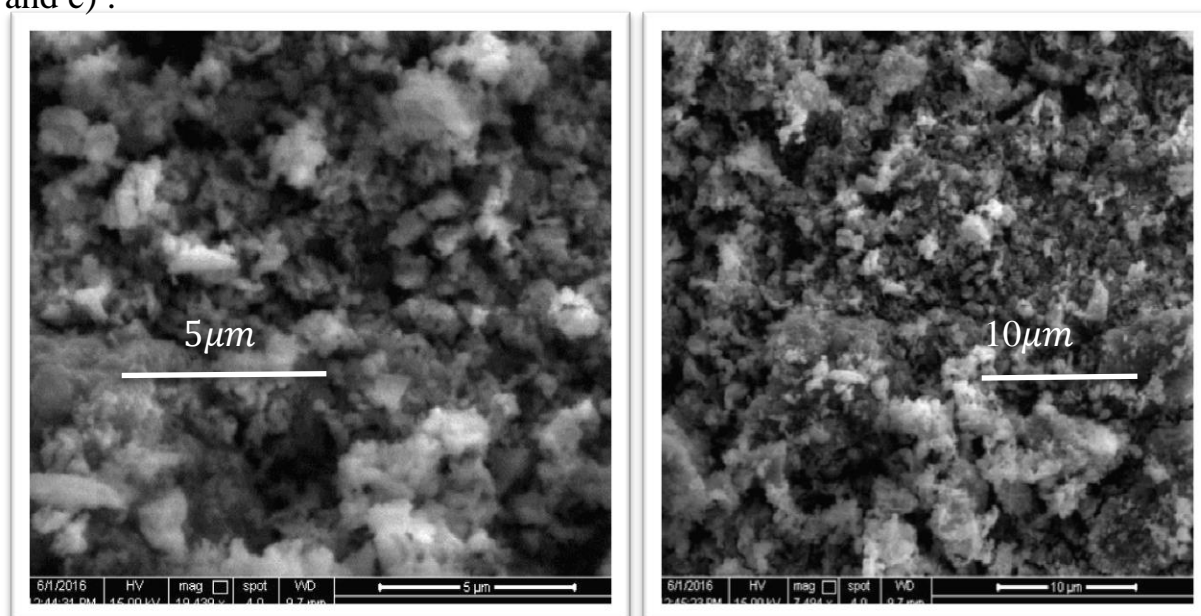


Figure (4.8 a) SEM micrographs of M-type Barium hexaferrite sintered at 900°C for 3h .

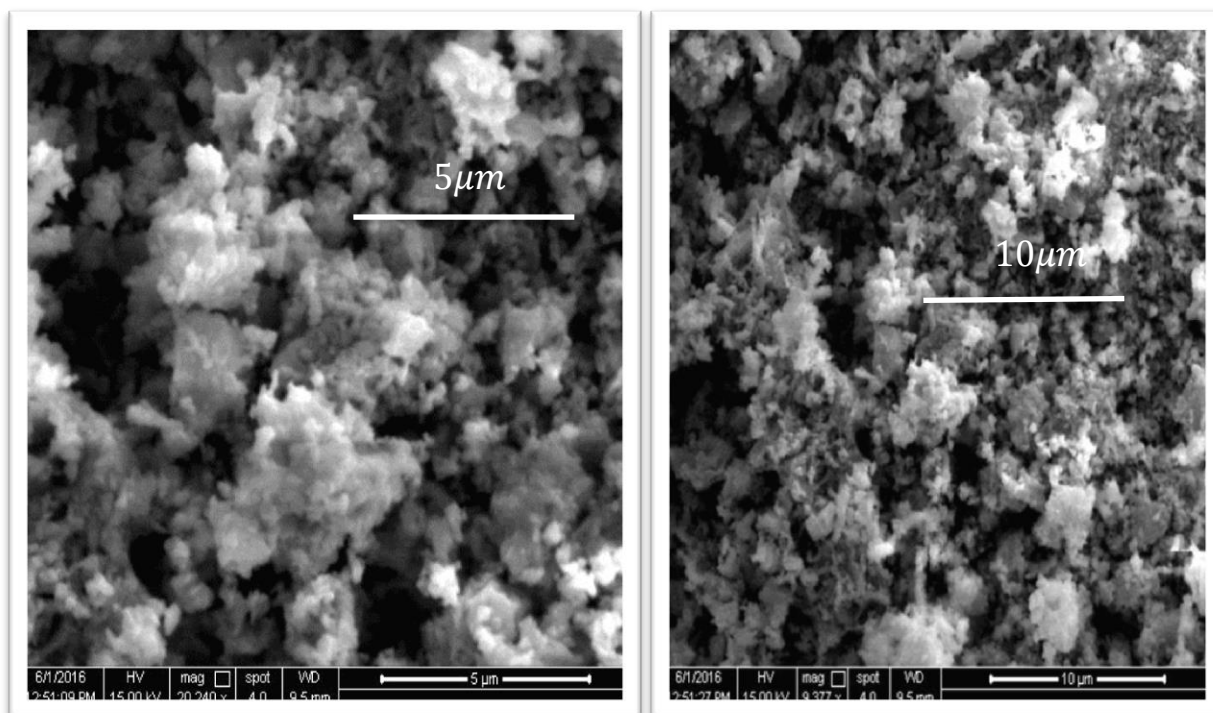


Figure (4.8 b) SEM micrographs of M-type Barium hexaferrite sintered at 1000°C for 3h .

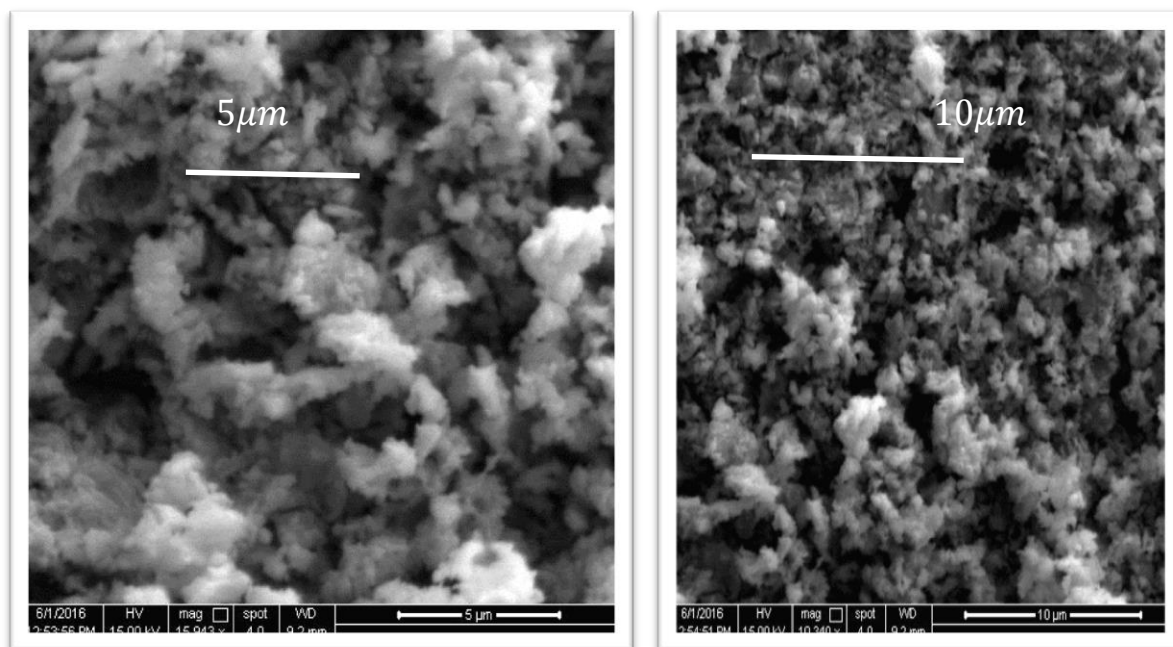


Figure (4.8 c) SEM micrographs of M-type Barium hexaferrite sintered at 1100°C for 3h .

The images shows an agglomerated samples, they are platelet-shaped, more spherical towards a hexagonal shape at higher sintering temperatures as illustrated at 1200°C figure (4.9):

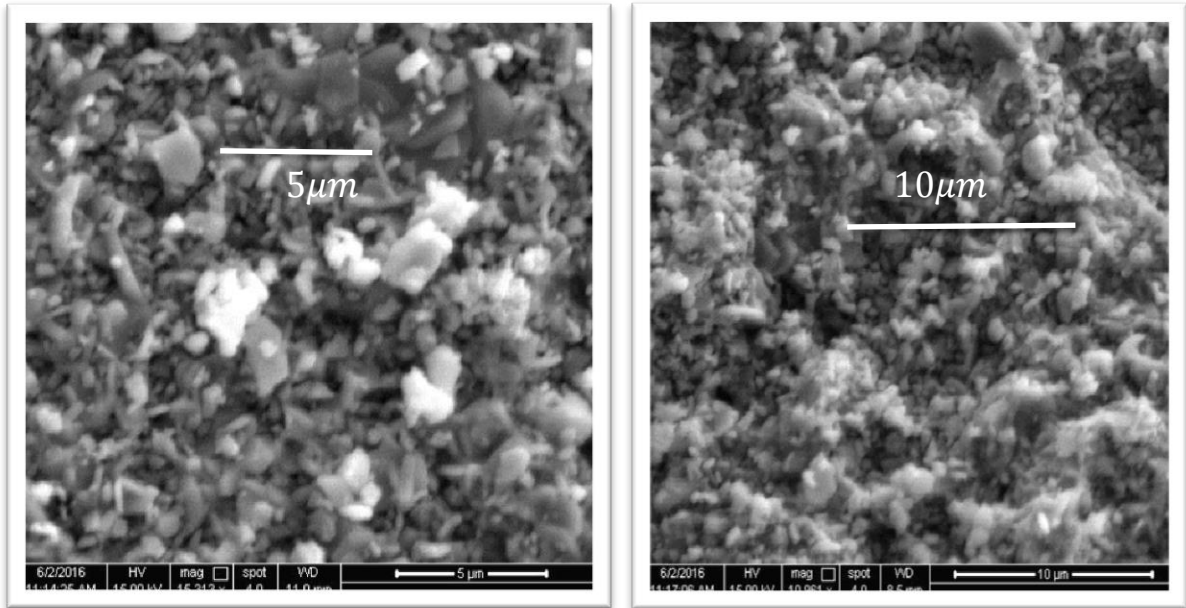
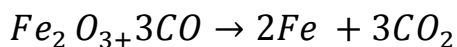


Figure (4.9) SEM micrographs of M-type Barium hexaferrite sintered at 1200°C for 3h .

The average grain size estimated about 0.5, 0.6, 0.8, 1 and 1.3 μm at 800°C,, 900°C, 1000°C, 1100°C and 1200°C respectively. After sintering the pellets we observed changing in colors from rust at 800 and 900°C to barn red 1000°C to brown at 1100°C then to black at 1200°C as shown in figure (3.2), the gradient in the colors is due to the high Iron oxide content.

The carbon monoxide reduces the Iron oxide as in the chemical formula below:



EDX (Energy Dispersive X-ray Analysis) analysis showed that the Oxygen decreases from 32.79% at 800°C to 23.08 at 1200°C, Table (4.3) clarifies the proportions of elements.

Table (4-3) measured proportions of elements, employing EDX analysis.

Temperature (°C)	Wight(%)			Atomic(%)		
	Oxygen	Iron	Barium	Oxygen	Iron	Barium
800	32.79	58.75	14.47	63.91	32.80	13.65
900	28.80	48.62	10.19	65.58	31.72	2.70
1000	23.98	68.99	14.79	52.74	43.47	3.79
1100	30.32	54.14	10.18	64.49	32.99	2.52
1200	23.08	69.10	14.60	51.77	44.41	3.82

4.4 Density measurement result

The bulk density (d_{Bulk}) of all prepared samples has been calculated after sintering using the equation (3.10), the theoretical density (d_{Theo}) calculated for the samples using the equations (3-11) ,(3-12), and the value of porosity has been calculated using equation (3-13), D_{SEM} –grain size estimated from SEM micrographs, (V)- unite cell volume depend on lattice parameters.

At 800°C lattice parameters values approach to standard values with comparison to standard $\text{BaFe}_{12}\text{O}_{19}$ card No-043-0002, $a= 5.892\text{\AA}$, $c= 23.183\text{\AA}$, $V=696.99\text{\AA}^3$, then decreased at 900°C, back to growth gradually in 1000°C and 1100°C, and then approach to standard volume at 1200°C. Table (4.4) shows the value of density and porosity for all prepared barium hexaferrite samples at different temperatures.

Table (4-4): The porosity of barium hexaferrite samples sintered at different temperature (800°C, 900°C, 1000°C, 1100°C and 1200°C)

T(°C)	Lattice constant(Å)		V(Å ³)	D _{x-ray} (nm)	D _{SEM} (μm)	d _{Theo} g/cm ³	d _{Bulk} g/cm ³	p%
	a	c						
800	5.874	23.174	692.46	32.99	0.5	5.331	2.0915	60
900	5.865	23.136	689.21	42.66	0.6	5.356	1.9044	64.44
1000	5.866	23.154	689.98	47.63	0.8	5.350	2.0158	62.32
1100	5.87	23.159	691.07	49.13	1	5.341	2.182	59.14
1200	5.876	23.162	692.67	52.68	1.3	5.329	2.495	53

4.5 Electrical properties for the barium hexaferrite

4.5.1 Dielectric constant

The dielectric properties of ferrites strongly depend on several factors, including the method of preparation, chemical composition and grain size. The frequency dependence of the real and imaginary part of dielectric constant (ϵ' and ϵ'') for all the samples was studied at room temperature in the range of 50Hz to 1MHz, It is observed that all the samples have higher dielectric constant at lower frequency and decreases sharply up to (25175 Hz) and then decreasing gradually with increasing the frequency this behavior is typical of ferrites and a similar behavior was observed by other researchers [88]. The trend can be explained on the basis that at lower frequencies there exist four different types of Polarization (i.e. Electronic, ionic, dipolar and space

Charge) contributions take a part in the dielectric constant, but at higher frequencies some of polarization contributions relax out, result in the lowering of dielectric constant (ϵ_r).

The frequency of electron hopping between the Fe^{+2} and Fe^{+3} ions at octahedral sites is higher as compared to the applied AC field and thus can interact with the applied field easily, resulting in a higher value of dielectric constant at lower frequencies. Contrary to it, at higher frequency the hopping electron cannot follow the frequency of the applied electric field, resulting in lowering of dielectric constant. Consequently, the electron exchange between Fe^{+2} and Fe^{+3} is perturbed at high frequencies, which explains the slower decrease of dielectric constant (ϵ') at high frequency.

Above (25175 Hz) notice a change in the behavior of dielectric constant (ϵ' and ϵ'') for the samples, as shown in Figure (4.10a and b)

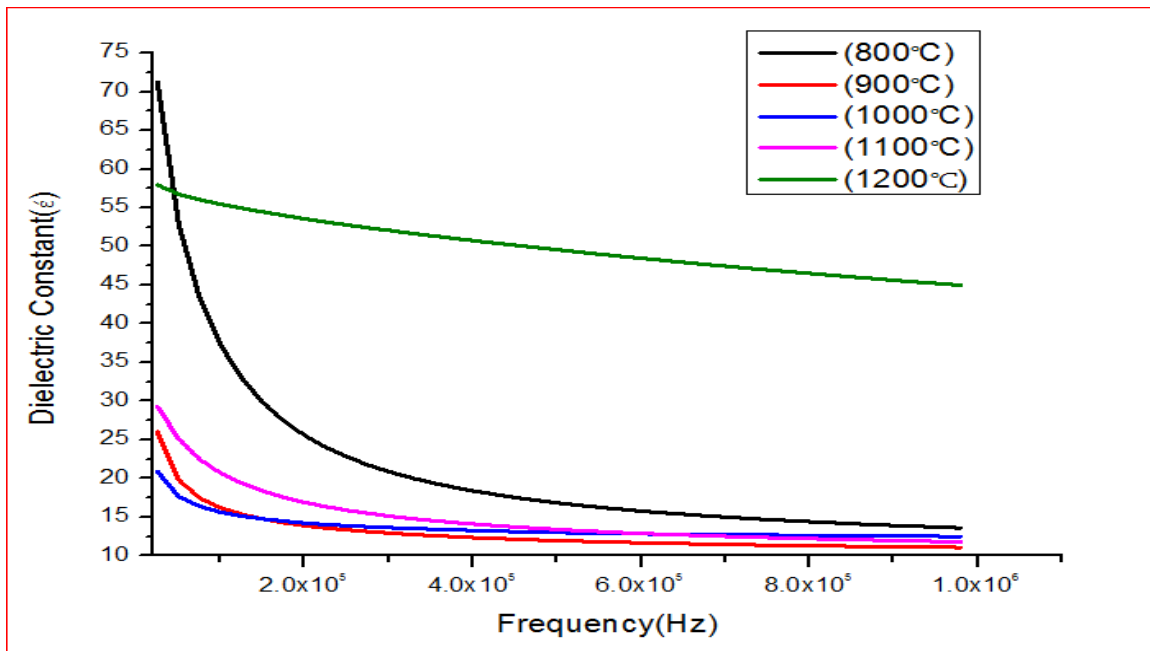


Figure (4.10 a) variation of real part of dielectric constant (ϵ') with frequency (Hz) for the Barium Hexaferrite samples sintered at (800°C, 900°C, 1000°C, 1100°C and 1200°C).

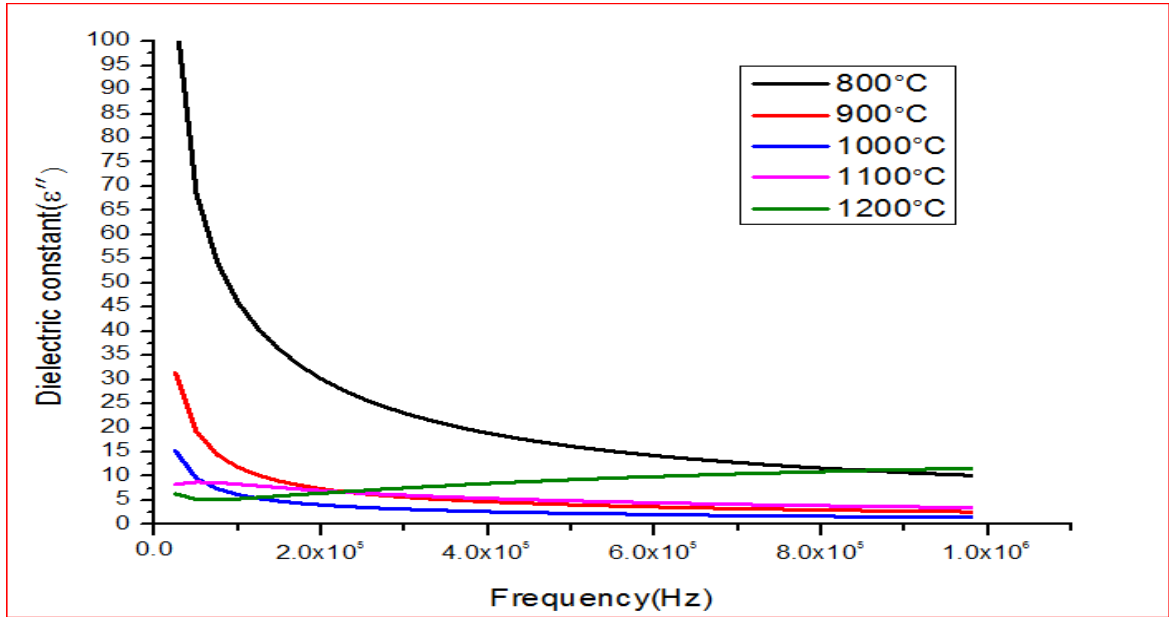


Figure (4.10 b) variation of imaginary part of dielectric constant (ϵ'') with frequency (Hz) for the Barium Hexaferrite samples sintered at (800°C, 900°C, 1000°C, 1100°C and 1200°C).

The variation of dielectric constant with frequency may be explained on the basis of space-charge polarization phenomenon [89], according to this, dielectric material has well conducting grains separated by highly resistive grain boundaries. On the application of electric field, space charge accumulates at the grain boundaries and voltage drops mainly at grain boundaries, Koops proposed that grain boundary affect is more at low frequencies [90]. As the frequency increased beyond a certain limit the electron exchange between Fe^{2+} and Fe^{3+} ions does not follow the variations in applied field, so the value of dielectric constant becomes constant. According to Maxwell and Wagner [91, 92] two layer models, the dielectric structure of ferrite material is assumed to be made of two layers, the first layer being a conducting layer consisting of large conducting ferrite grains separated by the other thin poorly conducting intermediate grain boundaries.

Sintering at higher temperature enhances the Fe^{2+} ions, which are more conducting ions as compared to other cations present in ferrites. The presence of more Fe^{2+} ions due to sintering at higher temperatures, therefore results in high dielectric constant and losses. It's evident that the sample sintering at 800°C have high dielectric constant decrease exponentially with increase in frequency is probably due to small particles exhibited high polarizing while decreasing at 900°C , 1000°C and 1100°C with growth grain size, the small particles filling the spaces between the large particles, the effect of particle size is evident for the samples that have been sintered at 1200°C , enlarge grain size causes an increase in the dielectric constant at low frequencies, In addition sintering at higher temperatures 1200°C will be an abundance of Fe^{2+} ions For this reason has high dielectric constant and decreases linearly with increasing frequency and this corresponds with other theses [88].

4.5.2 A.C –Conductivity

The plot for variations of AC electrical conductivity with frequency is shown in figure (4.11), in the present study; it has been observed that the A.C conductivity gradually increases with an increase in frequency, thus linear nature is then justified. The increase in A.C conductivity with an applied field frequency can be explained on the basis the applied field which facilitates in transferring the charge carriers between different localized states as well as liberate the trapped charges from different trapping centers. At lower frequencies, these grain boundaries are many active, hence the hopping frequency of electron between Fe^{3+} and Fe^{2+} is less at lower frequencies. As the frequency of an applied field increases, the conductive grains become much active in upholding the hopping of electron between Fe^{3+} and Fe^{2+} ions, thereby increasing the hopping frequency.

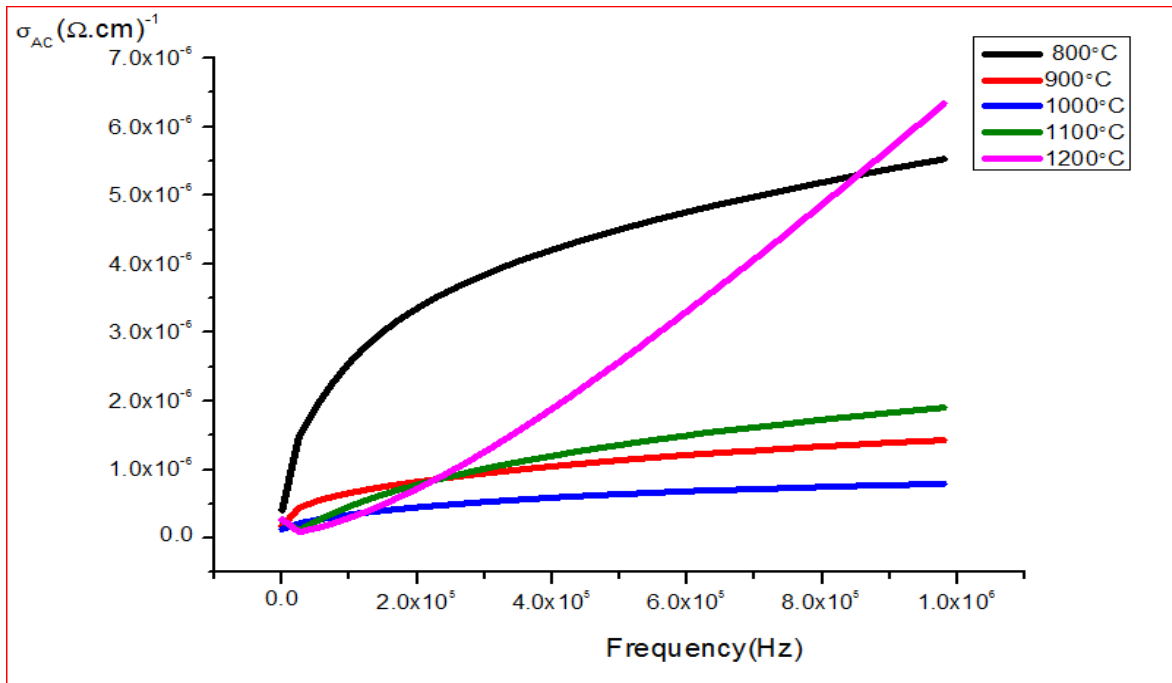


Figure (4.11) variation of A.C conductivity with frequency for barium hexaferrite

It observed high conductance for the sample was sintered at 800°C due to the presence of Nano particles decreases significantly when sintering the sample at 900°C and 1000°C, because of the decreasing in the surface area of contiguous granules then back to increasing at 1100°C and 1200°C, for the samples has been sintered at and 1200°C. It was noted increasing in conductivity, the reason for this is due to the decrease in porosity in addition presence of more Fe^{2+} ions due to sintering at 1200°C contributed to an increase conductive alternating. In case of ferrites, conversion of Fe^{+2} to Fe^{+3} or vice-versa leads to the formation of extra electron or hole. Under the influence of external electrical energy or thermal energy, these extra electrons (or holes) jump from one valence state of iron to the other and constitute the conduction current [88].

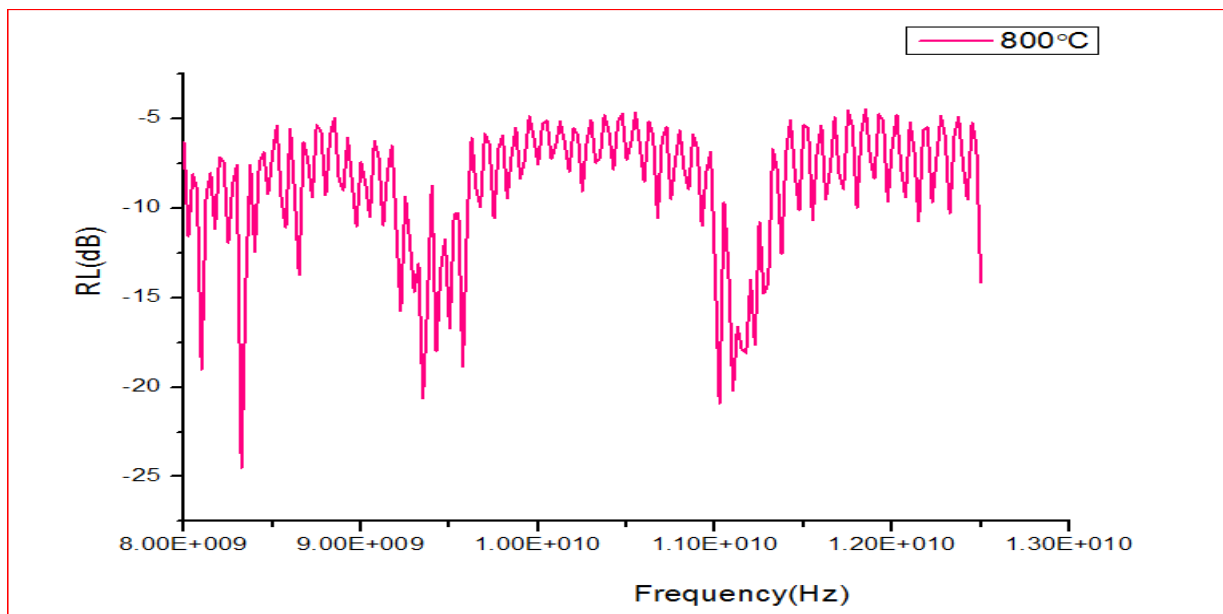
4.6 Microwave characterization

4.6.1 Absorbing Properties

The microwave absorbing characteristics of the barium hexaferrite samples has been carried out in the X-band range (8-12.5) GHz by changing sintering temperature.

Figure (4.12a, b) shows the reflection loss values as a function of frequency for barium hexaferrite using network analyzer system; it was calculated using the equation (3.2) and Figure (4.13) shows the absorption for samples versus frequency it calculated by equation (3.3).

The effect of changing temperature leads to a difference in the composition and affects the density, porosity, and grain size, this leading to a change in attenuation intensity and absorbance values as a result of changing in the scattering parameters (S_{11} and S_{21}).



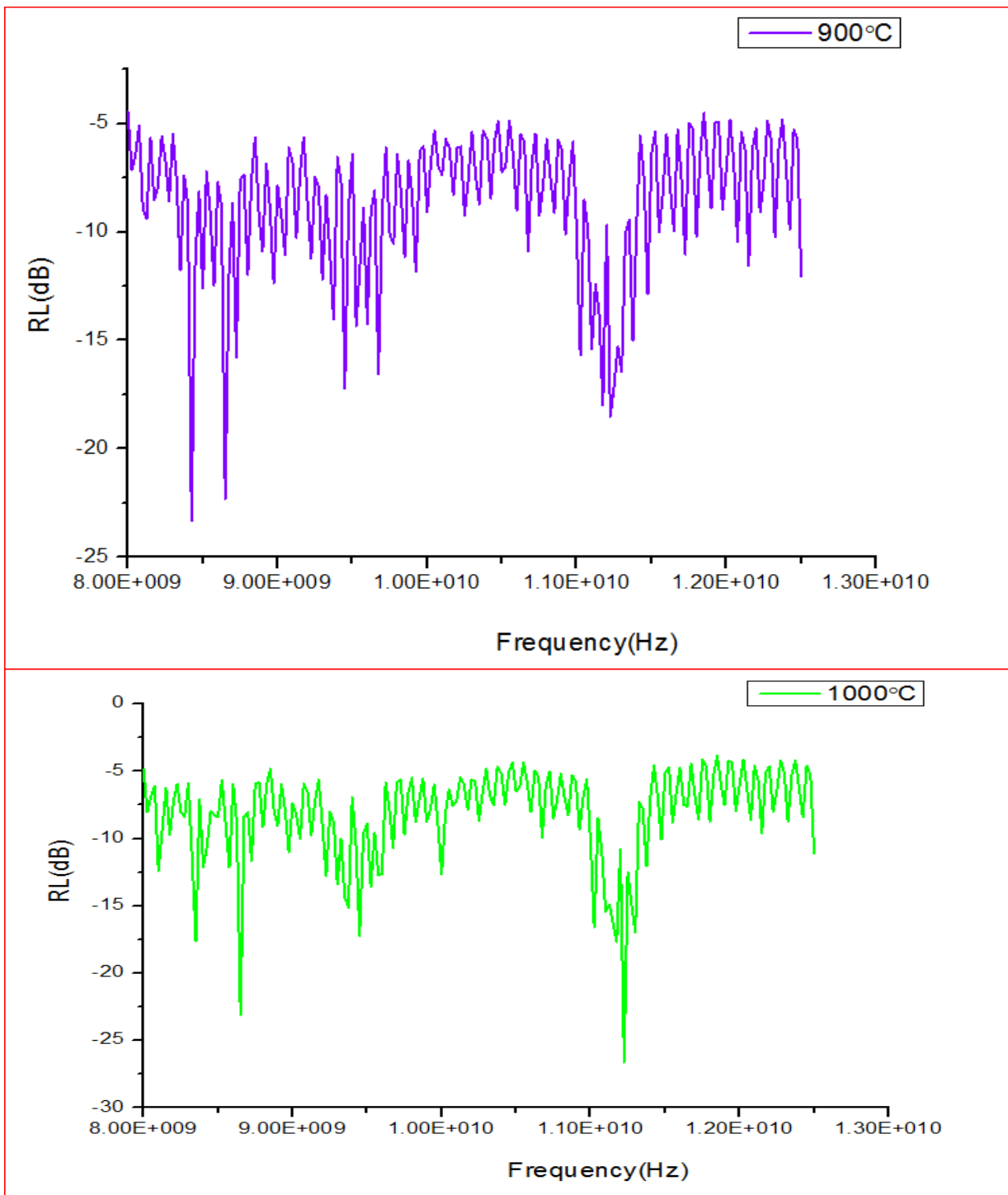


Figure (4.12a): Measured reflection loss for barium hexaferrite sintered at different temperatures (800°C, 900°C and 1000°C).

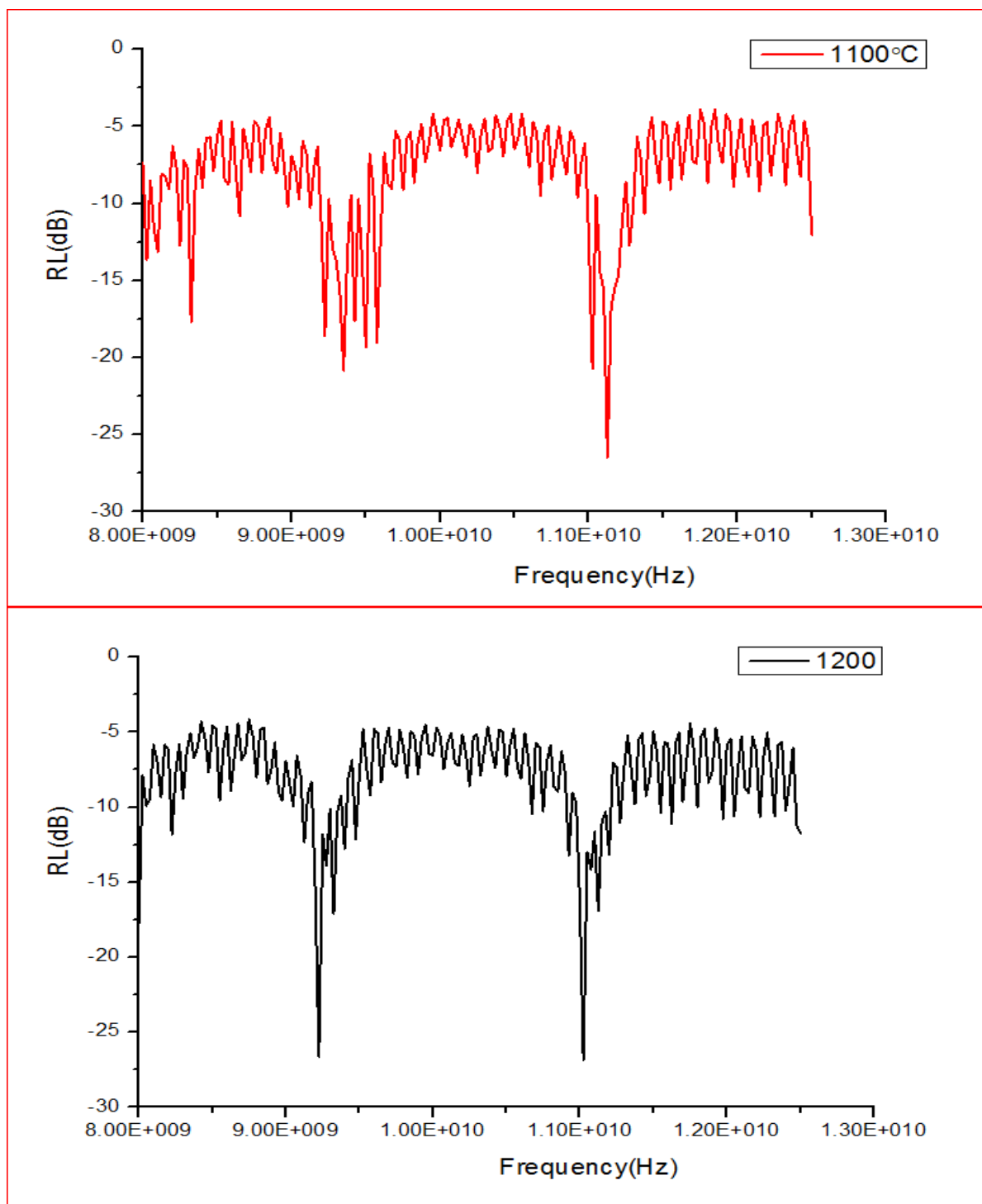


Figure (4.12b): Measured reflection loss for barium hexaferrite sintered at different temperatures (1100°C and 1200°C).

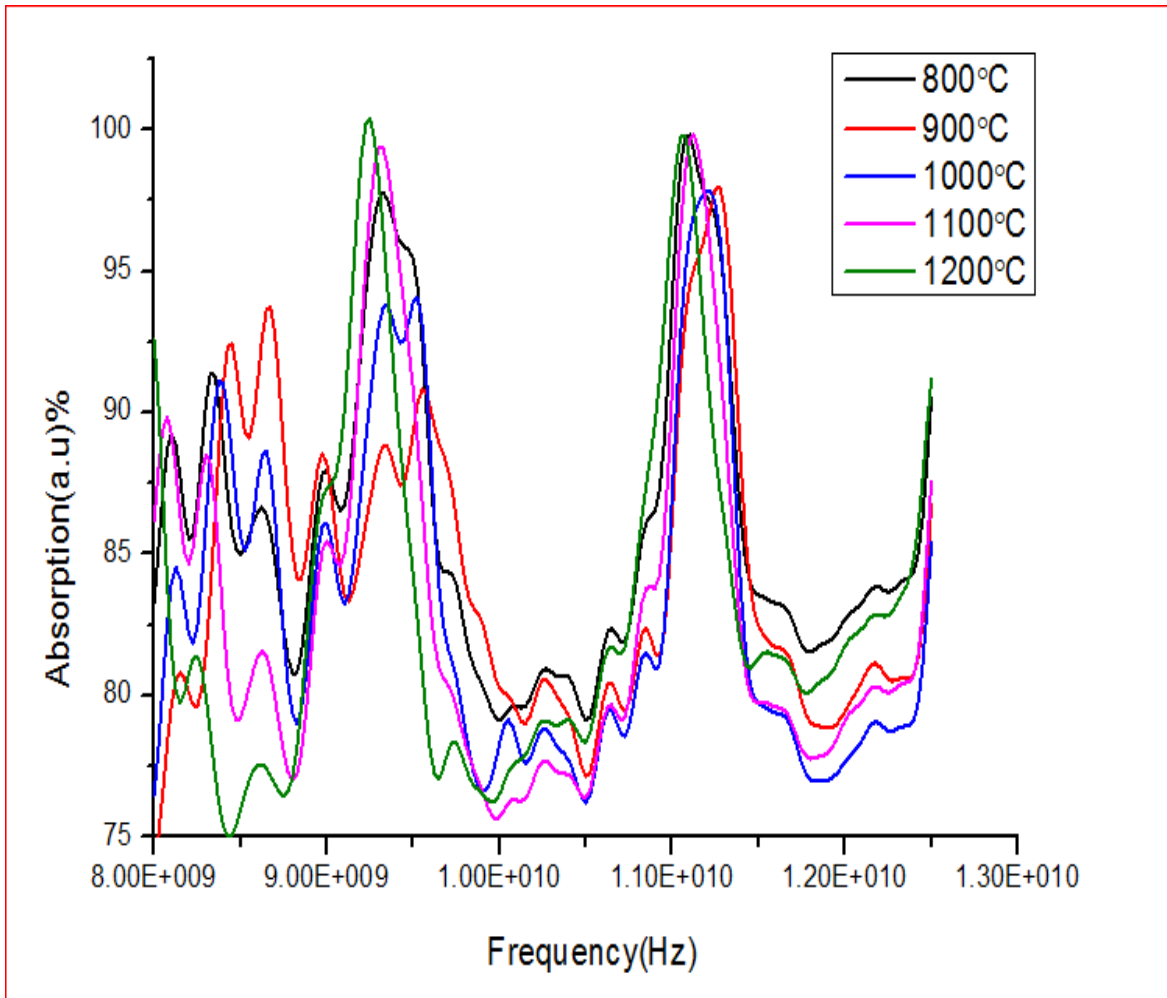


Figure (4.13) showed absorbance curve versus (x-band) microwave frequencies for barium hexaferrite sintering at different temperature.

The M-type hexagonal ferrites are special kinds of absorbing materials due to their dielectric and magnetic losses in the microwave frequency band, the magnetic loss of these materials results from their ferrimagnetism's, the resonance absorption of moving magnetic domains wall and spin relaxation in the high-frequency alternating electromagnetic fields. The critical diameter of the spherical barium ferrite with single magnetic domain is reported to be 460nm [93, 94]. The coercivity could in principle be increased by making the particles smaller or smoother and with fewer crystal imperfections in order to

Decrease the number of sites for wall nucleation [95]. From the figure (4.12, 13); illustrates the existence of two attenuation curves with the presence of some other peaks at low frequencies from (8-9GHz) within the X-band region, Generally observed increasing the value of the attenuation of the samples that has been sintering at (900°C, 1000°C, 1100°C and 1200°C) by increasing the sintering temperature except for the samples that have been sintered at 800°C it behaves differently from other samples, Also it illustrates the increasing of sintering temperature caused to shifted absorption curves tends to lower frequency, It was observed that the attenuation peaks diminish with increased sintering temperature within the frequency range (8.4-8.83) GHz. This behavior is probably due to the particles being sufficiently small to approach single domain characteristics, so that only spin rotations can occur [11], while in other attenuation peaks when the ranges (9.25-9.55) GHz and (11-11.27) GHz noted that with decreasing the porosity due to variation in sintering temperature caused to increasing in attenuation.

4.6.2 Relative Complex permittivity and permeability

In order to investigate the properties of preparing material which use for microwave absorption, complex permittivity and permeability of hexagonal barium ferrite which sintering at different temperature was studied. Complex permittivity ($\epsilon_r = \epsilon' - i\epsilon''$) and complex permeability ($\mu_r = \mu' - \mu''$) represent the dielectric and dynamic magnetic properties of magnetic materials.

The real parts (ϵ' and μ') of the complex permittivity and permeability indicate the storage capability of electric and magnetic energy. The imaginary parts (ϵ'' and μ'') Represent the loss of electric and magnetic energy.

The mechanisms of energy loss in magnetic materials are due to dielectric and magnetic properties, which depend on the imaginary part of the complex permittivity and complex permeability.

Nicholson-Ross-Weir (NRW) method used to calculate both of the permittivity and permeability from the s-parameters, figure (4.14a,b) below; show the real and imaginary part of permittivity it observed an increase in the real part of permittivity with decreasing the porosity within the frequency range (9.4-11.6) GHz Virtually in the regions of attenuation peaks, This increase in the value of the dielectric constant as a result of the contribution of more $\text{Fe}^{+2} \leftrightarrow \text{Fe}^{+3}$ ions in the polarization[14], when comparing the imaginary part of the dielectric constant it observed that increasing with frequency from $(-i)$ part to $(+i)$, when the imaginary part approaching to zero the absorbance curve reducing significantly within the frequency range (10-11GHz)as shown in figure (4.13), also noted the sample have been sintering at 1200°C prevail on the other samples in imaginary part too.

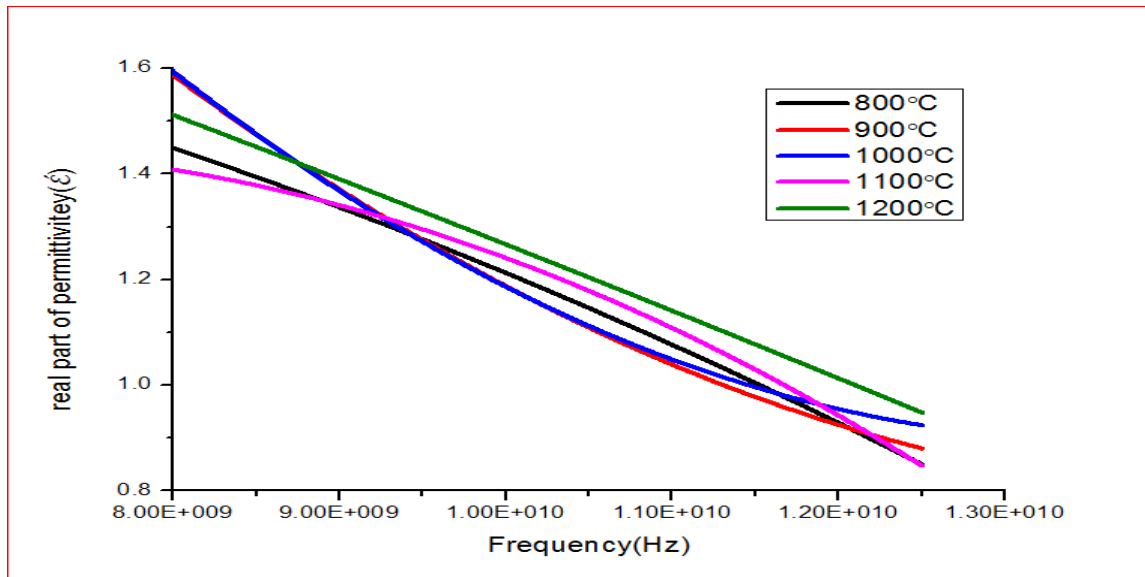


Figure (4.14a) real part of permittivity for hexagonal barium ferrite within frequency range (8-12.5GHz).

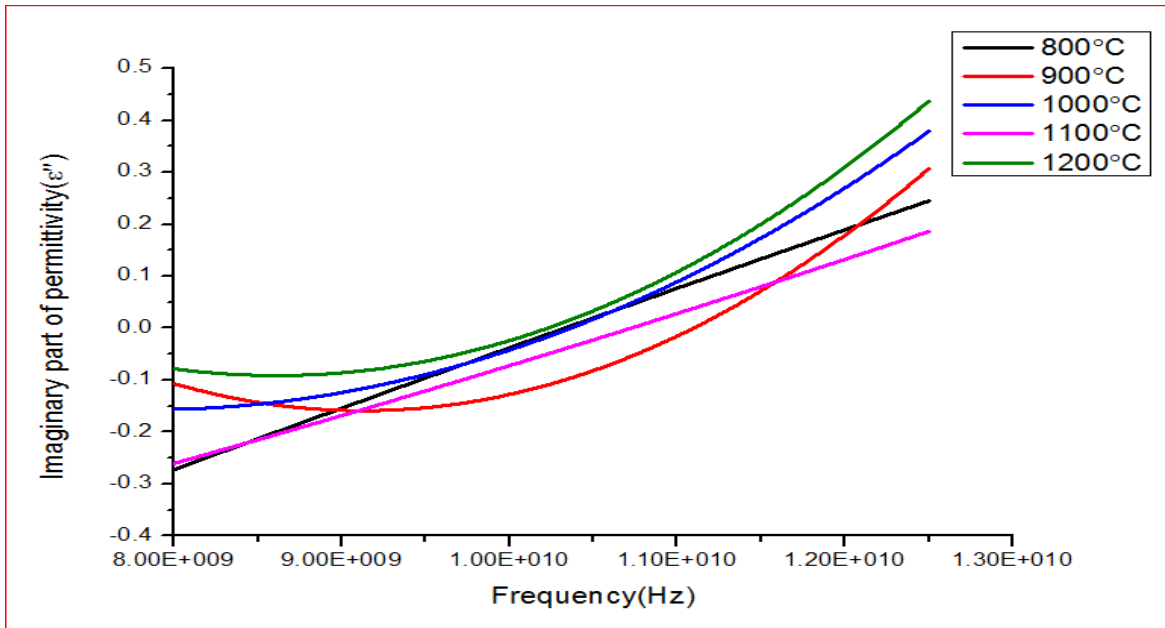


Figure (4.14b) imaginary part of permittivity for hexagonal barium ferrite within frequency range (8-12.5GHz).

The complex permeability of the studied ferrites is shown in Figure (4.15a), it observed the real part of the permeability (μ') An increase with decreasing the porosity within the frequency range (9.4-11.6) GHz Virtually in the regions of two attenuation peaks, These pores constitute barriers preventing domain wall motion.

In addition, the relative permeability increased with increasing grain size, while the sample sintering at 800°C containing particles approaching single domain contribution besides the contribution of larger grains.

In the Figure (4.15b) observed an increase in the imaginary part of permeability for the samples sintering at 800°C, 900°C, 1000°C with an arched in the attenuation zones (9.4-11.6) GHz and then decreases with increasing frequency, this behavior is likely as a result of the contribution of small grains, which is approaching the single domain characteristics with the participation of grains is greater than critical size but for the samples

Sintering at 1100°C and 1200°C it behave differently from other samples due to the increase in grain size with increasing temperature, consequently the reason for a low-value of imaginary part of the permeability then increased with increasing frequency, it concluded from this the grain size which contribute in attenuation has become greater than critical size to leave the single domain characteristics.

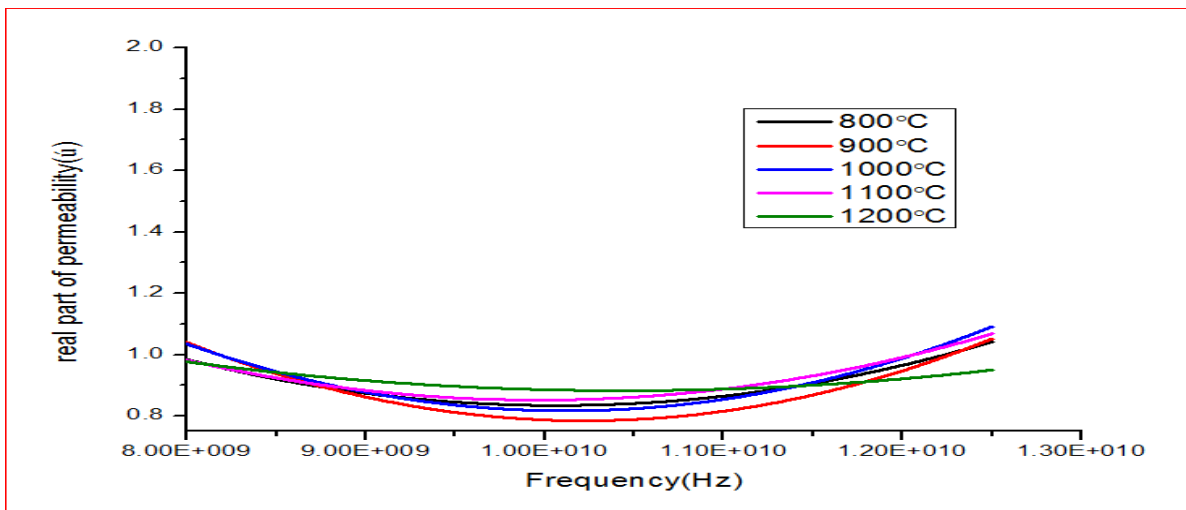


Figure (4.15a) showed real part of permeability of hexagonal barium ferrite at x-band microwave frequencies.

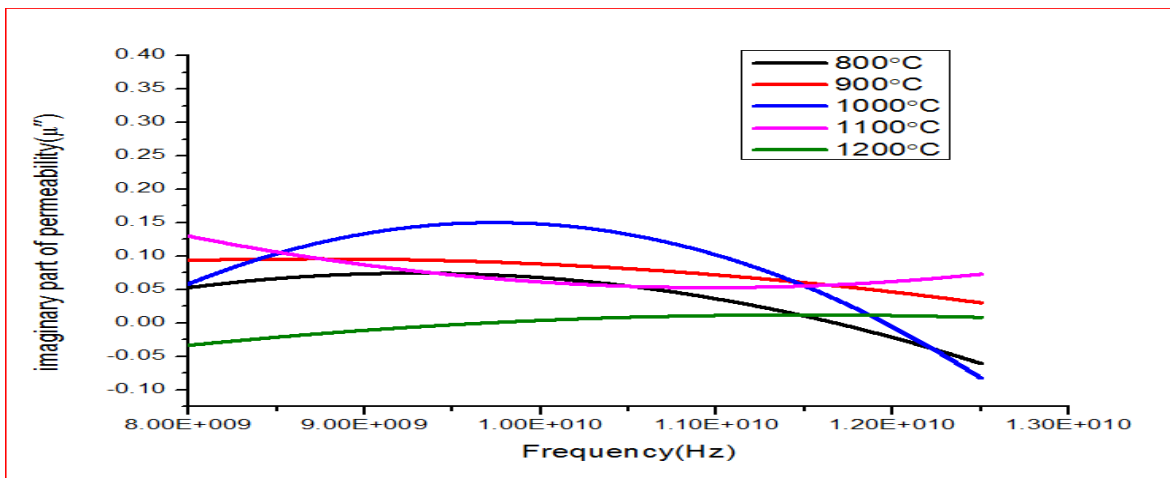


Figure (4.15b) showed imaginary part of permeability of hexagonal barium ferrite at x-band microwave frequencies.

The resonance peaks for barium hexaferrite samples were formed when there is matching between the relative permeability and relative permittivity of ferrite, the dissipative energy is said to have been (absorbed) by the medium due to the electric loss tangent ($\tan \delta_\epsilon$) and magnetic loss tangent($\tan \delta_\mu$), the matched characteristic impedance concept relates to a special class of absorber

where ($\mu_r = \epsilon_r$) And characteristic impedance of the material $Z = \sqrt{\frac{\mu_r}{\epsilon_r}}$ It can be observed through the table (4-5).

Table (4-5) Clarify values of complex permittivity, permeability, characteristic impedance and loss tangent for resonance peaks for prepared samples.

Sintering temperature			800°C				
Frequency(Hz)	Reflection loss(dB)	Complex permittivity(ϵ_r)	Complex Permeability(μ_r)	$\frac{\mu_r}{\epsilon_r}$	$Z = \sqrt{\frac{\mu_r}{\epsilon_r}}$	$\tan \delta_\epsilon = \frac{\epsilon''}{\epsilon'}$	$\tan \delta_\mu = \frac{\mu''}{\mu'}$
8.325E9	-24.49306	0.88629-i0.37283	1.08707-i0.5362	1.22655	1.1074	-0.4206	-0.49327
9.35E9	-20.61566	1.53893-i0.27119	1.10433-i0.5351	0.7176	0.8471	-0.17622	-0.4845
1.1025E10	-20.90651	0.19698-i0.72917	0.21878-i0.326	1.11067	1.0535	-3.70178	-1.49012
1.11E10	-20.18759	0.97835-i0.40432	0.04546-i0.4795	0.04646	0.2144	0.413262	-10.5497
Sintering temperature			900°C				
Frequency(Hz)	Reflection loss(dB)	Complex permittivity(ϵ_r)	Complex Permeability(μ_r)	$\frac{\mu_r}{\epsilon_r}$	$Z = \sqrt{\frac{\mu_r}{\epsilon_r}}$	$\tan \delta_\epsilon = \frac{\epsilon''}{\epsilon'}$	$\tan \delta_\mu = \frac{\mu''}{\mu'}$
8.425E9	-23.31521	0.945-i0.7231	1.0326-i0.131	1.09202	1.045	-0.76472	-0.12754
8.65E9	-22.31886	1.460-i0.0085	1.0696-i0.762	0.73234	0.8557	-0.00584	0.712788
9.45E9	-17.20785	0.9536-i0.4407	1.7515-i0.393	1.8366	1.355	-0.46212	-0.22446
1.1225E10	-18.50206	0.3063-i0.57007	0.6917-i0.227	2.25847	1.5028	-1.86115	-0.329

Sintering temperature			1000°C				
Frequency(Hz)	Reflection loss(dB)	Complex permittivity(ϵ_r)	Complex Permeability(μ_r)	$\frac{\mu_r}{\epsilon_r}$	$Z = \sqrt{\frac{\mu_r}{\epsilon_r}}$	$\tan \delta_\epsilon = \frac{\epsilon''}{\epsilon'}$	$\tan \delta_\mu = \frac{\mu''}{\mu'}$
8.35E9	-17.59996	2.0558+i1.0967	1.0910-i1.57965	0.5307	0.7285	0.53347	-1.44781
8.65E9	-23.12378	1.29475-i0.042	0.73061+i0.8608	0.5642	0.7511	-0.03254	1.1783 3
9.45E9	-17.22998	1.21949-i0.619	1.76275-i0.0933	1.4454	1.2022	-0.50777	-0.05296
1.1225E10	-26.61517	0.63-i0.72721	0.708-i0.1137	1.1251	1.0607	-1.15431	-0.1604
Sintering temperature			1100°C				
Frequency(Hz)	Reflection loss(dB)	Complex permittivity(ϵ_r)	Complex Permeability(μ_r)	$\frac{\mu_r}{\epsilon_r}$	$Z = \sqrt{\frac{\mu_r}{\epsilon_r}}$	$\tan \delta_\epsilon = \frac{\epsilon''}{\epsilon'}$	$\tan \delta_\mu = \frac{\mu''}{\mu'}$
8.325E9	-17.68612	0.9756-i0.5345	1.2911-i0.26208	1.32327	1.1503	-0.54787	-0.20299
9.35E9	-20.82629	1.63081-i0.432	1.2207-i0.3015	0.74854	0.8651	-0.26491	-0.24701
1.1125E10	-26.46759	0.41503-i0.48	0.60332-i0.2926	1.45368	1.2056	-1.16257	-0.48506
Sintering temperature			1200°C				
Frequency(Hz)	Reflection loss(dB)	Complex permittivity(ϵ_r)	Complex Permeability(μ_r)	$\frac{\mu_r}{\epsilon_r}$	$Z = \sqrt{\frac{\mu_r}{\epsilon_r}}$	$\tan \delta_\epsilon = \frac{\epsilon''}{\epsilon'}$	$\tan \delta_\mu = \frac{\mu''}{\mu'}$
9.225E9	-26.64854	0.25553-i0.715	0.15155-i0.19768	0.59309	0.77012	-2.79904	-1.30439
1.1025E10	-26.8813	0.37168-i0.737	0.5402-i0.2292	1.45339	1.20557	-1.98312	-0.42439

4.7 microwaves absorbing composites

With the development of electronic technologies and microwave technology caused electromagnetic interference (EMI)(refers to any undesirable signals) thus; has been a requirement for new materials for the application in the field of shielding and stealth technology, Microwave shielding has been applied to different devices such as computers, mobile phones, aircraft avionics and stealth technology.

EM wave energy can be completely absorbed and dissipated into heat through magnetic losses and dielectric losses if the characteristic impedance of free space is matched with the input characteristic impedance of an absorber [96].

Microwave absorbers are produced by the modification of the dielectric and magnetic properties of the physical characteristics of the compound to allow the absorption of microwave energy for broadband wave attenuation [97].

The objective of this study was the advancement of microwave shielding composites based formation composite consists of barium hexaferrite powder sintering at 1200°C (known to be magneto-dielectric) and/or barium titanate powder (ferroelectrics material) in epoxy resin (as Sticky then fixed medium), preparation method was explained in the previous chapter (3-5), denoted to the specimens ($A_{0:0}$, $A_{4:0}$, $A_{3:1}$, $A_{2:2}$, $A_{1:3}$, $A_{0:4}$) depending on the mixing ratios of the components.

4.8 X-Ray Diffraction Result for (BaTiO₃)

Barium titanate prepared by conventional solid-state reaction method, the XRD pattern of BaTiO₃ powder Figure (4.16) exhibit typical peaks that can be indexed to the standard pattern of BaTiO₃ crystals (JCPDS 05-0626).

X-ray testing illustrated Tetragonal system with lattice constant measured ($a=3.98\text{\AA}$, $c=3.997\text{\AA}$) this results good agreement with standard pattern ($a=3.994\text{\AA}$, $c=4.038\text{\AA}$) also ;average particle size measured from strongest three peaks by using the Debye-Scherrer method ($D = 32.58\text{nm}$).

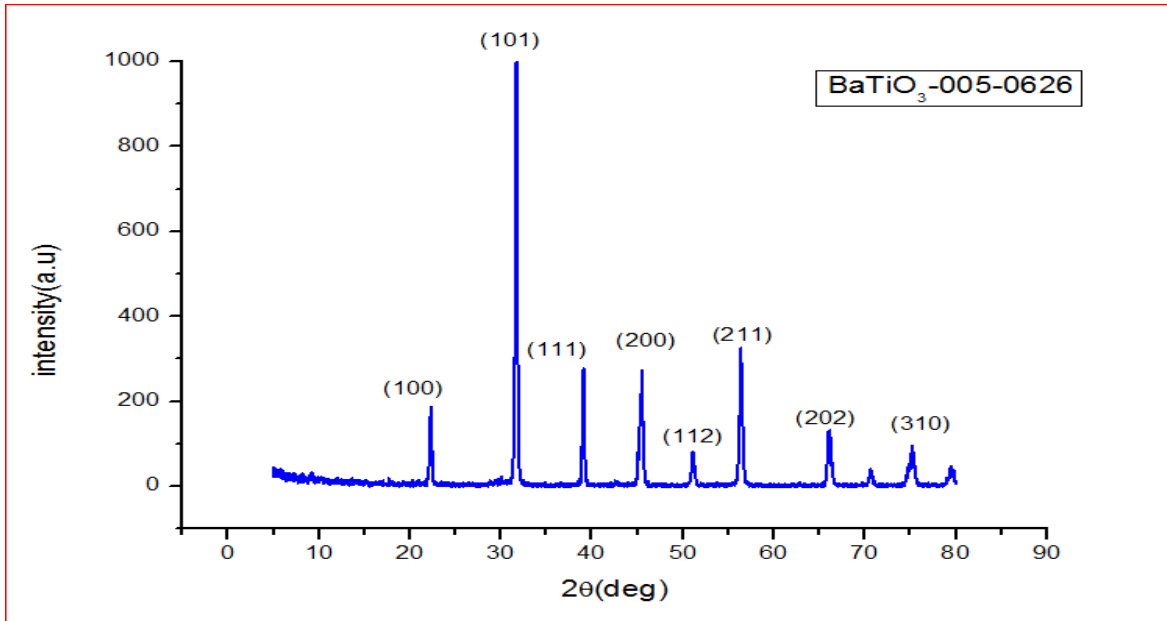


Figure (4.16) XRD patterns for the barium titanate powder

4.9 Microwave characters for the composites

4.9.1 Absorbing Properties

The absorbance tests of the composites have been carried out by changing mixing ratios of the components, and then study the physical characteristics of the compound at the X-band range (8-12.5) GHz.

Figure (4.17a, b) shows the reflection loss values as a function of frequency to the specimens using network analyzer system; it was calculated using the equation (3.2) and Figure (4.18) shows the absorption for samples versus frequency it is calculated by equation (3.3).

The effect of changes in the mixing ratios of the component leads to a changing in the attenuation intensity and absorbance values due to changes in the scattering parameters (S_{11} and S_{21}).

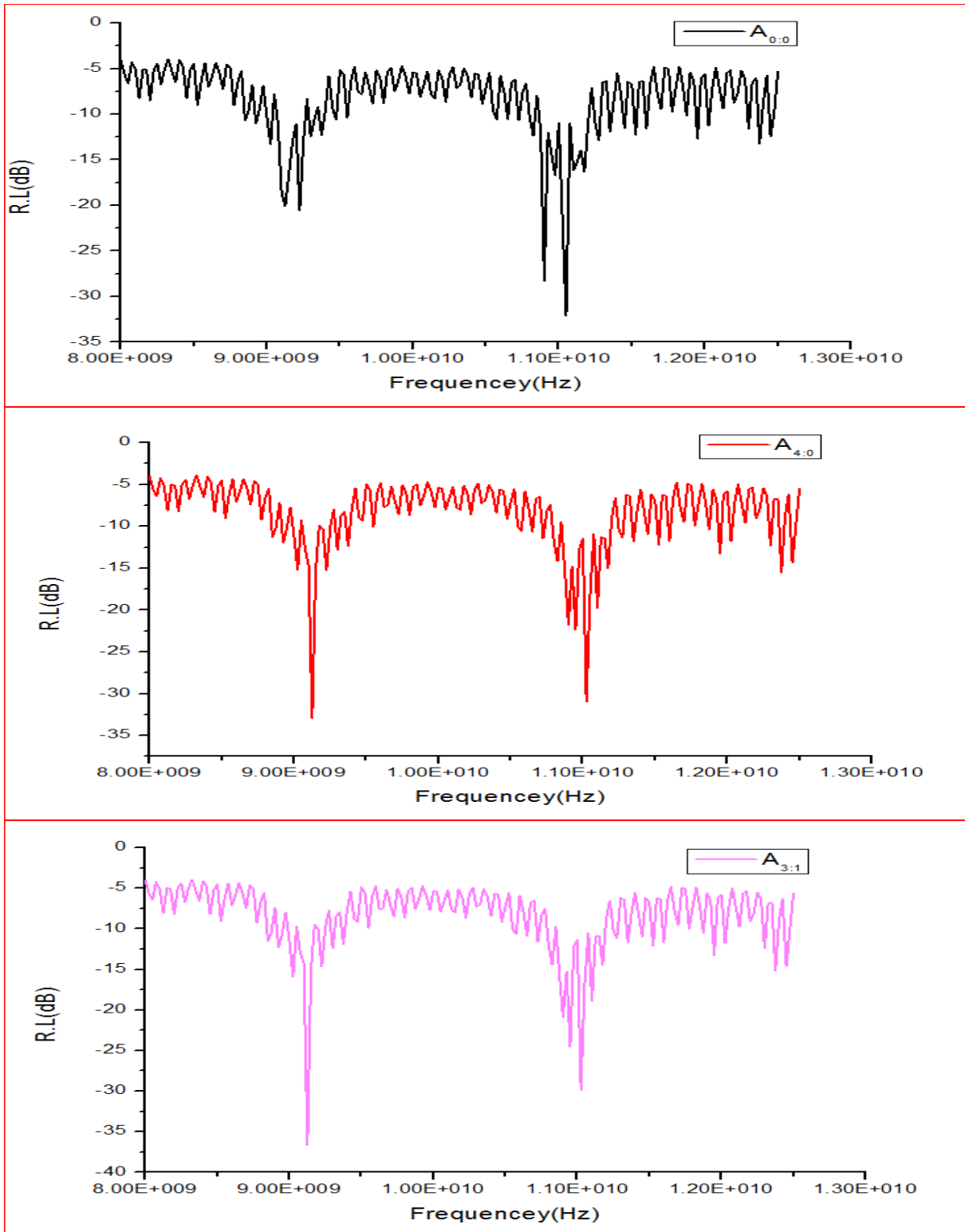


Figure (4.17a) showed the reflection loss values as a function of frequency for samples $A_{0:0}$, $A_{4:0}$ and $A_{3:1}$

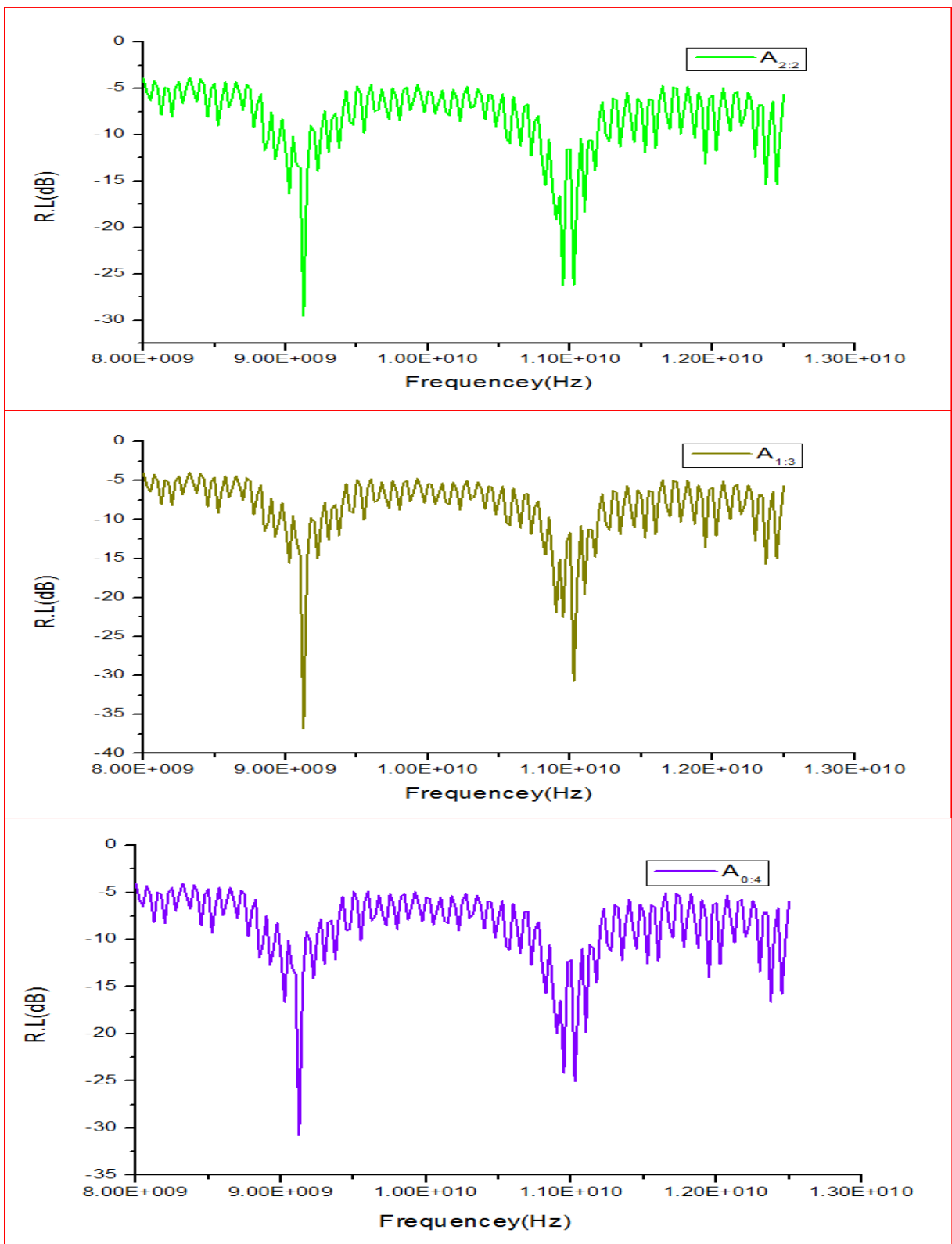


Figure (4.17b) showed the reflection loss values as a function of frequency for samples $A_{2:2}$, $A_{1:3}$ and $A_{0:4}$

The scattering parameters S_{11} & S_{21} , were used to calculate the attenuation coefficient (reflection loss) in (dB) unit by the equation:

$$(\text{Attenuation Coefficient}) = -20 \text{Log}|s_{11}| \dots \dots \dots (3.2)$$

Figure (4.17a, b) for un doped samples ($A_{0:0}$) observed the reflection loss equal -21.50 dB at 11.025 GHz and it reach the value -30.95 dB when it was doped with barium hexaferrite (sample $A_{4:0}$) then attenuation decreases with reduction the content of ferrite as in the samples $A_{3:1}$, $A_{2:2}$, $A_{0:4}$ -29.82 dB, -26.179 dB, -25.04 dB respectively except $A_{1:3}$ the attenuation is equal -30.75 dB , the absorbing properties increases with the concentration of $BaFe_{12}O_{19}$ in composite materials because it appeared absorption resonance frequency at 11.025 GHz but for the sample $A_{1:3}$ the weight ratio of $BaFe_{12}O_{19}$ / $BaTiO_3$ 1:3 the dielectric properties have perfectly matched with the magnetic properties[91].

After the resonant frequency of barium hexaferrite, the attenuation peaks observed at 9.125 GHz with the values -20.08 dB, -32.93 dB, -36.62 dB, -29.52 dB, -36.83 dB, -30.7 dB for samples $A_{0:0}$, $A_{4:0}$, $A_{3:1}$, $A_{2:2}$,and $A_{0:4}$ respectively the samples $A_{1:3}$ showed high attenuation and less than in $A_{3:1}$ and minimum attenuation for doped sample $A_{2:2}$,

So we conclude the value of attenuation progressive according to suitable matching between the dielectric properties and magnetic properties, for the same reason increasing absorbance of Epoxy-resin (EUXIT 50) templates based on the composite which doping by the materials ($BaTiO_3$, $BaFe_{12}O_{19}$) was observed as shown in figure (4.18).

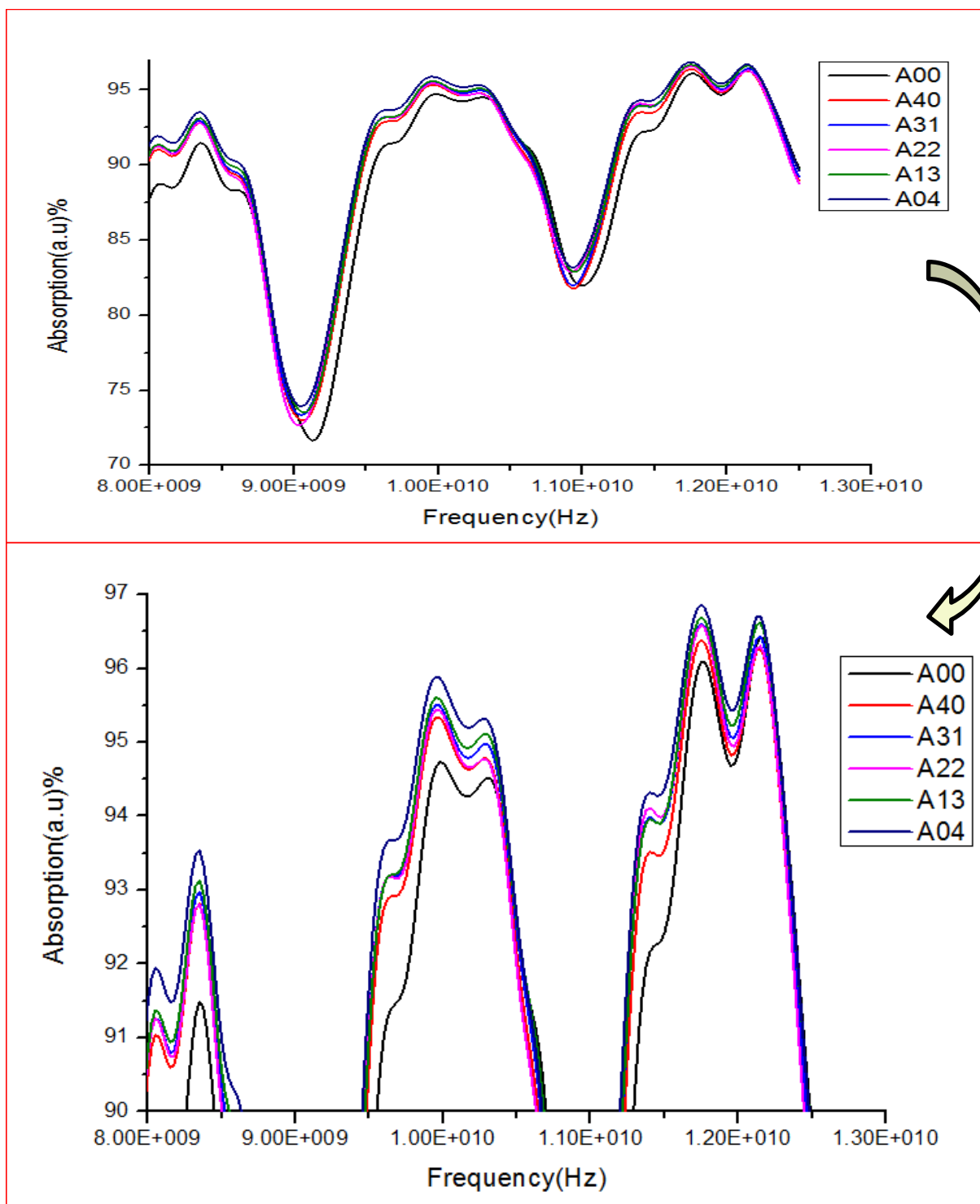


Figure (4.18) showed absorbance curve versus microwave frequencies (x-band) for composite templates.

4.9.2 Relative Complex Permittivity and Permeability

To infer a mechanism of microwave absorption, we determined the real and imaginary parts of complex permittivity (ϵ_r' , ϵ_r'') and permeability (μ_r' , μ_r'') from the scattering parameters S_{11} & S_{21} by using the Nicolson- Ross- Weir (NRW) method, where the real part (ϵ_r' , μ_r') is a measure of how much energy from an external electric/ magnetic field is stored in a material; the imaginary part (ϵ_r'' , μ_r'') is called the energy dissipated and is a measure of how dissipative or lossy a material is to an external electric/magnetic field, for non-magnetic material presume (NRW) method ($\mu_r=1$) for this reason, we assume for samples $\mathbf{A}_{0:0}$, $\mathbf{A}_{0:4}$ ($\mu_r=1$), The positive ions Ba^{+2} and Fe^{+3} at their respective positions form the electric dipoles with the surrounding negative O^{2-} ions, contributing to dielectric constant (ϵ_r') through dipolar polarization and by dipole relaxation to dielectric loss (ϵ_r'') [14], The electron hopping between Fe^{+3} and Fe^{+2} ions also contribute to the dielectric loss due to boost conduction mechanisms giving rise to another relaxation frequency [98,99].

BaTiO_3 has face centered cubic (fcc) structure in which the Ti^{4+} ions have six-fold coordination, surrounded by an octahedron of O^{2-} ions and Ba^{2+} ions have 12-fold cub-octahedral coordination.

BaTiO_3 has permanent dipoles and it absorbs electrical energy, an applied electric field creates a torque on electric dipole and the dipole rotate to align with the electric field orientation polarization occurs, at microwave frequencies the electric field energy changes quickly, the friction accompanying the lack of alignment leads to energy dissipation in a form of heat.

Magnetic field loss occurs due to hysteresis loss, eddy-current loss and residual loss [21].

For ferrite–polymer composites, the contribution to dielectric constant and dielectric loss also occur due to interfacial polarization and its relaxation as the Semiconducting ferrite particles separated by insulating matrix molecules giving the cause of heterogeneity.

Diverse relaxation frequencies of various dipoles formed in the ferrite structure, hopping of electrons and the relaxation due to interfacial polarization all are responsible for the oscillatory behavior of absorption in the samples [100]

In Figure (4.19) observed self-identification real part of permittivity for the samples $\mathbf{A}_{4:0}$, $\mathbf{A}_{3:1}$, $\mathbf{A}_{2:2}$, $\mathbf{A}_{1:3}$ the value of dielectric constant (ϵ') Decreases with the increase in frequency and be higher than in pure epoxy sample ($\mathbf{A}_{0:0}$), while for the sample $\mathbf{A}_{0:4}$ it was noted that the value of (ϵ') less than it is in pure epoxy due to diminution interfacial polarization caused decrease the value (ϵ') with constancy, its value between 1.3&1.4 in the x-band bandwidth.

For samples $\mathbf{A}_{4:0}$, $\mathbf{A}_{3:1}$, $\mathbf{A}_{2:2}$, $\mathbf{A}_{1:3}$ also observed matching the imaginary part (ϵ'') With changed slightly in the imaginary part (ϵ'') With varying the frequency because hysteresis loss occurs due to presence of barium hexaferrite in the composite, there is a distinct variation with frequency for the samples $\mathbf{A}_{0:0}$ & $\mathbf{A}_{0:4}$ which decreases with the increase in frequency, The electric field loss is caused by the dielectric relaxation effect associated with permanent & induced molecular dipoles [90].

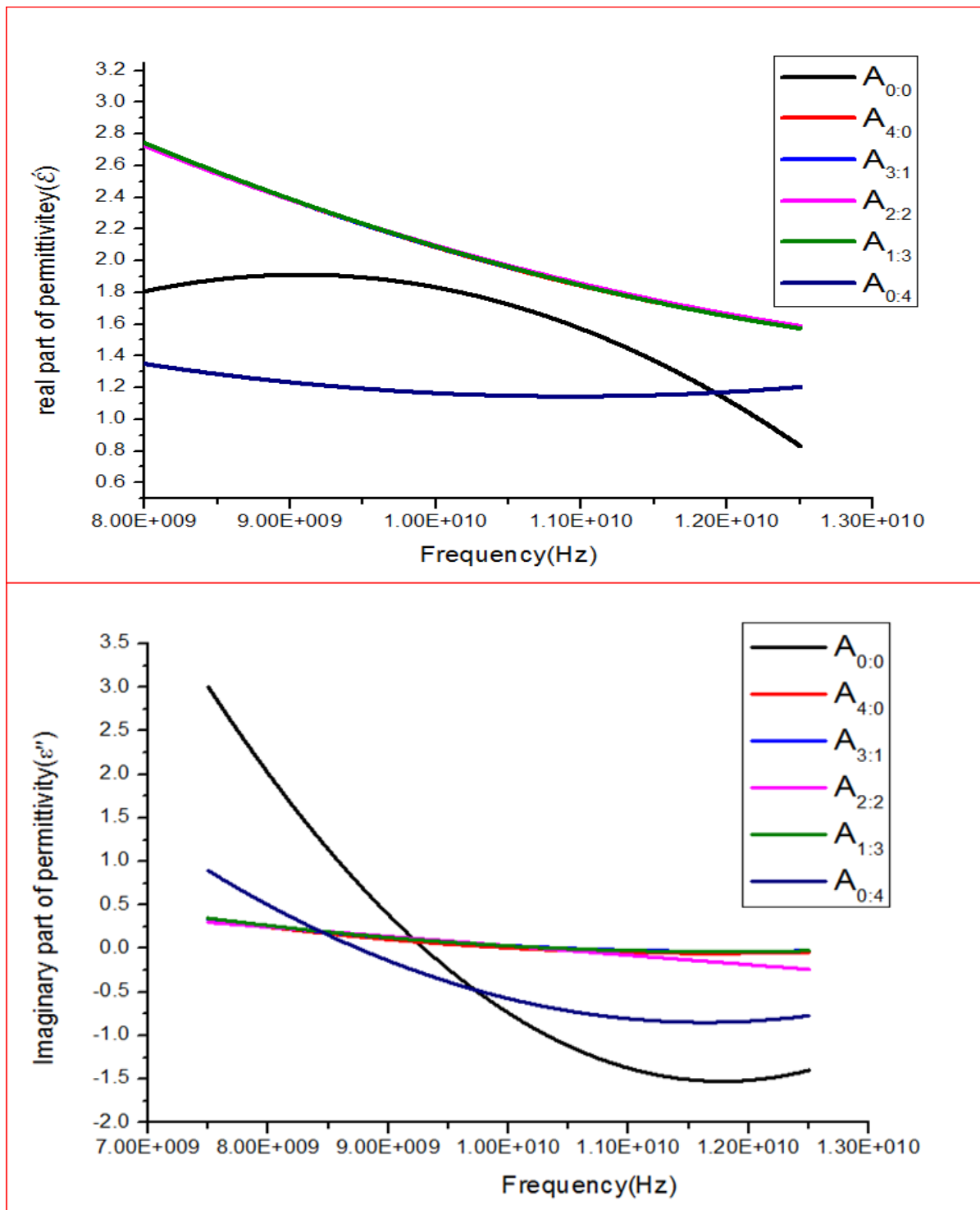


Figure (4.19) showed real and imaginary part of permittivity for composite samples $A_{0:0}$, $A_{4:0}$, $A_{3:1}$, $A_{2:2}$, $A_{1:3}$ and $A_{0:4}$

Fabricated composites $A_{0:0}$, $A_{0:4}$ are purely non-magnetic the real and imaginary parts are equal ($\mu'_r = 1, \mu''_r = 0$), hence omitted in the figure (4.20),

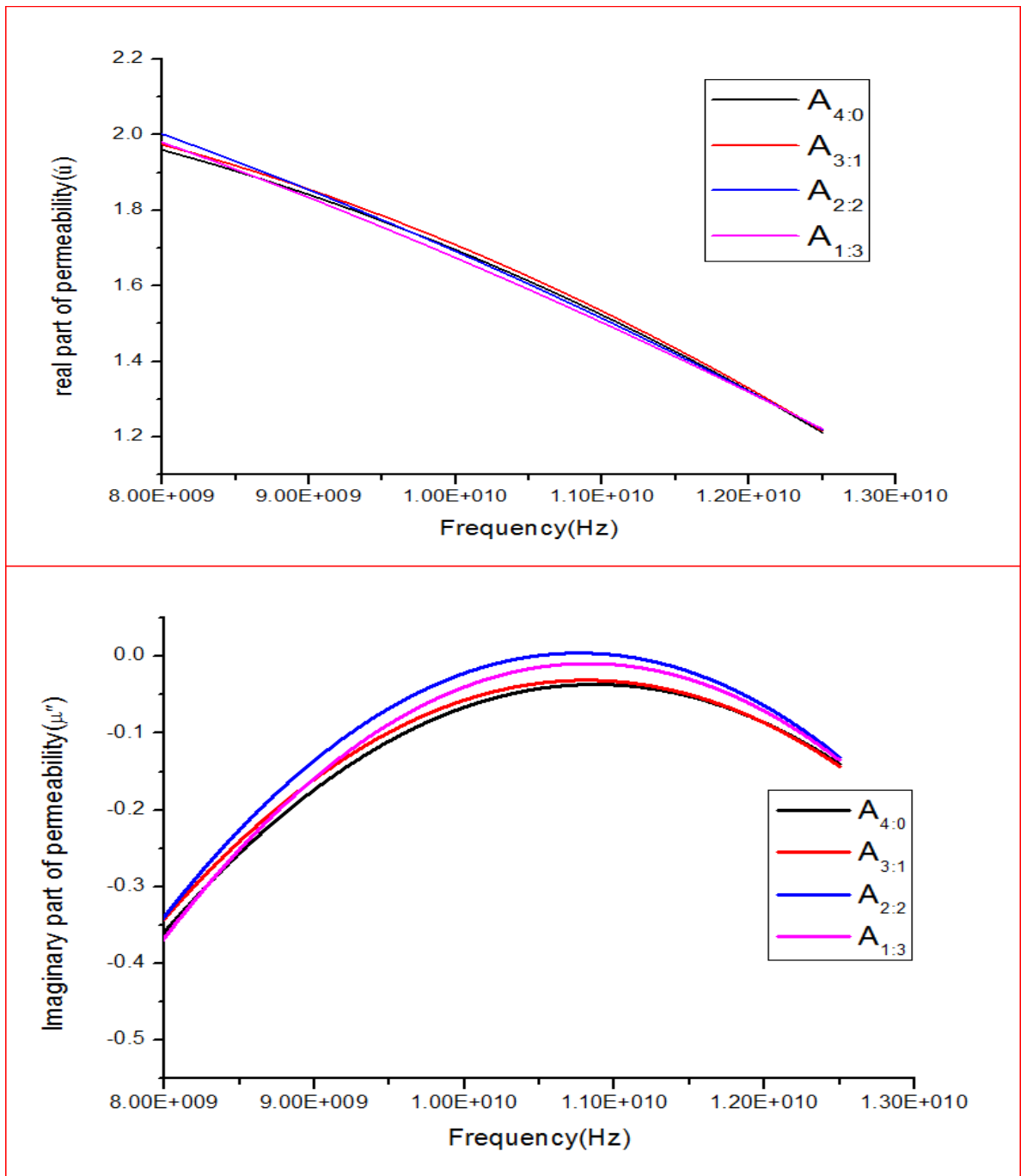


Figure (4.20) showed real and imaginary part of the permeability spectra of composite samples $A_{4:0}$, $A_{3:1}$, $A_{2:2}$ and $A_{1:3}$.

The figure illustrated a real part of magnetic permeability exhibiting excellent rapprochement for the samples $A_{4:0}$, $A_{3:1}$, $A_{2:2}$, $A_{1:3}$ with gradually decreases for increasing frequency, there is a significant observation; the complex permeability measured for composite material which have been calculated using (NRW) method it was larger than pure material for barium hexaferrite sintering at 1200°C because the scattering parameters S_{11}

(related to the radiation emission from port 1 and collect in port 1) and S_{21} (scattering parameter related to the radiation emission from port 1 and collect in port 2) experience from overlapping attenuation aggregate from ferrite and epoxy -resin this is caused the spurious values of the magnetic permeability.

While the imaginary part of permeability for the samples $A_{4:0}$, $A_{3:1}$, $A_{2:2}$, $A_{1:3}$ rapprochements and possess the same characteristics, it increases with increasing frequency to reach the its maximum value at the frequency 10.75GHz then decreases with increasing the frequency.

Resonance peaks observed for all samples $A_{0:0}$, $A_{4:0}$, $A_{3:1}$, $A_{2:2}$, $A_{1:3}$ and $A_{0:4}$ due to matching the relative permeability and relative permittivity for the composite, reflection loss -10 dB, corresponding to 90% attenuation for the incident wave, the dissipative energy is said to have been (absorbed) by the medium due to the electric loss tangent ($\tan \delta_\epsilon$) And magnetic loss tangent ($\tan \delta_\mu$), the matched characteristic impedance concept relates to a special class of absorber where ($\mu_r = \epsilon_r$) And characteristic impedance of the

material $z = \sqrt{\frac{\mu_r}{\epsilon_r}}$ It can be observed through the table (4.6a,b and c).

Table (4-6 a): clarify the values of complex permittivity and permeability, characteristic impedance, loss tangent for resonance peaks for the sample (A_{0:0}).

Pattern			A _{0:0}				
Frequency(Hz)	Reflection loss(dB)	Complex permittivity(ϵ_r)	Complex Permeability(μ_r)	$\frac{\mu_r}{\epsilon_r}$	$Z = \sqrt{\frac{\mu_r}{\epsilon_r}}$	$\tan \delta_\epsilon = \frac{\epsilon''}{\epsilon'}$	$\tan \delta_\mu = \frac{\mu''}{\mu'}$
9.1E9	-18.54426	1.56351+i0.47718	1	0.63959	0.79974	0.3052	0
9.125E9	-20.08573	1.90542-i0.15984	1	0.52482	0.72444	-0.08389	0
9.225E9	-20.54724	1.03175-i0.35677	1	0.96922	0.98449	-0.34579	0
1.09E10	-28.33544	1.15385-i0.04426	1	0.86667	0.93095	-0.03836	0
1.105E10	-32.11791	3.00821-i1.30595	1	0.33242	0.57656	-0.43413	0

Table (4-6 b): clarify the values of complex permittivity and permeability, characteristic impedance, loss tangent for resonance peaks for the samples A_{4:0}&A₃:

pattern			A _{4:0}				
Frequency(Hz)	Reflection loss(dB)	Complex permittivity(ϵ_r)	Complex Permeability(μ_r)	$\frac{\mu_r}{\epsilon_r}$	$Z = \sqrt{\frac{\mu_r}{\epsilon_r}}$	$\tan \delta_\epsilon = \frac{\epsilon''}{\epsilon'}$	$\tan \delta_\mu = \frac{\mu''}{\mu'}$
9.125E9	-32.93534	2.44846+i0.8314	2.4095+i0.64189	0.98409	0.99201	0.33956	0.2664
1.09E10	-21.78432	3.35646-i1.29393	2.53274-i0.3935	0.75459	0.86867	-0.3855	-0.15537
1.095E10	-22.33917	0.034-i0.85187	0.33761-i 0.7875	9.92834	3.15093	-25.0516	-2.33273
1.1025E10	-30.95955	1.10938+i0.86581	1.03358+i0.7537	0.93167	0.96523	0.78044	0.72922

pattern			A _{3:1}				
Frequency(Hz)	Reflection loss(dB)	Complex permittivity(ϵ_r)	Complex Permeability(μ_r)	$\frac{\mu_r}{\epsilon_r}$	$Z = \sqrt{\frac{\mu_r}{\epsilon_r}}$	$\tan \delta_\epsilon = \frac{\epsilon''}{\epsilon'}$	$\tan \delta_\mu = \frac{\mu''}{\mu'}$
9.125E9	-36.62827	2.3445+i0.79689	2.4215+i0.69808	1.03285	1.01629	0.3399	0.28828
1.09E10	-20.90296	3.388-i1.39564	2.53689-i0.3353	0.74879	0.86532	-0.41194	-0.13217
1.095E10	-24.52667	0.10052-i0.86502	0.32962-i 0.7886	3.27916	1.81084	-8.60541	-2.39255
1.1025E10	-29.82503	1.03958+i0.90008	1.0305+i0.74513	0.99126	0.99562	0.86581	0.72307

Table (4-6 c): clarify values of complex permittivity and permeability, characteristic impedance, loss tangent for resonance peaks for the samples A_{2:2}, A_{1:3}&A_{0:4}

Pattern			A _{2:2}				
Frequency (Hz)	Reflection loss(dB)	Complex permittivity(ϵ_r)	Complex Permeability(μ_r)	$\frac{\mu_r}{\epsilon_r}$	$Z = \sqrt{\frac{\mu_r}{\epsilon_r}}$	$\tan \delta_\epsilon = \frac{\epsilon''}{\epsilon'}$	$\tan \delta_\mu = \frac{\mu''}{\mu'}$
9.125E9	-29.52941	2.19395+i0.77269	2.45923+i0.7078	1.12091	1.05873	0.35219	0.28783
1.095E10	-26.20758	0.22348-i0.9507	0.33818-i0.7785	1.51327	1.23015	-4.25411	-2.3022
1.1025E10	-26.17928	0.97538+i0.96492	1.00041+i 0.7296	1.02567	1.01275	0.98928	0.72934
pattern			A _{1:3}				
Frequency(Hz)	Reflection loss(dB)	Complex permittivity(ϵ_r)	Complex Permeability(μ_r)	$\frac{\mu_r}{\epsilon_r}$	$Z = \sqrt{\frac{\mu_r}{\epsilon_r}}$	$\tan \delta_\epsilon = \frac{\epsilon''}{\epsilon'}$	$\tan \delta_\mu = \frac{\mu''}{\mu'}$
9.125E9	-36.83315	2.39583+i0.80469	2.40474+i0.6835	1.00372	1.00186	0.33587	0.28425
1.09E10	-21.92098	3.30631-i1.36211	2.59189-i0.3980	0.78392	0.88539	-0.41197	-0.15359
1.095E10	-22.50051	0.04845-i0.89986	0.3461-i 0.80277	7.14357	2.67275	-18.5735	-2.3195
1.1025E10	-30.75777	1.08868+i0.89384	1.00711+i0.7789	0.92508	0.96181	0.82104	0.77348

pattern			$A_{0:4}$				
Frequency (Hz)	Reflection loss(dB)	Complex permittivity(ϵ_r)	Complex Permeability(μ_r)	$\frac{\mu_r}{\epsilon_r}$	$Z = \sqrt{\frac{\mu_r}{\epsilon_r}}$	$\tan \delta_\epsilon = \frac{\epsilon''}{\epsilon'}$	$\tan \delta_\mu = \frac{\mu''}{\mu'}$
9.125E9	-30.78307	0.94085+i0.07284	1	1.06287	1.03096	0.07742	0
1.095E10	-24.13283	1.11432-i0.29113	1	0.8974	0.94731	-0.26126	0
1.1025E10	-25.04896	1.17275+i0.14055	1	0.8527	0.92342	0.11984	0

Chapter Five

Conclusions

and Future

Recommendations

5.1- Conclusions

1- The perfect ratio to get M-type hexagonal phase when the molar ratio of ferric nitrate to barium nitrate equal (12:1). And the sol-gel auto-combustion technic enabled to get homogeneous and ultrafine barium ferrites.

2- When changing a molar ratio to Fe/Ba (12:3), this leads to the formation of secondary phase barium mono-ferrite (BaFe_2O_4), when increased molar ratio to 12:6 Fe/Ba, hexagonal phase disappears completely and formed BaFe_2O_4 (antiferromagnetic) despite the high calcination temperature (1200°C).

3- Intermediate phases were transformed into $\text{BaFe}_{12}\text{O}_{19}$ hexagonal phase when increasing the calcination temperature at 800°C or greater than, with fixing the molar ratio of Fe/Ba in 12:1.

4- From SEM micrographs the average grain size estimated about 500nm for the sample sintered at 800°C and the porosity 60%, the diameter of grain size closer to critical size of single magnetic domain.

5-LCR-meter tests showed within frequency range (50-1MHz) that the samples which sintering at 800°C , 900°C , 1000°C , 1100°C and 1200°C have higher dielectric constant at lower frequency and decreases sharply up to (25175 Hz) and then decreasing gradually with increasing the frequency this behavior is typical of ferrites and a similar behavior was observed by several authors[92], Above (25175 Hz) notice a change in the behavior of dielectric constant (ϵ' and ϵ'') for the samples especially the sample sintered at 800°C the real and imaginary part of dielectric constant decreasing exponentially with increasing frequency, it observed high conductance for the samples was sintered at 800°C and 1200°C .

6- within the frequency range (8-9) GHz it observed that the Reflection loss decreasing because the particles being sufficiently small to approach single domain characteristics so that only spin rotations can occur and decreases with increases sintering temperature which cause to growth of the grain size.

7- Increasing of sintering temperature caused to shifted absorption curves tends to lower frequency.

8- There are resonance peaks for barium hexaferrite samples; the peak is formed when there is matching between the relative permeability and relative permittivity of ferrite.

9- Maximum reflection loss -36.83dB observed for the samples $A_{1:3}$ (ferrite: barium titanate) equal 1:3, due to good matching the relative permeability and relative permittivity.

10- The complex Permeability measured for composite material which have been calculated using (NRW) method, was larger than pure material for barium hexaferrite sintering at 1200°C because of overlapping attenuation aggregate from ferrite and epoxy -resin this is causing the spurious values of the magnetic permeability.

5.2 Future Recommendations

1- Preparation of nanoparticles barium hexaferrite (M, W, Y, Z, X and U-type) and comparison of microwave characteristics, structure, electrical and Magnetic Properties.

2- Fabricate of (EMI) electromagnetic immunity Shielding Application in X-Band Frequency Range.

Chapter Five Conclusions and Future Recommendations

3- Preparation of composite materials and studying its microwave characteristics in other bands.

Appendix

Appendix

Appendix

MATLAB Code for Solving the (NRW) Equation

By employment MATLAB (matrix laboratory) allowing access to computing (permittivity, permeability, tangents loss and reflectivity VS frequency) using Nicholson-Ross-Weir (NRW) method, we need to specify the text files containing s-parameters for the measured material and open measurements, absorber thickness, De-Embedding option, and specify if the material is magnetic. The calculated values are also written in an Excel file. The source code of the main function presented below:

```
Function [ f r e q , e r - r e a l , e r - i m a g , e r - a b s , t a n e r , m r - r e a l , m r - i m a g ,  
Mr- abs , t a n m r , r e f l , c a p , s 1 1 R , s 1 1 I , s 2 1 R , s 2 1 I , s 1 2 R , s 1 2 I , s 2 2 R ,  
s 2 2 I ]  
  
=NRModel ( F i l e P a t h 1 , F i l e P a t h 2 , T h i c k n e s s , C h e c k B o x S t a t u s 1  
C h e c k B o x S t a t u s 2 )  
  
global FILENAME1  
  
global FILENAME2  
  
Data meas=import tdata ( F i l e P a t h 1 ) ; % i m p o r t d a t a f r o m f i l e  
  
Data open=import tdata ( F i l e P a t h 2 ) ;  
  
[m, n]=s i z e ( D a t a m e a s ) ;  
  
c = 2.99792_10^8; % s p e e d o f l i g h t
```

Appendix

```
%****c r e a t e a r r a y s ****
```

```
e r- r e a l =zeros (m, 1 ) ;
```

```
e r- i m a g =zeros (m, 1 ) ;
```

```
e r- a b s =zeros (m, 1 ) ;
```

```
d = Thickness * 10(-3) ;
```

```
t a n e r =zeros (m, 1 ) ;
```

```
m r- r e a l =zeros (m, 1 ) ;
```

```
m r- i m a g =zeros (m, 1 ) ;
```

```
m r- a b s =zeros (m, 1 ) ;
```

```
t a n m r =zeros (m, 1 ) ;
```

```
r e f l =zeros (m, 1 ) ;
```

```
c a p =zeros (m, 1 ) ;
```

```
s 1 1 R =zeros (m, 1 ) ;
```

```
s 2 1 R =zeros (m, 1 ) ;
```

```
s 1 2 R =zeros (m, 1 ) ;
```

```
s 2 2 R =zeros (m, 1 ) ;
```

```
s 1 1 I =zeros (m, 1 ) ;
```

```
s 2 1 I =zeros (m, 1 ) ;
```

```
s 1 2 I =zeros (m, 1 ) ;
```

Appendix

```
s 2 2 I=zeros (m, 1 ) ;

% *****

z0=376.734;

e r0 =8.854_10^-12;

mr0=4×pi ×10^-7;

%read frequency and s-parameters

f r e q=Data- meas ( : , 1 ) ;

s11- mag- meas=Data- meas ( : , 2 ) ;

s11- deg- meas=Data- meas ( : , 3 ) ;

s21- mag- meas=Data- meas ( : , 4 ) ;

s21- deg- meas=Data- meas ( : , 5 ) ;

s12- mag- meas=Data- meas ( : , 6 ) ;

s12- deg- meas=Data- meas ( : , 7 ) ;

s22- mag- meas=Data- meas ( : , 8 ) ;

s22- deg- meas=Data- meas ( : , 9 ) ;

% i f De-Embedding i s enabled than read s-parameters from f i l e

i f ( CheckBoxStatus1 )

s11- mag- open=Data- open ( : , 2 ) ;

s11- deg- open=Data- open ( : , 3 ) ;
```

Appendix

```
s21- mag- open=Data -open ( : , 4 ) ;  
s21- deg- open=Data- open ( : , 5 ) ;  
s12- mag -open=Data- open ( : , 6 ) ;  
s12- deg- open=Data -open ( : , 7 ) ;  
s22- mag -open=Data- open ( : , 8 ) ;  
s22- deg- open=Data- open ( : , 9 ) ;  
  
end;  
  
for k=1:m  
  
lamb0=c /( f r e q ( k ) ) ;  
  
% t h i s i s f o r Real /Imag s-parameter format  
  
s11- meas = s11- mag- meas ( k)+1 i*s11 deg- meas ( k ) ;  
s21- meas = s21- mag -meas ( k)+1 i *s21 deg- meas ( k ) ;  
s12- meas = s12- mag- meas ( k)+1 i* s12 deg- meas ( k ) ;  
s22- meas = s22- mag- meas ( k)+1 i * s22 deg- meas ( k ) ;  
  
% i f De-Embedding i s enabled than do act al De-Embedding  
  
i f ( CheckBoxStatus1 )  
  
s11 -open = s11- mag -open ( k)+1 i *s11- deg-open ( k ) ;  
s21- open = s21- mag -open ( k)+1 i*s21 deg -open ( k ) ;  
s12- open = s12- mag -open ( k)+1 i *s12 deg -open ( k ) ;
```

Appendix

$$s_{22\text{-open}} = s_{22\text{-mag-open}}(k) + 1i * s_{22\text{-deg-open}}(k);$$

$$s\text{-params-meas} = [s_{11\text{-meas}}, s_{12\text{-meas}}; s_{21\text{-meas}}, s_{22\text{-meas}}];$$

$$s\text{-params-open} = [s_{11\text{-open}}, s_{12\text{-open}}; s_{21\text{-open}}, s_{22\text{-open}}];$$

$$y\text{-params-meas} = s_{2y}(s\text{-params-meas}, 201);$$

$$y\text{-params-open} = s_{2y}(s\text{-params-open}, 201);$$

$$y\text{-params} = y\text{-params-meas} - y\text{-params-open};$$

$$s\text{-params} = y_{2s}(y\text{-params}, z_0);$$

$$s_{11} = s\text{-params}(1, 1);$$

$$s_{21} = s\text{-params}(2, 1);$$

$$s_{12} = s\text{-params}(1, 2);$$

$$s_{22} = s\text{-params}(2, 2);$$

$$s_{11R}(k) = \text{real}(s_{11});$$

$$s_{11I}(k) = \text{imag}(s_{11});$$

$$s_{21R}(k) = \text{real}(s_{21});$$

$$s_{21I}(k) = \text{imag}(s_{21});$$

$$s_{12R}(k) = \text{real}(s_{12});$$

$$s_{12I}(k) = \text{imag}(s_{12});$$

Appendix

s22R(k)=real (s22) ;

s 2 2 I (k)=imag(s22) ;

% De-Embedding option is not enabled

else

s11=s11- meas ;

s21=s21- meas ;

s12=s12- meas ;

s22=s22- meas ;

s11R(k)=real (s11) ;

s 1 1 I (k)=imag(s11) ;

s21R(k)=real (s21) ;

s 2 1 I (k)=imag(s21) ;

s12R(k)=real (s12) ;

s 1 2 I (k)=imag(s12) ;

s22R(k)=real (s22) ;

s 2 2 I (k)=imag(s22) ;

s- params = [s11 s12 ; s21 s22] ;

Appendix

```
y- params = s2y ( s- params , z0 ) ;  
  
cap ( k)=y- params ( 1 , 1 ) / ( 2 * pi * f r e q ( k ) ) ;  
  
end;  
  
%Nicolon Ross Model  
  
V1 = s21 + s11 ;  
  
V2 = s21 - s11 ;  
  
X = ( 1 - V1*V2 ) / ( V1 - V2 ) ;  
  
i f abs ( X + sqrt ( X^2 - 1 ) ) <= 1  
  
G = X + sqrt ( X^2 - 1 ) ;  
  
Else  
  
G = X - sqrt ( X^2 - 1 ) ;  
  
end;  
  
T = ( ( s11+s21 ) - G ) / ( 1 - ( s11+s21 ) * G ) ;  
  
i f ( CheckBoxStatus2 )  
  
w = 2*pi * f r e q ( k ) ;  
  
c1 = ( ( 1 + G ) / ( 1 - G ) ) ^ 2 ;  
  
c2 = - ( c / ( w*d ) * log ( 1/T ) ) ^ 2 ;  
  
e r = sqrt ( c2 / c1 ) ;  
  
e r- r e a l ( k ) = real ( e r ) ;
```

Appendix

```
e r- imag ( k)=imag( e r ) ;  
e r- abs ( k)=abs ( e r ) ;  
tan er ( k)=er- imag ( k) / e r- r e a l ( k ) ;  
mr = sqrt ( c1 *c2 ) ;  
mr- r e a l ( k)=real ( mr ) ;  
mr- imag ( k)=imag( mr ) ;  
mr- abs ( k)=abs ( mr ) ;  
tanmr ( k)=mr- imag ( k) / mr- real ( k ) ;  
else  
mr=1;  
mr- r e a l ( k)=real ( mr ) ;  
mr- imag ( k)=imag( mr ) ;  
mr- abs ( k)=abs ( mr ) ;  
tanmr ( k)=mr- imag ( k) / mr- real ( k ) ;  
e r=((1 - G)^2/(1 + G) ^ 2 ) ;  
e r- r e a l ( k)=real ( e r ) ;  
e r- imag ( k)=imag( e r ) ;  
e r- abs ( k)=abs ( e r ) ;  
tane r ( k)=er- imag ( k) / e r- r e a l ( k ) ;
```

Appendix

```
end;

r = sqrt (mr/ e r ) * tanh( 1 i _ ( 2 * pi / c ) * f r e q ( k ) * d * sqrt (mr * e r ) ) ;

r e f l ( k ) = 20 * log10 ( abs ( ( r - 1 ) / ( r + 1 ) ) ) ;

% Create  xlsx  file and write data

i f ( CheckBoxStatus1 ) %  if De-Embedding i s enabled that include the
OPEN f i l e

OutFi le = strcat ( 'Output-' , FILENAME1 , '- DE-' , FILENAME2 , '. x l s x ' ) ;

else          % De-Embedding opt ion i s not enabled

OutFi le = s t r c a t ( 'Output-' , FILENAME1 , '. x l s x ' ) ;

End

Header = { ' Freq  _ ( Hz ) ' , ' e _ Real ' , ' e _ Imaginary ' , ' Abs ( e ) ' , ' Loss _
Tan _ e ' , ' u _ Real ' ,
' u _ Imaginary ' , ' Abs ( u ) ' , ' Loss _ Tan _ u ' , ' Re f l e c t i v i t y ' ,
' Capacitance ' , ' s11R ' , ' s 1 1 I ' , ' s21R ' , ' s 2 1 I ' , ' s12R ' , ' s 1 2 I ' ,
' s22R ' , ' s 2 2 I ' } ;

Xls wr i t e ( OutFi le , Header , 'A1 : S1 ' ) ;

Xls wr i t e ( OutFi le , f r e q , s t r c a t ( 'A2 :A' , num2str(m+1) ) ) ;

Xls wr i t e ( OutFi le , e r - r e a l , s t r c a t ( 'B2 :B' , num2str(m+1) ) ) ;

Xls wr i t e ( OutFi le , e r - i m a g , s t r c a t ( 'C2 :C' , num2str(m+1) ) ) ;

Xls wr i t e ( OutFi le , e r - a b s , s t r c a t ( 'D2 :D' , num2str(m+1) ) ) ;
```

Appendix

Xls wr i t e (OutFi le , taner , s t r c a t ('E2 :E ' , num2str(m+1))) ;

Xls wr i t e (OutFi le , mr- real , s t r c a t ('F2 :F ' , num2str(m+1))) ;

Xls wr i t e (OutFi le , mr- imag , s t r c a t ('G2 :G ' , num2str(m+1))) ;

Xls wr i t e (OutFi le , mr- abs , s t r c a t ('H2 :H ' , num2str(m+1))) ;

Xls wr i t e (OutFi le , tanmr , s t r c a t (' I2 : I ' , num2str(m+1))) ;

Xls wr i t e (OutFi le , r e f l , s t r c a t (' J2 : J ' , num2str(m+1))) ;

Xls wr i t e (OutFi le , cap , s t r c a t ('K2 :K' , num2str(m+1))) ;

Xls wr i t e (OutFi le , s11R , s t r c a t ('L2 :L ' , num2str(m+1))) ;

Xls wr i t e (OutFi le , s11I , s t r c a t ('M2:M' , num2str(m+1))) ;

Xls wr i t e (OutFi le , s21R , s t r c a t ('N2 :N' , num2str(m+1))) ;

Xls wr i t e (OutFi le , s21I , s t r c a t ('O2 :O' , num2str(m+1))) ;

Xls wr i t e (OutFi le , s12R , s t r c a t ('P2 :P ' , num2str(m+1))) ;

Xls wr i t e (OutFi le , s12I , s t r c a t ('Q2 :Q' , num2str(m+1))) ;

Xls wr i t e (OutFi le , s22R , s t r c a t ('R2 :R' , num2str(m+1))) ;

Xls wr i t e (OutFi le , s22I , s t r c a t (' S2 : S ' , num2str(m+1))) ;

References

References

- [1] J. M. D. COEY "Magnetism and Magnetic Materials" 1st ed ,New York (2010).
- [2] J.L. Snoek, " **New Developments in Ferromagnetic Materials** ", Elsevier Publishing Co., Inc., New York-Amsterdam (1947).
- [3] B.Lax, and K.J.Button, , " **Microwave Ferrites and Ferrimagnetics** ", McGraw Hill Book Co., (1962).
- [4] A.J. Fuller, " **Ferrites at Microwave Frequencies** ", Peter Peregrinuss Ltd., London, (1987).
- [5] S. B, Narang, and I. S. Hudiara. " **Microwave dielectric properties of M-type barium, calcium and strontium hexaferrite substituted with Co and Ti.**" *Journal of Ceramic Processing Research* 7.no,2: p.p.113. (2006)
- [6] V.R.K.Murthy, S.Sundaram, and B.Vishwanathan, , " **Microwave Materials** ", Narosa Publishing House, New Delhi (1993).
- [7] W.D.Kingly, D.R.uhlmann and H.K.Bowenm " **Introduction to ceramic** " 2nd edition.New York (1976).
- [8] H.Ota, M. Kimura, R. Sato, K. Okayama, S.Kondo and M.Homma " **Broadband Microwave absorber using M-type hexagonal Ferrite. In Electromagnetic Compatibility** " IEEE International Symposium on ,Vol. 2, p.p. 590-593. (1999).
- [9] I.Nedkov, and A. Petkov. " **IEEE Transaction Magnetism.**" *MAG-26* p.p. 1483-1484, (1990).
- [10] Y. K Marina, E. K Alexey, and A. K Alexander " **Advances in Engineering and Applications of Hexagonal Ferrites in Russia** " Chapter 4 in *Advances in Ceramics – electric and magnetic Ceramics, bioceramics, Ceramics and environment* ,Croatia ,.p.p. 60-64, (2011)

- [11] H. J. Kwon, J. Y. Shin, and J. H. Oh "The microwave absorbing and resonance phenomena of Y-type hexagonal ferrite microwave absorbers " J.Appl.phys, vol.75, No.10, p.p. 6109-6111,(1994)
- [12] C. D Mukesh, C. K Subhash, D.C. Dube "Electrical and magnetic properties of barium hexaferrite nanoparticles prepared by citrate precursor method " Ceramics International 30 ,p.p.1623–1626, (2004)
- [13] A. Ghasemi, A. Hossienpour, A. Morisako, A. Saatchi, M. Salehi " Electromagnetic properties and microwave absorbing characteristics of doped barium hexaferrite " Journal of Magnetism and Magnetic Materials 302 ,p.p.429–435, (2006)
- [14] S.M. Abbasa, A.K. Dixit, R. Chatterjee, T.C. Goel " Complex permittivity, complex permeability and microwave absorption properties of ferrite–polymer composites " Journal of Magnetism and Magnetic Materials , vol.309,p.p. 20–24 , (2007)
- [15] M.Guohong, C. Na, P.Xifeng, S.Haigen, G. Mingyuan " Preparation and microwave absorption properties of barium ferrite nanorods " Materials Letters, vol.62, p.p.840–842, (2008).
- [16] L.C. Jefferson, R.C. Valeska, O.Tsuneharu and S.P.Magali "Performance of Radar Absorbing Nanocomposites by Waveguide Measurements " Materials Research, Vol. 11, No. 3,p.p. 319-324,(2008).
- [17] W.Lixi, S. Jie, Z.Qitu, H.Xiaogu and X.Naicen "The microwave magnetic performance of Sm^{3+} doped $\text{BaCo}_2\text{Fe}_{16}\text{O}_{27}$ " Journal of Alloys and Compounds 481 ,p.p. 863–866. (2009)
- [18] R.S. Meena, B.Sudeshna,C. Ratnamala "Complex permittivity, permeability and wide band microwave absorbing property of La^{3+} substituted U-type hexaferrite " Journal of Magnetism and Magnetic Materials 322,P.P. 1923–1928. (2010)
- [19] G.Ali, E. S .Sagar, L.Xiaoxi, and M.Akimitsu" Enhanced reflection loss characteristics of substituted barium ferrite/functionalized multi-

walled carbon nanotube nanocomposites" JOURNAL OF APPLIED PHYSICS 109, 07,p.p,A507, (2011).

[20] C.Sun Chang, K.Sun, P.Chui "**Microwave absorption properties of Ce-substituted M-type barium ferrite**" Journal of Magnetism and Magnetic Materials 324 ,p.p.802–805, (2012)

[21] K.D.Chapal "**Microwave Absorbing Properties of DBSA-doped Polyaniline/BaTiO₃-Ni_{0.5}Zn_{0.5}Fe₂O₄ Nanocomposites**" Journal of Materials Science Research, Vol. 1, No. 1,(2012)

[22] K.Abhishek, A.Vijaya, and S.Dharmendra "**effect of particle size of BaFe₁₂O₁₉ on the microwave absorption characteristics in X- band**" Progress in Electromagnetics Research M, Vol. 29,(2013)

[23] A.Hamed, P.Mohammad "**A Study on the Effect of Temperature in Synthesis and Magnetic Properties of W-Type Hexaferrites Barium Nano Composites with Radar Wave Absorbing Properties**" Natural and Social Sciences, Vol.3, No.3 pp. 580-588,(2014)

[24] S. Vinayasree, M. A. Soloman, S.Vijutha, P. Mohanan, K.Philip, P. A. Joy, and M. R. Anantharaman "**Flexible microwave absorbers based on barium hexaferrite, carbon black, and nitrile rubber for 2–12GHz applications**" J. Appl. Phys. 116, P.P.024902 (2014).

[25] E. J.Silvia, G. B.Paula, A. H.Carlos and A. V.Leandro "**Sr hexaferrite/Ni ferrite nanocomposites: magnetic behavior and microwave absorbing properties in the X-band**" Materials Chemistry and Physics, Volume 157, Pages 124–129,(2015)

[26] V. F. Veley, "**Modern Microwave Technology** ", Ch. (1), Ellis Horwood Limited, New York, (1987)

[27] S. Y. Liao, "**Microwave Devices and Circuits** " Printice Hall Inc., New Jersey, (1990)

[28] B.Ananjan, "**An introduction to microwave measurements** " Ch.(4), Boca Raton London New York,(2015)

- [29] L. F. Chen, C. K. Ong, C. P. Neo, V. V. Varadan and V. K. Varadan " **Microwave Electronics Measurement and Materials Characterization** " England,(2004)
- [30] Nicolson, A. M., and G. F. Ross. "**Measurement of the intrinsic properties of materials by time-domain techniques**", *IEEE Transactions on instrumentation and measurement* 19.4,p.p. 377-382. (1970)
- [31] Weir, William B. "**Automatic measurement of complex dielectric constant and permeability at microwave frequencies.**" *Proceedings of the IEEE* 62, no. 1, p.p. 33-36, (1974)
- [32] Tucker and Rampton Norrtla – Holl. Pub. Comp. Amsterdam, (1972).
- [33] Vinoy and Jha, "**Radar Absorbing Materials**" National Aerospace Laboratories, India, (1996).
- [34] Ahmed and Al-Rashed "**Electric and Magnetic**" 1st Edition University of AL-Basra , (1978).
- [35] Al-Sharbaty , Al-Kheyat and S. K. Hassoun "**Physical Optics**" University of Baghdad , (1983).
- [36] Smith and Hosie " **Basic Electrical Engineering Science**" Pub. Lengman Group Lim., London, (1973).
- [37] Zaki , Ibrahim and Mohammed "**Electrical machinery**" university of Al-Mosul (1975).
- [38] Michielssen , Saier , Ranjithan, and R.Mittras , " **IEEE TRANSACTIONS ON MICROWAVE THEORY AND TECHNIQUES** ", Vol. 41, No.617. 1024. (1993)
- [39] Braders and Scheer, " **IEEE TRANSACTIONS ON MICROWAVE THEORY AND TECHNIQUES** ", Vol. 24 (1988)
- [40] D.Stoppels, "**Frequency dependence of the complex permeability of monocrystalline MnZn ferrous ferrites.**" *Journal of Applied Physics* 52.3 ,pp.2433-2435, (1981)

- [41] Ganchev, Bhattacharyya, Bakhtiari, and Qaddoumi, "IEEE TRANSACTIONS ON MICROWAVE THEORY AND TECHNIQUES " Vol.42, pp.18, (1994)
- [42] Taher, Lamer, and Chanterac , "IEEE TRANSACTIONS ON MICROWAVE THEORY AND TECHNIQUES ", Vol.38 .1, (1990)
- [43] A. I. Al- Khfagy "Studying some Properties of Spinel Ferrite preparing by Ceramic and Sol-Gel Methods " ph.D.thesis, University of Al-Mustansiriyah,(2015)
- [44] Johnson, "Radar-Absorbing Materials : A passive Role in Active Scenario, "Rep.Int.Count. Handbook, 11th ed,(2000).
- [45] Harmuth " IEEE Trans. On Elect .Comp " Vol. EMC.27 ,100, (1985)
- [46] V. Akhterov "microwave absorption in nanosructures " UNIVERSITY of CALIFORNIA SANTA CRUZ,(2010)
- [47] Application Note 1217-1, "Basics of Measuring the Dielectric Properties of Materials" , Agilent Technologies, Inc.,(2006)
- [48] A.J. Moulson and J. M. Herbert, "Electroceramics: Materials, Properties, Applications " , 2nd ed, Wiley, West Sussex, (2003).
- [49] M. Hill, " The Microwave Palaeointensity Technique and its Application to Lava" , PhD. Thesis, University of Liverpool, (2000).
- [50] E.F. Knott, J.F. Shaeffer, M.T. Tuley, "Radar Cross Section " 2nd ed ,Artech House, Boston,(1993).
- [51] B .Stephen, "Magnetism in Condensed Matter " , Oxford University Press ,Oxford, (2001).
- [52] C,Soshin, "Physics of Magnetism " , John Wiley and Sons, New York , (1964),
- [53] A. Muhammad ,Ph. D. Thesis, physics Department, Quaid-i-Azam University, Islamabad, Pakistan. (2008).

- [54] Jackson, "**Classical Electrodynamics**", 3rd Ed. John Wiley & Sons, Inc, New York, (1998).
- [55] Halliday, R. Resnick, Walker, "**Fundamentals of Physics**", 6th Ed. John Wiley & Sons, New York, (2002).
- [56] Vijaya, Rangarajan, "**Materials Science**", McGraw-Hill Publishing Company Limited, New Delhi, 447, (1999-2000)
- [57] Kittel, "**Introduction to Solid State Physics**", 7th Ed. John Wiley & Sons, New York, (1996).
- [58] Omar, "**Elementary Solid State Physics (Principles & Applications)**" Addison-Wesley Publishing Company, Amsterdam, (1962).
- [59] Morish, "**The Physical Principles of Magnetism**", John Wiley and Sons, (1965).
- [60]- Reitz, Milford, Chrisly, "**Foundations of Electromagnetic Theory**", 3rd Ed. Addison-Wesley Publishing Company, London (1979).
- [61]- E.Veena Gopalan, , and M. R. Anantharaman. "**On the Synthesis and Multifunctional Properties of some Nanocrystalline Spinel Ferrites and Magnetic Nanocomposites.**" PhD diss., Cochin University of Science and Technology, (2009).
- [62] H. Kojima, "**Ferromagnetic Materials**", Ed. E.P. Wohlfarth, North-Holland Publishing Company, 3, 309 (1982).
- [63] Nilofer Parween "**Study of barium hexaferrite (BaFe₁₂O₁₉) synthesized by sol gel auto- combustion technique**" dept of physcs and astronomy, National Institute of Technology, Rourkela, MSc thesis,(2014)
- [64] M. P.Edward ~ "**Epoxy Adhesive Formulations**", The McGraw-Hill Companies, (2006).
- [65] K.S. Ghead , "**Synthesis and characterization of magnesium ferrites material**", M.Sc. Thesis, Department of Applied Sciences, University Of Technology,(2012).

- [66] V.Raul "**Magnetic ceramics**", HICambridge University Press (Eds.), , (1994).
- [67] Lu, A. H., Salabas, E. E., & Schüth, F. "**Magnetic nanoparticles: synthesis, protection, functionalization, and application**" *Angewandte Chemie International Edition*, 46, no. 8, p.p.1222-1244. (2007).
- [68] Brinker, C. Jeffrey, and W. Scherer. "**Sol-gel science: the physics and chemistry of sol-gel processing**", Academic press, (2013)
- [69] L.l.Hench and K. W.Jon est, "**The sol-gel process.**" *Chemical Reviews* 90, no. 1 pp. 33-72, (1990).
- [70] V. Petkov, T. Ohta, Y. Hou, Y. Ren, "**Atomic-Scale Structure of nanocrystals by High-Energy X-ray Diffraction and Atomic Pair Distribution Function Analysis Nanoparticles**" *J. Phys. Chem. C* 11 p.p.714-720,(2007)
- [71] H. Keller, "**X-ray Diffraction**" University stuttgart fakultat for mathematic and physic, advanced practical course, (2011).
- [72] D.Garmo's, "**Materials and Processes in Manufacturing**" Wiley,10th Edition,(2007).
- [73] J.Connolly, "**Elementary Crystallography for X-Ray Diffraction**", Introduction to X-Ray powder diffraction, Spring, (2012).
- [74] A. Goldman, "**Modern ferrite technology**" Van nostrand reinhold, New York,(1990).
- [75] Nisreen Zaidan Khalaf "**Preparation of nano barium ferrite and study of its physical properties**" M.Sc. Thesis, University of Diyala,(2011).
- [76] William D. Callister, Jr. "**Materials Science and Engineering**"7th Edition,(2007).
- [77] A.J. Moulson and J.M.Herbert, "**Electroceramics-Materials-properties-applications Chapman and Hall**", London, p.p.18, 52,277, (1990).

- [78] M.A.Iqbal, Amna Mir and Shezad “**synthesis and Characterizations of nano-sized barium Hexa ferrite using sol-gel method**” NSTI-Nanotech, p.p.103-106, vol.1, (2010).
- [79] G.K.Sahoo, "**Synthesis and Characterization of BaTiO₃ Prepared by Molten Salt Synthesis Method.**" PhD diss, (2009).
- [80] M. M. Vijatović, J. D. Bobić, and B. D. Stojanović. "**History and challenges of barium titanate: Part II.**" *Science of Sintering* 40, no. 3 ,p.p.235-244, (2008).
- [81] Asuka Namai and Shin-ichi Ohkoshi, "**High-frequency Millimeter Wave Absorber Composed of a New Series of Iron Oxide Nanomagnets**" ,InTech, vol. 10, pp.494-501,(2011).
- [82] Rohde & Schwarz "**Measurement of Material Dielectric Properties**" <http://www.0CustomerSupport@rohde-schwarz.com> ,<RAC0607-0019_1_4E>. pdf
- [83] C.Varsha ,S. Chavan,M. Shirsath, L. Mane and Surendra S. More "**Effect of Dy³⁺ substitution on the structural properties of barium hexaferrite nanoparticles**" Journal of Chemical and Pharmaceutical Research, 7(4),PP.675-678,(2015).
- [84] C.Sajal, H. Akther "**Synthesis and Magnetic Properties of Ba₂Ni_{2-x}Zn_xFe₁₂O₂₂ Hexaferrites**" Journal of Condensed Matter Physics, 2, p.p.181-187,(2012)
- [85] S. Laith "**preparation of Co_{1-x}Zn_xFe₂O₄ Nano ferrite and study of its electrical and structural properties**" M.Sc. Thesis,University of Diyala,(2012).
- [86] Y.Y. Meng, M.H. He, Q. Zeng, D.L. Jiao, S. Shukla, R.V. Ramanujan, Z.W. Liu "**Synthesis of barium ferrite ultrafine powders by a sol–gel combustion method using glycine gels**" Journal of Alloys and Compounds vol,583,p.p.220–225, (2014).
- [87] E.Lesley , Smart, A. Moore, "**Solid State Chemistry**" , 4th Edition , Boca Raton .Landon .New York,(2012)

- [88] C.Mukesh ,Dimri, D. C. Dube "Permittivity and Permeability of Polycrystalline $\text{Ba}(\text{CoZr})_x\text{Fe}_{12-2x}\text{O}_{19}$ and Their Composite Thick Films at RF and Microwave Frequencies" *Journal of Materials Science and Engineering*, vol.3,p.p.208-218,(2015)
- [89] Rezlescu, N., and E. Rezlescu. "Dielectric properties of copper containing ferrites." *physica status solidi (a)* 23, no. 2 ,p.p.575-582, (1974).
- [90] M. T.Farid, I. Ahmad, S. Aman, M.Kanwal, G.Murtaza, I. ALIa, and M.Ishfaq, "STRUCTURAL, ELECTRICAL AND DIELECTRIC BEHAVIOR OF $\text{Ni}_x\text{Co}_{1-x}\text{Nd}_y\text{Fe}_{2-y}\text{O}_4$ NANO-FERRITES SYNTHESIZED BY SOL-GEL METHOD " *Digest Journal of Nanomaterials and Biostructures*, 10,no(1), p.p.265-275, (2015).
- [91] J.C. Maxwell "Electricity and Magnetism " 1, Oxford University Press, Oxford, (section 328) (1929).
- [92] K.W.Wagner,. "The physical nature of the electrical breakdown of solid dielectrics." *Journal of the American Institute of Electrical Engineers* 41,no.12p.p. 1034-1044, (1922)
- [93] J. Qiu, Gu ,Mingyuan, and S.Haigen, "Microwave absorption properties of Al-and Cr-substituted M-type barium hexaferrite." *Journal of magnetism and magnetic materials* 295, no. 3 ,p.p. 263-268, (2005).
- [94] S.Sugimoto, K.Haga, T. Kagotani, and K.Inomata, "Microwave absorption properties of Ba M-type ferrite prepared by a modified coprecipitation method." *Journal of magnetism and magnetic materials*, 290, p.p.1188-1191, (2005)
- [95] Cullity, D.Bernard, and D. G.Chad."Introduction to magnetic materials." John Wiley & Sons, (2011).
- [96] V.Vivek, K.Jyoti, S.Neelam "Structural, Magnetic Properties of Soft and Hard Ferrites and their EMI Shielding Application in X-Band Frequency Range" *International Journal of Engineering Research & Technology (IJERT)*, Vol.3,p.p.557-560.(2014)

- [97] P. ANNADURAI, A. K. MALLICK, D. K. TRIPATHY "Studies on Microwave Shielding Materials Based on Ferrite and Carbon Black-Filled EPDM Rubber in the X-Band Frequency" Journal of Applied Polymer Science, Vol. 83, p.p.145–150 ,(2002).
- [98] S. Chikazumi, "SH Charap Physics of Magnetism." ,161, (1964).
- [99] Haijun, Zhang, Liu Zhichao, Yao Xi, Zhang Liangying, and Wu Mingzhong. "Complex permittivity and permeability dependence of Ba₄Zn₂-ZCoZFe₃₆O₆₀ U-type hexaferrites prepared by citrate sol-gel on composition, annealing temperature and frequency." Materials Science and Engineering: B97, no. 2 ,p.p.160-166, (2003).
- [100] H. Severin, , and J. P. Stoll. "Permeabilitat einiger Ferrite mit magnetischen Verlusten im Bereich der Zentimeter-und Millimeterwellen." ZEITSCHRIFT FUR ANGEWANDTE PHYSIK. Vol. 23. No. 3,(1967).



جمهورية العراق
وزارة التعليم العالي والبحث العلمي



جامعة ديالى
كلية العلوم
قسم الفيزياء

تحضير فرايت الباريوم النانوي وقياس خصائصه الكهربائية ضمن النطاق
السيني باستخدام الدليل الموجي

رسالة

مقدمة الى مجلس كلية العلوم /جامعة ديالى وهي جزء من متطلبات نيل درجة الماجستير في علوم
الفيزياء

من قبل

حسين سليمان محمود علي

بكالوريوس في الفيزياء 2007

باشراف

د.صائب ذياب علوان

ا.م.د. تحسين حسين مبارك

2016 ميلادية

1438 هجرية

الخلاصة

تم تحضير فيرايت الباريوم السداسي (نوع-M) باستخدام طريقة المحلول الغروي- الاحتراق الذاتي لتحضير فيرايت متجانس ومتناهي في الصغر وموزع بأحجام صغيرة وملبدة عند درجات حرارة واطئة نسبيا . استخدمت املاح النترات ،حامض الستريك ،الامونيا للحصول على مسحوق فيرايت نانوي عند درجة حرارة 100 م⁰ . اوضحت فحوصات حيود الاشعة السينية ان النسبة الامثل للحصول على الطور السداسي (نوع M-) عندما تكون النسبة المولارية لنترات الحديد الى نترات الباريوم تساوي (12/1) . بعد الحصول على الفيرات النانوي تم تلييدها عند درجات حرارية مختلفة (700،800،900،1000،1100،1200) م⁰ لمدة ثلاث ساعات . اظهرت فحوصات حيود الاشعة السينية وجود اطوار وسطية (BaFe₂O₄) و (γ-Fe₂O₃) بالإضافة الى وجود الطور السداسي (BaFe₁₂O₁₉) عند 700 م⁰ وتختفي الاطوار الوسطية عند ازدياد درجة الحرارة الى 800 م⁰ . ثم حضرت عينات مناسبة لأجراء الفحوصات الكهربائية والمايكروية. اظهرت فحوصات المجهر الالكتروني الماسح (SEM) لعينات فيرايت الباريوم السداسي ان الحجم الحبيبي يبلغ حوالي 0.5، 0.6، 0.8، 1، 1.3 مايكرومتر عند 800، 900، 1000، 1100، 1200 م⁰ على التوالي ، اذ ان زيادة درجة حرارة التلييد تؤدي الى نمو الحجم الحبيبي .

تم دراسة الخصائص الكهربائية لعينات فيرايت الباريوم السداسي بواسطة (LCR) عند درجة حرارة الغرفة ضمن مدى التردد 50 Hz الى 1MHz اذ لوحظ ان قيم ثابت العزل تكون عالية عند الترددات الواطئة ثم تتناقص بحدّة بزيادة التردد وعند بلوغها التردد 25175Hz تبدا بالتناقص التدريجي ويعتبر هذا من السلوك العامة للفيرايات.

كذلك تم دراسة خصائص الامتصاص المايكروية لعينات فيرايت الباريوم السداسي ضمن النطاق السيني(x-Band) من حزمة الاشعة المايكروية 8-12.5 GHz ، استخدمت طريقة (نيكلسون – روز –وير) لحساب النفاذية المغناطيسية والسماحية الكهربائية بعد اجراء الحسابات على مؤثرات s – باراميتر ، لوحظ ازدياد في مقدار التوهين للعينات التي تم تلييدها عند 900، 1000، 1100، 1200 م⁰ بزيادة درجة حرارة التلييد ماعدا العينة التي تم تلييدها عند 800 م⁰ اذ تتصرف بصورة مختلفة عن العينات.

تم تحضير مادة متراكبة متكونة من راتنج الايبوكسي كمادة اساس ومطعمة ب(تيتانات الباريوم و/او فيرايت الباريوم السداسي) بإضافة 1 غرام من المسحوق لكل 10 غرام من راتنج الايبوكسي وبنسب تطعيم مختلفة ، اذ لوحظ خسارة انعكاس عظمى مقداره -36.83 ديسيبييل للعينة A_{1:3} اذ تحتوي على(فيراييت 1:باريوم تيتانات 3) .

